INERTIAL CONFINEMENT FUSION

Lawrence Livermore National Laboratory

ICF Quarterly Report *January–March 1999, Volume 9, Number 2*

Special Issue: Optics Technology for the National Ignition Facility

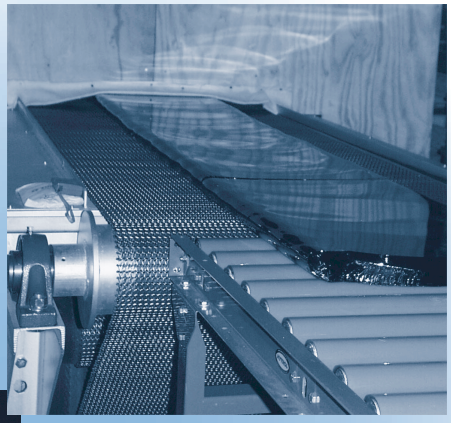

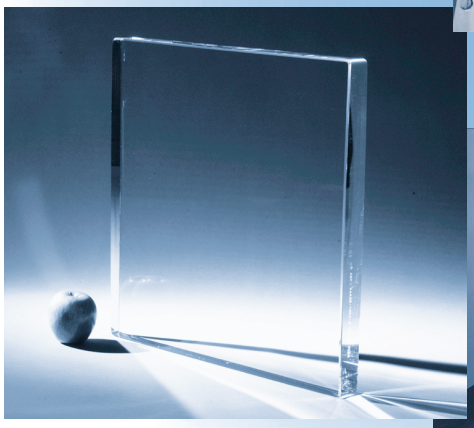

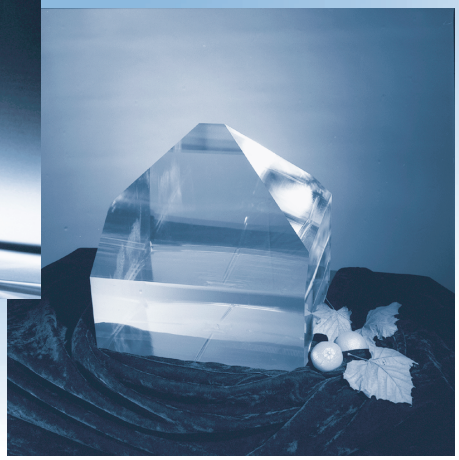

UCRL-LR-105821-99-2

The Cover: Significant progress has been made in optics manufacturing technology development for the NIF. Full-size optics have been produced using advanced manufacturing technologies by the NIF optics companies. Shown clockwise from upper left: A NIF-size amplifier slab fabricated by Zygo from laser glass produced in the Schott Glass Technologies continuous laser glass melter. Continuous strip of laser glass being formed in Hoya Optics laser glass melter. NIF KDP crystal boule produced using rapid growth technology at LLNL, and duplicated by Inrad and Cleveland Crystals. NIF cavity spatial filter lens fabricated by SVG-Tinsley from a Corning fused silica blank.

The *ICF Quarterly Report* is published four times each fiscal year by the Inertial Confinement Fusion Program at the Lawrence Livermore National Laboratory. The journal reports selected current research within the ICF Program. Major areas of investigation presented here include fusion target theory and design, target fabrication, target experiments, and laser and optical science and technology. In addition, the Laser Science and Technology program element of LLNL's Laser Programs serves as a source of expertise in developing laser and electro-optics capabilities in support of the ICF mission and goals and also develops new lasers for government and commercial applications. To keep our readers informed of these new capabilities, the *ICF Quarterly Report* now covers additional non-ICF funded, but related, laser research and development and associated applications. We also include summaries of the quarterly activities within Nova laser operations and the NIF Project. Questions and comments relating to the technical content of the journal should be addressed to ICF/NIF and HEDES Program, Lawrence Livermore National Laboratory, P.O. Box 808, L-475, Livermore, CA 94551.

On the Web:
http://lasers.llnl.gov/lasers/pubs/icfq.html

UCRL-LR-105821-99-2
January–March 1999

Printed in the United States of America
Available from
National Technical Information Service
U.S. Department of Commerce
5285 Port Royal Road
Springfield, Virginia 22161
Price codes: printed copy A03, microfiche A01.

Work performed under the auspices of the U.S. Department of Energy by Lawrence Livermore National Laboratory under Contract W–7405–Eng–48.

INERTIAL CONFINEMENT FUSION

ICF Quarterly Report *January–March 1999, Volume 9, Number 2*

In this issue:

FOREWORD

The National Ignition Facility (NIF) requires approximately 7,500 large optical components, including laser glass amplifier slabs, fused silica lenses, windows and diffractive optics, multilayer mirror and polarizer coatings, and crystals for optical switching and frequency conversion. The Beamlet laser, a scientific prototype of NIF, demonstrated that NIF-size optics could be manufactured to meet the NIF performance requirements. The technologies used to make these optics, while appropriate for Nova and Beamlet, are not suitable for NIF because of the large number of optics needed, the short time frame for producing these optics, and the aggressive cost targets for NIF. To meet these challenges, LLNL and U.S. optics companies have been engaged in a development, facilitization, and pilot production effort started in 1995 to implement the technologies, equipment, and manufacturing facilities needed for the NIF. Most of the companies producing optics for NIF are currently in the middle of or preparing for the pilot production campaigns to demonstrate these technologies.

About 40% of the NIF optics are amplifier slabs fabricated from phosphate laser glass. For all previous ICF laser systems at LLNL and elsewhere in the world, this laser glass has been produced using a batch melting process. Utilizing batch melting technology for the NIF would not meet the cost targets, approximately three times lower than for Beamlet, and would have substantial schedule and performance risks. Schott Glass Technologies of Duryea, Penn., and Hoya Optics of Fremont, Calif., jointly funded by LLNL and the French Commissariat à l'Energie Atomique (CEA), have developed continuous melting technology and built the melting systems needed to produce the laser glass for NIF and the CEA's Laser Megajoule (LMJ). Zygo of Middlefield, Conn., and Eastman Kodak of Rochester, N.Y., have demonstrated several technical advances for fabricating amplifier slabs rapidly, efficiently, and deterministically.

SVG-Tinsley has substantially improved its technologies for rapid fabrication of fused silica blanks into lenses and windows. LLNL, SVG-Tinsley, and Eastman Kodak have all made significant progress in understanding the factors that affect laser damage of fused silica optics at 351-nm wavelength, and altering the fabrication process to improve the damage resistance of these optics. Utilizing diffractive optics technologies developed for the LLNL Petawatt laser and for Nova, prototype NIF diffractive optics structures have been fabricated and demonstrated to meet virtually all of the NIF requirements.

Technologies used to create the multilayer mirror and polarizer coatings have been improved substantially by Spectra-Physics of Mountain View, Calif., and the Laboratory for Laser Energetics at the University of Rochester, N.Y. Improvements include much greater determinism in coating thickness to improve coating yields (not covered in this issue), and significantly greater laser damage resistance. Sol-gel antireflection (AR) coatings applied to fused silica and crystal optics have also been modified to improve their resistance to organic contamination. Work has started to better understand and reduce the sensitivity of crystal AR coatings to humidity.

Beam dumps in the NIF target chamber must survive significant x-ray, laser, ion, and shrapnel exposures without generating excessive vapors or particulates, which in turn would contaminate optics in the final optics assembly. A simple, inexpensive concept utilizing louvered stainless-steel panels has been demonstrated and adopted for NIF.

L. Jeffrey Atherton
Scientific Editor

Properties of and Manufacturing Methods for NIF Laser Glasses

J. H. Campbell *P. Ehrmann*

T. Suratwala *W. Steele*

C. Thorsness *M. McLean*

The laser systems for the U.S. Department of Energy (DOE) National Ignition Facility (NIF) at Lawrence Livermore National Laboratory (LLNL) and for the French Commissariat à l'Energie Atomique (CEA) Laser Megajoule (LMJ) consist of 192 and 240 laser beamlines, respectively.[1–4] Each beamline contains either 16 (NIF) or 18 (LMJ) large, Nd-doped laser glass slabs, and each finished laser glass slab is about $81 \times 46 \times 4.1$ cm^3. A total of 3072 and 4380 slabs will be installed on the NIF and LMJ, respectively (Table 1). In addition, each facility plans to purchase approximately 10% more slabs to be used as construction and operation spares. Thus, nearly 8150 laser glass slabs will be needed for the two laser systems, representing a volume of about 125 m^3 (330 metric tons) of finished, high-optical-quality glass. The quantity of raw glass that must be melted is greater than 330 metric tons to account for various processing losses.

Both the NIF and LMJ use a compact laser amplifier design called the multisegment amplifier (MSA).[5–7] Amplifiers consist of stacked 4×1 arrays of laser glass slabs inside a flashlamp-pumped cavity (Figure 1). By using square apertures (i.e., square beams), it is possible to tightly pack the individual laser glass amplifiers into a compact matrix and greatly reduce the size and cost of the system. This design requires that the laser glass be manufactured in rectangular slabs. Although the laser aperture is square, the laser slabs are rectangular because they are mounted at Brewster's angle to the propagation direction of the beam. Mounting the glass at Brewster's angle minimizes the Fresnel reflection losses at the surfaces of the slabs. In addition, mounting at an angle increases the coupling efficiency of the

TABLE 1. Quantity of laser glass required for the LMJ and NIF projects.

Variable	NIF	LMJ
Number of beamlines	192	240
Number of slabs/beamline	16	18
Spares	10%	10%
Total number of slabs (including spares)	3380	4752
Finished slab dimensions (cm^3)	$81 \times 46 \times 4.1$	$81 \times 46 \times 4.1$
Volume per slab (L)	15.3	15.3
Total volume (m^3)	52	73
Mass (metric tons)	136	190

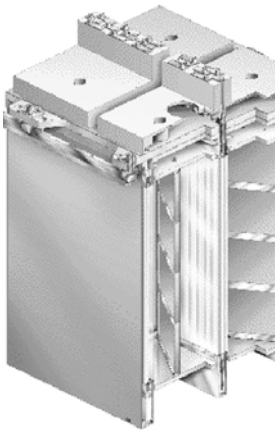

FIGURE 1. Assembly drawing of two 4×2 amplifier units to be used on the NIF. The 81- × 46- × 4.1-cm^3 laser slabs are held in a frame that is mounted at Brewster's angle within the amplifiers. (70-00-0199-0056pb02)

flashlamp light with the slabs. Erlandson et al.[5–7] have recently described in detail the design and operating characteristics of flashlamp-pumped MSAs. The measured small-signal gain coefficient is typically about 0.05/cm, and the stored energy density is about 0.25 J/cm^3 for phosphate laser glass doped at about 4×10^{20}/cm^3 and pumped at a lamp explosion fraction of 0.20.

A prototype laser closely resembling one of the NIF beamlines has recently been built and tested.[8] This laser, called Beamlet, uses 11 amplifiers in the main cavity and 5 in the booster section, the same configuration as that for the NIF. A series of large phosphate glass slabs ($767 \times 428 \times 44$ mm^3) having a doping of 3.5×10^{20}/cm^3 were produced for this laser.[9] Although slightly smaller than required for LMJ and NIF, these prototype glass slabs were made to nearly identical specifications as those required for the NIF and LMJ. Therefore, to a great extent, the quality and size of the laser glass pieces needed for the NIF and LMJ have been demonstrated. What remains is to develop the manufacturing capability for producing a large number of these high-quality glass slabs at a high rate and at significantly lower cost. This article briefly describes the advanced melting methods that are being developed to produce the glass for the NIF and LMJ. Although details of the production processes are proprietary, we highlight the work involved in changing from the one-at-a-time, discontinuous production process used in the past to the continuous melting process of the future. Our cost goal is to manufacture the laser glass for about $1000/L ($350/kg), or roughly a factor of 3 lower than the cost associated with the current, one-at-a-time production methods. Given the size of the laser glass order, this level of cost reduction represents a total cost savings of about $200 million to $300 million compared to the price that could be achieved with current manufacturing methods.

NIF Laser Glass Properties and Specifications

To meet the performance requirements for NIF target applications, the laser glass must have the following important characteristics:

- High net gain.
- Efficient energy storage at high energy density.
- Efficient extraction of stored energy.
- Resistance to laser-induced damage.
- High optical homogeneity to allow light to propagate with negligible wavefront aberration.

Of these five properties, the first three relate to spectroscopic and optical properties of the glass, and the last two to glass quality.

Spectroscopic and Optical Properties

It can be argued that the most important laser glass spectroscopic and optical properties are the emission cross section, fluorescence lifetime, and nonlinear index of refraction. The emission cross section and fluorescence lifetime largely control the gain, energy storage, and extraction efficiency of the laser glass. The nonlinear index strongly impacts beam quality, particularly noise growth at the high operating intensities required for the NIF.

Compared to repetition-rated lasers that fire at frequencies of several hertz, the NIF will be essentially a single-shot device with a few hours between shots. Therefore, the physical properties of glass tend to be of less importance for the end-use application. Nevertheless, the physical properties of glass can be very important to the successful manufacturing and handling of NIF laser glasses.

Gain, Stored Energy, and Extraction Efficiency

The amplification of a laser pulse passing through a laser gain medium (e.g., laser glass) of length z can be modeled using the well-known Frantz–Nodvik equation.[10] This equation relates the output fluence F_{out} to the input fluence F_{in}, given the small-signal gain G_0 and saturation fluence F_{sat} of the laser medium, as follows:

$$F_{out} = F_{sat} \ln\{1 + G_0[\exp(F_{in}/F_{sat}) - 1]\} . \quad (1)$$

The small-signal gain of the laser glass is described by

$$G_0 = \exp\{z[(\sigma N^*) - \alpha]\} , \quad (2)$$

where σ is the emission cross section (cm^2), N^* is the Nd-ion inversion density ($1/cm^3$), and α is the transmission loss coefficient (cm^{-1}). Achieving high net gain requires a high emission cross section coupled with a large population inversion density. In addition, transmission losses due to absorption by impurities or scattering from defects in the glass (or on the polished surfaces) must be kept low relative to the gain.

The term σN^* is the gain coefficient g_L, which is related to the stored energy density ($E_s = h\nu N^*$) and the saturation fluence ($F_{sat} = h\nu_l/\sigma$) of the material:

$$g_L = N^*\sigma = (h\nu_l N^*)\,(\sigma/h\nu_l) = E_s/F_{sat} , \quad (3)$$

where h is Planck's constant (J · s), and ν_l is the laser frequency (Hz). Experimentally, the gain coefficient g_L is measured directly by monitoring the signal gain of a probe beam passing through the glass as it is being pumped in a laser amplifier.[11,12] For example, the large, flashlamp-pumped, glass laser amplifiers used in fusion energy applications typically operate with a gain coefficient of about 0.05 cm^{-1}. The emission cross section is determined independently from spectroscopic measurements. The phosphate glasses used in fusion applications nominally have an emission cross section of about 3.5 to 4.0×10^{20} cm^2, corresponding to a saturation fluence of about 5 J/cm^2. The stored energy in the laser glass is computed from Eq. 3 to be about 0.25 J/cm^3.

Energy extraction from the glass is most efficient at high laser fluences, particularly fluences in excess of twice the saturation fluence. Having a glass with a high emission cross section is desirable because efficient extraction can be achieved at lower fluence, thereby reducing the chance of laser-induced damage to the optics.

Unfortunately, not all of the stored energy in the glass can be extracted, even at very high fluences.[13] This limitation arises from the inhomogeneous broadening of the Nd emission. The cross section calculated from measurements of gain saturation using the Frantz–Nodvik equation give higher emission cross sections (σ_{gs}) than those determined spectroscopically (σ_{em}). The Nd-site inhomogeneities in the glass lead to hole burning, causing the glass to saturate at a lower fluence, corresponding to a higher effective cross section. The extraction efficiency then can be defined by the ratio of the two cross sections:

$$\eta_{ext} = \sigma_{em}/\sigma_{gs} . \quad (4)$$

Phosphate laser glasses tend to saturate much more homogeneously than do silicates; therefore, the efficiency with which the energy is extracted is much higher.[13] This is one of the reasons for the wide use of phosphate glasses in ICF applications. To be more specific, a large fraction of the cost of large fusion research lasers is in the cost of the amplifiers. Therefore, simultaneously achieving high stored energy and efficient extraction is essential to minimize the number and cost of the amplifiers.

A high Nd^{3+} gain cross section is often desirable for ICF laser applications; however, it can also lead to some undesirable effects. For example, for large-aperture laser systems, a high gain coefficient can lead to low energy-storage efficiency and large spatial variations in the gain distribution across the aperture due to amplified spontaneous emission. The general rule of thumb is that the product of the gain coefficient and longest dimension of the laser glass piece should not exceed a value of about 4.2. In addition, the Nd doping and fluorescence lifetime must be optimized to achieve maximum energy-storage efficiency. The tradeoff among high gain, good spatial gain uniformity, and efficient energy storage is quite complex and is usually optimized with the use of sophisticated laser-design computer codes.[14]

Nonradiative Energy Losses

In most practical applications, the quantum yield is never 100% because of nonradiative relaxation mechanisms that

significantly shorten the lifetime. The nonradiative losses are affected by intrinsic properties of the laser glass as well as the care with which the glass is manufactured.[15,16] Figure 2 shows a schematic view of the most important nonradiative mechanisms.

The two most important intrinsic processes are multiphonon relaxation and concentration quenching. Concentration quenching refers to the radiation exchange between a pair of Nd ions. Nd concentration quenching results from the contributions of two relaxation mechanisms. One is cross relaxation in which the two ions share the energy, and the second is migration of the excitation energy from one ion to the next (the so-called "hopping" mechanism). In theory, the rate of relaxation due to concentration quenching varies as $1/r^6$, where r is the inter-ion distance, which is equivalent to the square of the Nd^{3+} concentration. In reality, the effect of the Nd concentration on relaxation rate is highly glass dependent and varies from nearly linear to quadratic in phosphates and from quadratic to cubic in silicates.[15–18] Stokowski,[15] and more recently Payne et al.,[18] have proposed an empirical relation to characterize concentration quenching in metaphosphate laser glasses:

$$\tau_{em} = \tau_0/[1 + (N/Q)^2] \, , \qquad (5)$$

where τ_0 is the zero concentration lifetime (μs), N is the Nd^{3+} ion concentration (ions/cm^3), and Q (ions/cm^3) is an empirically determined quantity for a given glass. Q is physically equivalent to the Nd concentration needed to reduce the lifetime τ_{em} to one-half its zero concentration limit.

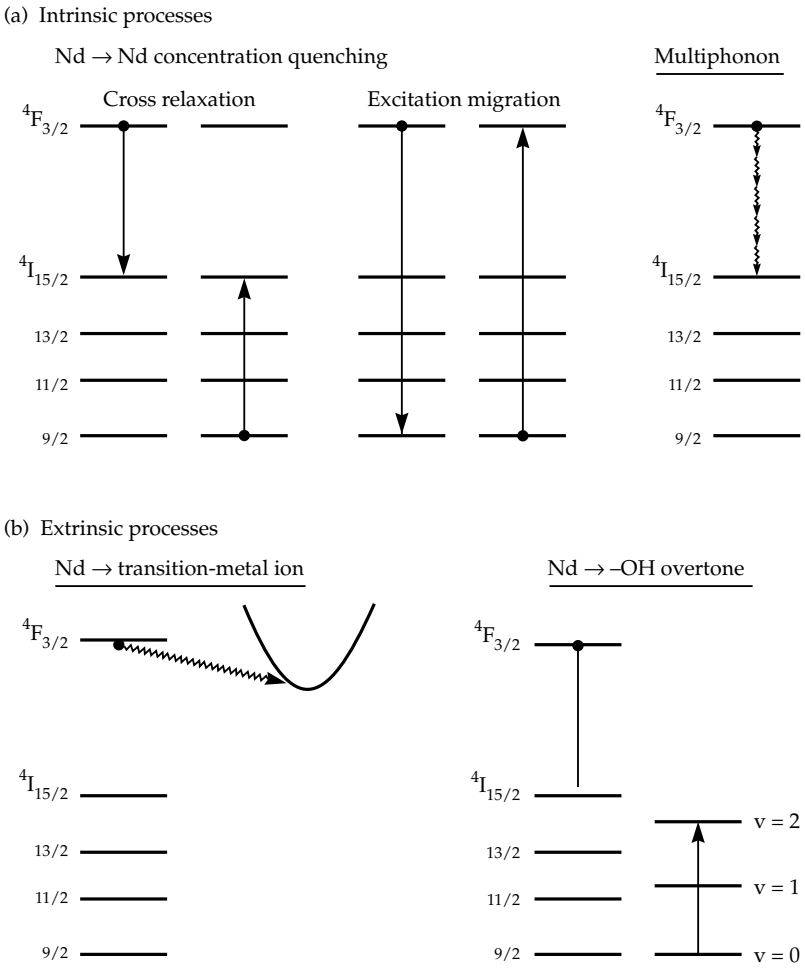

FIGURE 2. Nonradiative Nd^{3+} relaxation processes in laser glasses can be divided into (a) intrinsic processes that depend on glass composition and structure and (b) extrinsic processes that depend on doping density and impurities in the laser glass. Extrinsic losses depend strongly on processing methods. (40-00-0596-1135pb02)

The rate of multiphonon relaxation depends on how closely the $^4F_{3/2}$-to-$^4I_{15/2}$ energy transition (5500 cm^{-1}) matches the maximum vibration energy of the glass matrix.[15,16,19] For phosphate glasses, the maximum vibration energy is about 1170 to 1200 cm^{-1} (References 20 and 21), thus suggesting the absence of any significant multiphonon effects. Careful measurements by Caird et al.[16] on two commercial phosphate glasses (LG-750 and LG-760) support this observation. The measured multiphonon relaxation rate is about 200 s^{-1}.

It is well known that impurities that enter the glass during manufacturing (particularly hydroxyl groups and transition-metal ions) can cause significant nonradiative relaxation. Some useful correlations have recently been reported for estimating the impact of various impurities on the nonradiative relaxation rate in phosphate glasses.[22] We hasten to add, however, that the problems associated with impurities have been largely eliminated in modern laser glass manufacturing by the proper choice of raw material and melting equipment.

Nonlinear Refractive Index

The energy extraction efficiency for ICF laser systems is also limited by nonlinear propagation effects, particularly at very short pulse lengths. The refractive index increases with the laser intensity:

$$n = n_0 + \gamma I \ , \tag{6}$$

where γ is the nonlinear refractive index coefficient (m^2/W), and I is the laser intensity (W/m^2). The intensity-dependent index can cause amplitude ripples (noise) that occur at certain spatial frequencies to grow exponentially:

$$I = I_0 \exp(B) \ , \tag{7}$$

where the B factor (or breakup integral) is the cumulative nonlinear phase retardation over the optical path length:

$$B = 2\pi/\lambda \int \gamma I \, dz \ . \tag{8}$$

Experience has shown that B needs to be less than about 2 rad to avoid unacceptable noise ripple growth.[23,24] Such growth can cause optical damage and/or degrade the beam focus. Therefore, laser glasses with low nonlinear indices are required for ICF applications.

Direct measurement of γ is difficult, so empirical correlations have been developed. The expression developed by Boling et al.[25] many years ago accurately predicts γ from the refractive index n_d and the Abbe number ν of the glass:

$$\gamma = K(n_d - 1)(n_d^2 + 2)^2 / \{n_d \nu[1.52 + (n_d^2 + 2)(n_d + 1)\nu/6\, n_d]^{1/2}\}, \tag{9}$$

where $K = 2.8 \times 10^{-10}$ m^2/W is an empirically determined constant. The nonlinear refractive index n_2 (in esu) is related to γ by $n_2 = \gamma(nc/40\pi)$, where c is the speed of light.

Optical Quality

Some of the most critical specifications of laser glass relate to its optical quality, and the relevant characteristics are strongly dependent on the processing conditions. In particular, three main characteristics of the glass impact optical quality: optical homogeneity, inclusions, and bubbles.

Optical homogeneity refers to the refractive index variation in the optical material. For laser glass, the value is typically less than 2 ppm (i.e., $\Delta n < \pm 2 \times 10^{-6}$). Homogeneity is generally specified in terms of a maximum amount of allowed aberration due to sphere, astigmatism, and a smaller amount of higher-order terms (see Table 2). For the NIF and LMJ, we intend to keep the same specification. However the final, finished (i.e., polished) laser glass will be specified using a more sophisticated procedure designed to monitor aberrations at specific spatial frequencies that are known to seed nonlinear growth of intensity noise in the laser beam.

The homogeneity of the laser glass is critical to maintain wavefront uniformity

TABLE 2. Key technical specifications for the NIF prefinished laser glass slabs. Prefinished slabs will be clad, ground, and polished into finished slabs by the finishing vendor.

Parameter	NIF specification
Nd doping	$4.2 \times 10^{20} \pm 0.1$ Nd^{3+}/cm^3
Homogeneity (expressed as wavefront error at 632 nm, normal incidence)	
– Sphere	$< 0.425\ \lambda$
– Astigmatism	$< 0.220\ \lambda$
– Higher-order aberrations	$< 0.142\ \lambda$
Fluorescence lifetime (measured on $5 \times 5 \times 0.5$ cm^3 sample)	≥ 320 μs
Absorption coefficients	
– At 1053 nm	≤ 0.0019 cm^{-1}
– At 400 nm (due to Pt^{n+})	≤ 0.25 cm^{-1}
– At 3333 nm (due to hydroxyl groups)	≤ 2 cm^{-1}
Bubbles	
– Maximum number (per 100 cm^2 area)	Total cross section <0.15 mm^2
– Maximum diameter	≤ 100 μm
Birefringence	≤ 5 nm/cm
Pt inclusions	
– Maximum number for any one slab	≤ 5 in clear aperture
– Average for all slabs	≤ 2 per slab
– Maximum size after laser irradiation (5 shots per site)	≤ 100 μm

of the laser beam. Recall that there are a total of 16 laser slabs in the laser beamline, and during multiple passes through the cavity and booster amplifier sections, the beam passes through the equivalent of 54 laser slabs. Therefore, even small optical inhomogeneities can lead to significant wavefront aberration in the output of the beam, potentially causing significant degradation in both frequency conversion and focusability of the beam.

Inclusions from ceramic refractory materials, unmelted raw materials, platinum (Pt) metal, crystallites, or impurities can cause optical damage in the glass when exposed to high laser fluences. The most common inclusion source is metallic Pt inclusions from the Pt liners used in the melting system. Improved processing conditions have led to a dramatic reduction in Pt inclusions in recent years such that the average inclusion density is less than 0.1 per liter of glass, or less than an average of 1 to 2 per glass slab.[26,27] Inclusions in laser glass typically damage at about 2 to 5 J/cm^2 at the NIF and LMJ pulse lengths.[28] Although very small to begin with, inclusion damage can grow with successive laser shots to several millimeters or even centimeters in size, making the laser glass unusable. Large damage spots in laser glass can seed damage in other optics in the laser chain. In general, if the inclusions are small, they can be tolerated as long as the optical damage they produce does not exceed about 250 μm in size. This limit is the basis for the specification given in Table 2. Currently, we scan each piece of laser glass with a high-fluence laser beam and measure the size of any damage site after a specified number of shots at fluences between 7 to 14 J/cm^2 (8 ns).[29–31] If the Pt-damage size remains below the specified size limit given in Table 2, then it is acceptable.

New processing techniques for eliminating Pt inclusions rely on the intrinsic property of many phosphate glasses to dissolve Pt metal under oxidizing conditions. Izumitani et al.[32] have reported the use of gaseous $POCl_3$ as an oxidizing additive, and Campbell and coworkers at Hoya Corporation (Fremont, Calif.) and Schott Glass Technologies, Inc. (Duryea, Pa.)[26–28] have reported the effects of O_2, Cl_2, CCl_4, and N_2/O_2 mixtures. Model predictions of Pt-inclusion dissolution rates agree well with results from glass-melting tests.[33]

The effects of glass composition on Pt solubility have been reported to follow the trend: phosphate > silica-phosphate >> fluorophosphate > silicate.[32] These results are based on solubility measurements using LHG-5 and LHG-8 (phosphates), HAP-3 (silica-phosphate), LHG-10 (fluorophosphate), and LSG-91H (silicate).

If inclusions are eliminated from the bulk laser glass, the damage threshold is limited only by the quality of the surface finish.[34] This is shown in Figure 3, where surface damage threshold is plotted versus pulse length for various laser glasses as well as fused silica. The pulse-length dependence of the surface damage threshold for finely polished samples can be accurately represented by the empirical expression

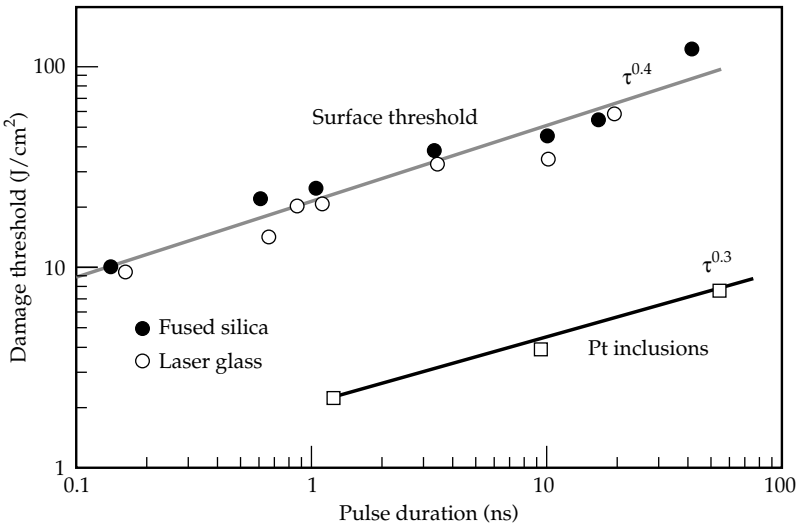

FIGURE 3. Measured surface-damage threshold for various polished laser glasses and fused silica vs pulse length at 1053 nm. The bulk-damage thresholds also shown arise from Pt inclusions, as reported by Gonzales and Milam.[35]
(40-00-0596-1133pb02)

$$D_s\,(\mathrm{J/cm^2}) = 22 t_p^{\,0.4}\,, \qquad (10)$$

where t_p is the pulse length (ns). The surface damage threshold approximately follows the $t^{1/2}$ relation predicted by a thermal-diffusion heat-transport model. For comparison, the damage threshold reported by Gonzales and Milam[35] for Pt inclusions is also shown in Figure 3. It follows the approximate pulse-length scaling relation

$$D_{Pt}\,(\mathrm{J/cm^2}) = 2.5 t_p^{\,0.3}\,. \qquad (11)$$

Thus, the presence of Pt inclusions reduces the operating limit of the laser glass by nearly tenfold.

The specification for laser glass bubbles is based on two requirements. The first is the need to minimize the amount of light loss due to obscurations caused by bubbles. The second is the need to keep the size below a certain value that may induce nonlinear growth of intensity noise. The obscuration loss is not to exceed 0.01% of the beam area per slab and therefore sets the total number of bubbles of a given size allowed in any given slab. The maximum-size bubble allowed is currently 100 μm. The diffracted light from bubbles that exceed 100 μm can, at high intensities, imprint a holographic diffraction pattern in the next optic that, in turn, can bring that portion of the beam to focus at another downstream optic and potentially damage it. Because of the regular spacing of many optics in the laser chain, such a nonlinear imaging effect could lead to propagation of laser damage throughout the beamline. In general, bubbles have not been a significant problem for laser glass. For example, only one of the Beamlet slabs had bubbles, and they were so few in number and so small as to be insignificant.[9] Similar results were observed for the Nova and Phebus laser glass disks.

Properties of the NIF and LMJ Laser Glasses

Laser glasses are specially formulated to give the desired laser, optical, thermal–mechanical, and physical–chemical properties needed for a specific laser application. Some properties are strongly affected by the processing conditions as discussed above; however, most are controlled by the base glass composition.

We have chosen two glasses for use on the NIF and LMJ that meet the gain, energy-storage, extraction-efficiency, and damage-resistance requirements: LHG-8 (Hoya Corporation) and LG-770 (Schott Glass Technologies, Inc.). LHG-8 is the same

TABLE 3. Properties of LHG-8 (Hoya) and LG-770 (Schott) laser glasses.

Glass properties	Symbol	LHG-8	LG-770
Optical			
Refractive index at 587.3 nm	n_d	1.52962	1.50674
Refractive index at 1053 nm	n_1	1.52005	1.49908
Nonlinear refractive index			
n_2 (10^{-13} esu)	n_2	1.12	1.01
γ (10^{-20} m^2/W)	γ	3.08	2.78
Abbe number	ν	66.5	68.4
Temp. coefficient refract. index (10^{-6}/K)	dn/dT	–5.3	–4.7
Temp. coefficient optical path (10^{-6}/K)	δ	0.6	1.2
Laser			
Emission cross section ($10^{-20}cm^2$)	σ_{em}	3.6	3.9
Saturation fluence (J/cm^2)	F_{sat}	5.3	4.8
Radiative lifetime (zero Nd) (μs)	τ_0	365	372
Judd–Ofelt radiative lifetime (μs)	τ_r	351	349
Judd–Ofelt parameter ($10^{-20}cm^2$)	Ω_2	4.4	4.3
Judd–Ofelt parameter ($10^{-20}cm^2$)	Ω_4	5.1	5.0
Judd–Ofelt parameter ($10^{-20}cm^2$)	Ω_6	5.6	5.6
Emission bandwidth (nm)	$\Delta\lambda_{eff}$	26.5	25.4
Concentration quenching factor (cm^{-3})	Q	8.4	8.8
Fluorescence peak (nm)	λ_L	1053	1053
Thermal			
Thermal conductivity (W/mK)	k	0.58	0.57
Thermal diffusivity(10^{-7} m^2/s)	α	2.7	2.9
Specific heat (J/gK)	C_p	0.75	0.77
Coefficient thermal expansion (10^{-7}/K)	α_e	127	134
Glass transition temperature (C)	T_g	485	461
Mechanical			
Density (g/cm^3)	ρ	2.83	2.59
Poisson's ratio	μ	0.26	0.25
Fracture toughness (MPa • $m^{0.5}$)	K_{1C}	0.51	0.43
Hardness (GPa)	H	3.43	3.58
Young's modulus (GPa)	E	50.1	47.3

glass as that used on the Nova and Phebus lasers. However, LG-770 is a new formulation developed to replace the LG-750 glass that was used on Nova, Phebus, and Beamlet. Table 3 summarizes the key properties of these laser glasses. Figure 4 shows the neodymium absorption and emission spectra for the two glasses, confirming that the glasses are essentially indistinguishable. In fact, for nearly all properties, the two glasses closely match, thereby making it possible for us to randomly interchange the two glass types within the NIF amplifiers without affecting laser performance.

Description of Glass Melting

Glasses made for the present, large ICF laser systems (e.g., Nova at LLNL, Phebus at CEA, Beamlet at LLNL, Gekko at Osaka, and OMEGA at the University of Rochester) were manufactured using a one-at-a-time, discontinuous melting process. We briefly describe this older manufacturing method and then discuss the new, advanced processes that have been developed for the NIF and LMJ.

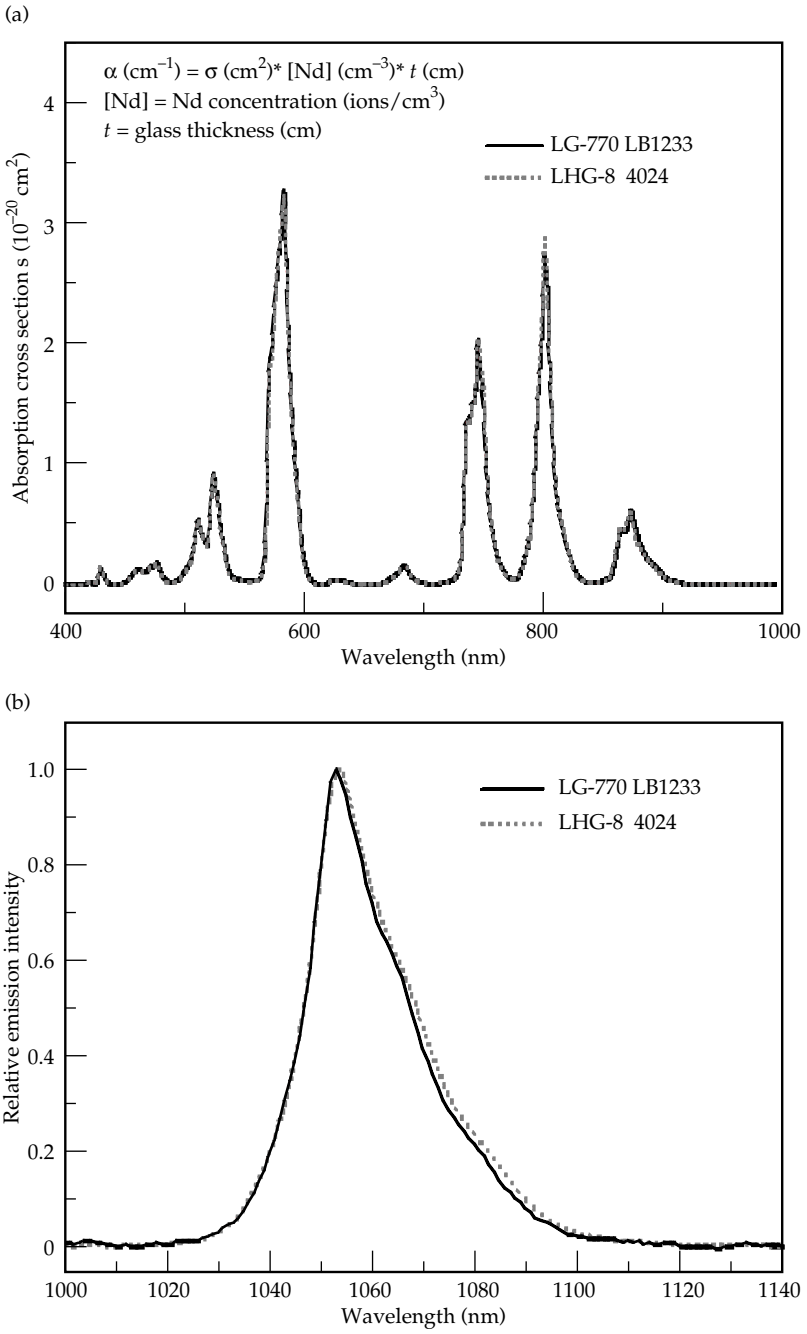

FIGURE 4. The (a) absorption and (b) emission spectra for LG-770 and LHG-8 laser glass are virtually indistinguishable.
(40-00-0299-0428pb02)

Old Technology: One-at-a-Time, Discontinuous Melting and Forming

The first step of the discontinuous process is premelting (Figure 5), which is designed to melt and mix on a large-scale length the raw starting materials. A bubbling gas is often added to remove unwanted volatile products, particularly water, and if necessary, to adjust the melt redox state. The premelt is carried out in a relatively inert refractory crucible. The walls of the refractory vessel corrode over time, eventually

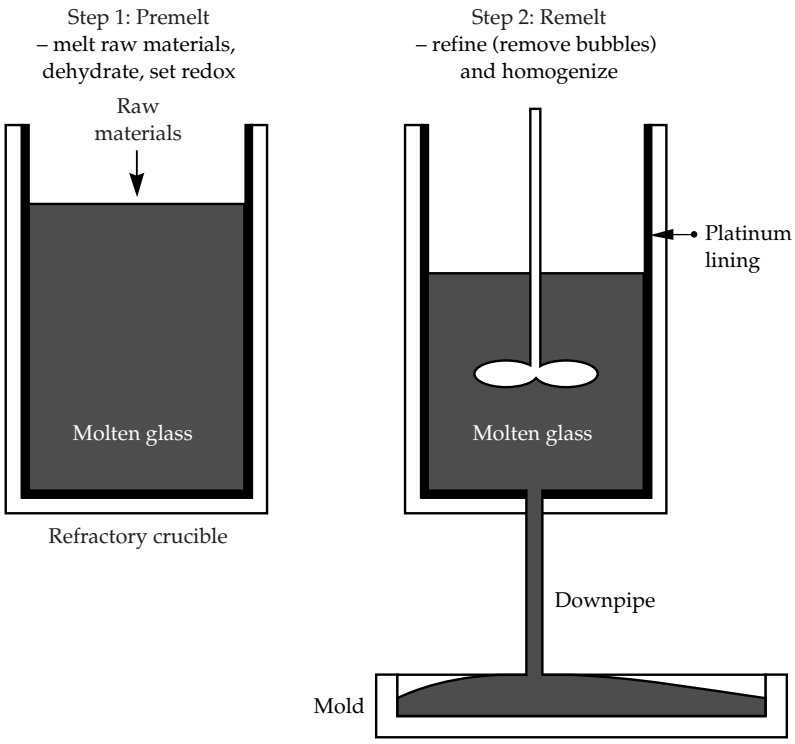

FIGURE 5. Schematic of the current, discontinuous, two-step process used to melt and form laser glass slabs. (40-00-0496-0936pb03)

requiring the vessel to be replaced. Glass from the premelter generally contains bubbles, striae, and possibly some small particles of unmelted starting material.

Product glass from the premelt stage is next processed in a physically separate unit called the remelter. The remelter consists of a platinum-lined vessel that also has provisions for stirring and gas bubbling. The main purposes of the remelter are to dissolve any Pt inclusions, remove any bubbles, and homogenize the glass to provide the striae-free, high-optical-quality glass necessary for laser applications. This process involves several stages.[36] During the first stage of the remelt cycle, the redox state of the glass is adjusted to enhance Pt-particle dissolution. Next, a refining or "fining" process is conducted at high temperatures, where the viscosity of the glass is low, allowing bubbles to rise to the surface. The third stage is a stirring process that is generally conducted at temperatures lower than those for either the melting or refining stages. Continuous stirring thoroughly distributes all components within the glass melt, eliminating striae and thus ensuring uniformity of the refractive index over the entire casting. Finally, the melt is cooled to a temperature such that the viscosity of the glass is proper for casting into a mold of the appropriate size and shape. After casting, the glass undergoes a coarse annealing step, is inspected for inclusions and striae, and then is fine-annealed to remove residual thermal stresses due to the forming process. Although it only takes one or two days to melt and cast each slab, it can take several months to complete the subsequent annealing and inspection.

Advanced Technology: Continuous Laser Glass Melting and Forming

Advanced laser glass melting processes have been developed separately by Schott Glass Technologies, Inc., and Hoya Corporation under work funded jointly by LLNL and the Centre d' Etudes de Limeil-Valenton. The two glass companies have chosen different development approaches. Schott has chosen to design and develop a full-scale melting system

that will then become the production melter. The Schott approach allowed for one development run to verify equipment design and the melting and forming process. Such verification was completed in November and December 1997. In contrast, Hoya chose to carry out development using a subscale, continuous melter. Because of the smaller size and lower operating costs of their equipment, Hoya was able to carry out several melting and forming campaigns, which were completed in March 1998. Both vendors have completed their development efforts, and as of February 1999, they are in the midst of the first production run that we term the "pilot." This work will be followed by several years of production, approximately 2 to 3 years for the NIF and about 3 to 4 years for LMJ.

Many details of the manufacturing process are highly proprietary to each company. Therefore, we give only a generic description of the melting, forming, and coarse annealing process. Nevertheless, this description should provide an idea of the progress in laser glass manufacturing technology that has occurred as a result of the NIF and LMJ projects. The laser glass melting systems developed by Schott and Hoya are arguably the most advanced optical glass melting systems in the world.

As shown in Figure 6, a continuous optical glass melting system is generally divided into several interconnected zones. Each zone consists of one or more vessels designed to carry out a specific aspect of the process. For laser glass continuous melters, Figure 6 shows the six main processing zones,[37] which are raw material batching, melting, conditioning, refining, homogenizing, and continuous strip forming. The six regions are interconnected, allowing for a continuous flow of glass from one zone to the next.

It is desirable that the raw materials be batched together and then thoroughly mixed in a dry atmosphere. The batch is then delivered continuously to the melter with precautions to avoid water uptake by hydroscopic raw materials. Batch powder that enters the melter dissolves in the molten glass and undergoes large-scale mixing. Off-gas handling equipment collects any gas emissions from the melter (or other vessels) and treats the effluent to meet environmental regulations.

Glass continuously flows from the melter into the conditioning unit, where the redox state of the melt is adjusted to enhance dissolution of Pt inclusions. If required, steps may also be taken to remove any excess "water" (i.e., hydroxyl groups) in the glass. Glass from the conditioning unit then flows to the refiner

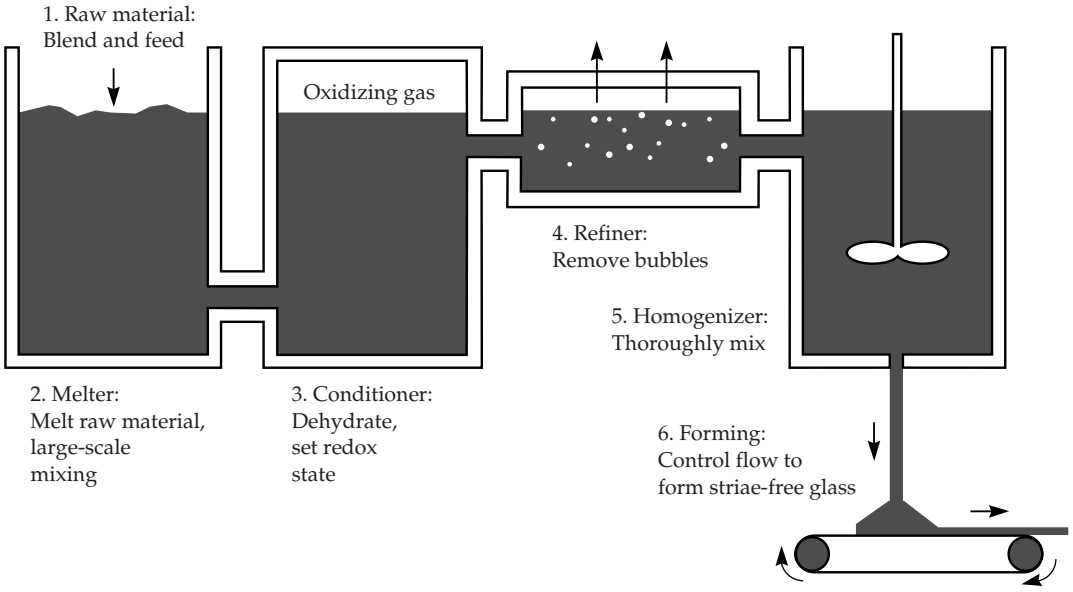

FIGURE 6. Schematic of the continuous laser-glass melting systems to be used to manufacture NIF and LMJ laser glass. The six process zones are discussed in the text. (40-00-0997-2077pb02)

section where the temperature is generally elevated to reduce the glass viscosity and thereby increase the bubble rise velocity to promote bubble removal.

Glass from the refiner enters the homogenizing section, where Pt stirrers thoroughly mix the glass to achieve the part-per-million index homogeneity required for ICF laser applications. Just as in the discontinuous process, the temperature of the homogenizing section is reduced to adjust the glass viscosity to give the desired flow characteristics needed to form a wide, thick, homogeneous strip of glass. The width and thickness of the glass strip produced during the forming operation are greater than those of any optical glass ever produced prior to NIF- and LMJ-driven glass development.

The glass manufacturers employ highly proprietary technology to "form" (i.e., cast) the glass into a homogeneous, continuous strip free of sharp index variations (striae). Once successfully formed, the cast strip moves by conveyor belt through a long (25- to 35-m), coarse annealing oven (Figure 7) where the temperature is ramped down at a rate to avoid generating unacceptable thermal stresses in the glass. Finally, the cast strip is cut into pieces that are individually processed to give the desired laser slab blank.

Both manufacturers will use advanced processing conditions designed to minimize the formation of Pt inclusions in laser glass. Prior to 1986, Pt inclusion damage represented the major source of damage in laser glass used for high-peak-power applications. However, new processing methods effectively reduce the Pt inclusion concentration by more that 1000-fold, to fewer than an average of 1 to 2 per laser glass slab (i.e., less than 0.1 per liter).

Postprocessing

Once the laser glass has been melted and formed into plates, several other process steps must be completed before the glass can be shipped to the final finishing vendor. Specifically, the laser glass needs to undergo prefabrication to a size suitable for inspection for striae and Pt inclusions. Next, the glass is slowly annealed to remove any residual strain, a process that can take many days. Finally, the glass blank is fabricated to the final dimensions, inspected for homogeneity, and prepared for shipping.

Manufacturing Schedule

Laser glass manufacturing for the NIF and LMJ is divided into two main phases: pilot and production. Pilot refers to the

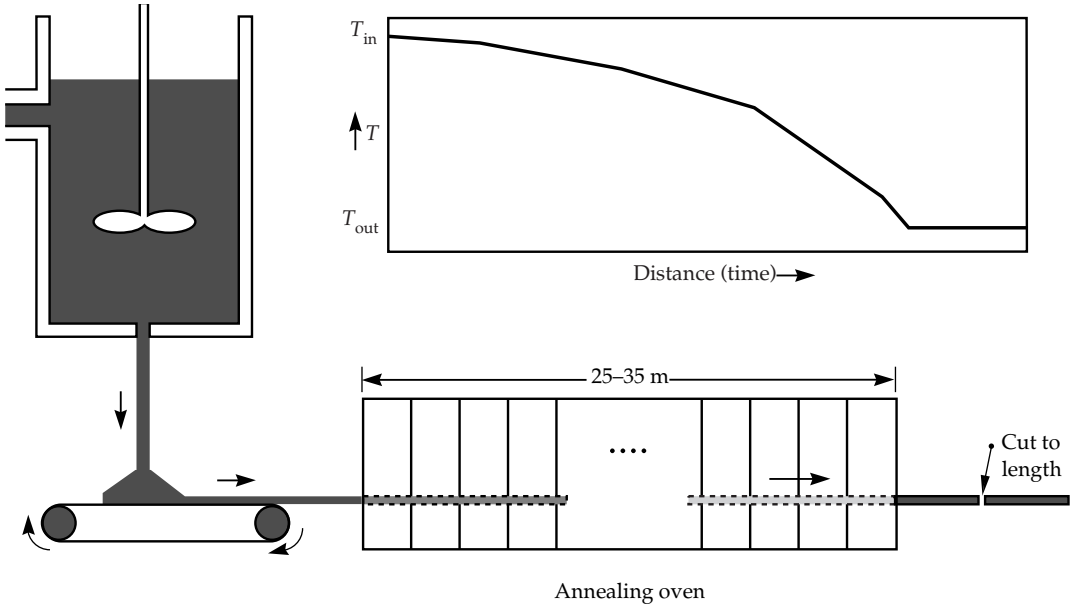

FIGURE 7. Schematic of the system used to coarse-anneal the as-cast, continuous laser glass strip. (40-00-0299-0429pb01)

first production run. Results from the pilot run will be used to establish yield and costs. In addition, glass from the pilot run will be used by the finishing vendors to demonstrate the advanced laser glass finishing and polishing methods to be used in final production.

The production phase immediately follows the pilot phase. The first stage of laser glass production will be primarily for the NIF facility because NIF construction will occur earlier than that for the LMJ. The NIF production will take place over approximately three years at a rate of about 1200 slabs per year. NIF production will be followed by LMJ production, which will last three to four years. During the third year of production, the NIF and LMJ may overlap somewhat, requiring a short-term increase in the annual production rate.

Summary

The NIF and LMJ laser systems require about 3380 and 4752 Nd-doped laser glass slabs, respectively. Continuous laser glass melting and forming will be used for the first time to manufacture these slabs. Two vendors have been chosen to produce the glass: Hoya Corporation and Schott Glass Technologies, Inc. The laser glass melting systems that each of these two vendors have designed, built, and tested are arguably the most advanced in the world. The cost goal is to manufacture the laser glass for about $1000/L ($350/kg), or roughly a factor of 3 lower than the cost associated with current, one-at-a-time production methods. Production of the laser glass began on a pilot scale in the fall of 1998.

Acknowledgments

The authors gratefully acknowledge J. Hayden, A. Thorne, H. Pankratz, J. Cimino, and their colleagues at Schott Glass Technologies, Inc., and K. Takeuchi, M. Smolley, J. Storms, and their colleagues at Hoya Corporation for their fine efforts in developing the advanced laser glass processes needed to produce the laser glass for the NIF and LMJ. Our close collaboration with Ms. Gaëlle Ficini–Dorn and her colleagues at the French CEA is gratefully acknowledged.

Notes and References

1. J. Paisner and J. R. Murray, "Overview of the National Ignition Facility Project," *Proc. SPIE Conf. Solid-State Laser Apps. to ICF* (Monterey, CA, 1998).
2. M. Andre, "LMJ and LIL," *Proc. SPIE Conf. Solid-State Laser Apps. to ICF* (Monterey, CA, 1998).
3. *National Ignition Facility Conceptual Design Report*, vol. 2 and 3, Lawrence Livermore National Laboratory, Livermore, CA, UCRL-PROP-117093 (May 1994).
4. M. Andre, *Chocs, Revue Scientifique et Technique de la Direction de Applications Militaires* **11**, 82–85 (July 1994).
5. A. C. Erlandson, M. D. Rotter, D. N. Frank, and R. W. McCracken, *Inertial Confinement Fusion Quarterly Report* **5**(1), 18–28, Lawrence Livermore National Laboratory, Livermore, CA, UCRL-LR-105821-95-1 (1994).
6. A. Erlandson et al., "Flashlamp-Pumped Nd:Glass Amplifiers for the National Ignition Facility," *Proc. 13th Embedded Topical Meeting on the Technology of Fusion Energy* (American Nuclear Society, 1998).
7. L. Zapata et al., "Gain and Wavefront Measurements Performed on the NIF/LMJ Prototype Amplifiers," *Proc. SPIE Conf. Solid-State Laser Apps. to ICF* (Monterey, CA, 1998).
8. B. M. Van Wonterghem et al., *Applied Optics* **36**, 4932 (1997).
9. J. H. Campbell et al., *Inertial Confinement Fusion Quarterly Report* **5**(1), 29–41, Lawrence Livermore National Laboratory, Livermore, CA, UCRL-LR-105821-95-1 (1994).
10. L. M. Frantz and J. S. Nodvik, *J. Appl. Phys*. **34**, 2346–2349 (1963).
11. H. T. Powell, A. C. Erlandson, K. S. Jancaitis, and J. E. Murray, *High Power Solid State Lasers and Applications*, *SPIE Proc.* **1277**, 103–120, Bellingham, WA (1990).
12. A. C. Erlandson, K. S. Jancaitis, R. W. McCracken, and M. D. Rotter, *Inertial Confinement Fusion Quarterly Report* **2**(3), Lawrence Livermore National Laboratory, Livermore, CA, UCRL-LR-105821-94-3 (1994).
13. W. E. Martin and D. Milam, *IEEE J. Quantum Electron*. **OE18**, 1155–1163 (1982).
14. *National Ignition Facility Conceptual Design Report*, vols. 2 and 3, Lawrence Livermore National Laboratory, Livermore, CA, UCRL-PROP-117093 (May 1994).
15. S. E. Stokowski, *Laser Glass: An Engineered Material*, Lawrence Livermore National Laboratory, Livermore, CA, UCRL-96331 (1987).
16. J. A. Caird, A. J. Ramponi, and P. R. Staver, *J. Opt. Soc. Am*. B **8**, 1391 (1991).
17. S. A. Payne, C. D. Marshall, A. Bayramian, G. D. Wilke, and J. S. Hayden, *Appl. Phys. B* **61**, 257–266 (1995).

18. S. A. Payne et al., *Ceramic Transactions: Solid State Optical Materials* **28**, 253–260, American Ceramic Society Press (1992).
19. C. B. Layne, W. H. Lowdermilk, and M. J. Weber, *Phys. Rev. B* **16**, 10 (1977).
20. H. Toratani, *Properties of Laser Glasses*, Ph.D. Thesis, Kyoto University, Japan, (1989).
21. H. Toratani, I. Izumitani, and H. Kuroda, *J. Non-Cryst. Solids* **52**, 303–313 (1982).
22. J. H. Campbell, "Recent Advances in Phosphate Laser Glasses for High-Power Applications," *Inorganic Optical Materials*, P. Klocek, Ed., SPIE **CR64**, 3–39 (1996).
23. J. T. Hunt and D. R. Speck, *Optical Engineering* **28**, 461–468 (1989).
24. J. T. Hunt, K. R. Manes, and P. A. Renard, *Appl. Optics* **32**, 5973–5982 (1993).
25. N. L. Boling, A. J. Glass, and A. Owyoung, *IEEE J. Quantum Electron.* **QE14**, 601 (1978).
26. J. H. Campbell, E. P. Wallerstein, J. S. Hayden, D. L. Sapak, and A. J. Marker, *Glastech. Ber. Glass Sci. Technol.* **68**(1), 11–21 (1995).
27. J. H. Campbell, E. P. Wallerstein, H. Toratani, H. Meissner, and T. Izumitani, *Glastech. Ber. Glass Sci. Technol.* **68**(2), 1–11 (1995).
28. J. H. Campbell et al., *Elimination of Platinum Inclusions in Phosphate Laser Glasses*, Lawrence Livermore National Laboratory, Livermore, CA, UCRL-53932 (1989).
29. C. L. Weinzapfel et al., "Large-Scale Damage Testing in a Production Environment," *Laser Induced Damage in Optical Materials: 1987* (NIST Special Publication 756, National Institute of Standards and Technology, 1987), pp. 112–122.
30. J. H. Campbell, J. F. Kimmons, and S. Schwartz, "Platinum Particle Detection in Phosphate Laser Glass," *Analysis of the Composition and Structure of Glass and Glass Ceramics* (Springer-Verlag, Heidelberg, 1999), Chapter 6.6.
31. S. Schwartz et al., "Vendor-Based Laser Damage Metrology Equipment Supporting the National Ignition Facility," *Proc. SPIE Conf. Solid-State Laser Apps. to ICF* (Monterey, CA, 1998).
32. T. Izumitani, M. Matsukawa, and H. Miyade, "Solubility of Pt in Nd Phosphate Laser Glass," *Laser Induced Damage in Optical Materials: 1987* (NIST Special Publication 756, National Institute of Standards and Technology, 1987), pp. 29–34.
33. J. H. Campbell, *Glass Sci. Technol.* **68**, 91–101 (1995).
34. J. H. Campbell et al., "Damage Resistant Optics for a Mega-Joule Solid-State Laser," *Laser Induced Damage in Optical Materials: 1990*, *SPIE* **1441**, 444–456 (1990).
35. R. Gonzales and D. Milam, *Laser Induced Damage in Optical Materials: 1985*, NBS Special Publication 745 (1988), pp. 128–137.
36. A. J. Marker, "Optical Glass Technology," *Geometrical Optics, SPIE Proc.* **531**, 2–10 (1985).
37. T. S. Izumitani, *Optical Glass*, Ch. 3 (American Institute of Physics Translation Series, New York, 1986).

DIFFRACTIVE OPTICS FOR THE NIF

J. A. Britten *M. C. Rushford* *L. Auyang*

S. N. Dixit *L. J. Summers* *I. M. Barton*

S. M. Herman *T. G. Parham* *B. W. Shore*

The National Ignition Facility's (NIF's) baseline laser design incorporates three diffractive structures in the third-harmonic (351-nm) final optics assembly, as shown in Figure 1. These are (1) a focusing beam sampling grating (BSG)[1] for sending a known fraction (0.2 to 0.4%) of the transmitted light into a calorimeter for energy diagnostics; (2) a color separation grating (CSG)[2–5] that transmits, with high-efficiency, third-harmonic light to the target, while directing the unconverted first and second harmonic light away from it, and; (3) a kinoform phase plate (KPP)[6] that smoothes the beam within a super-Gaussian envelope with a tailored spot size at the target plane. The optics' apertures are nominally 40 cm square. To withstand the design fluence, the

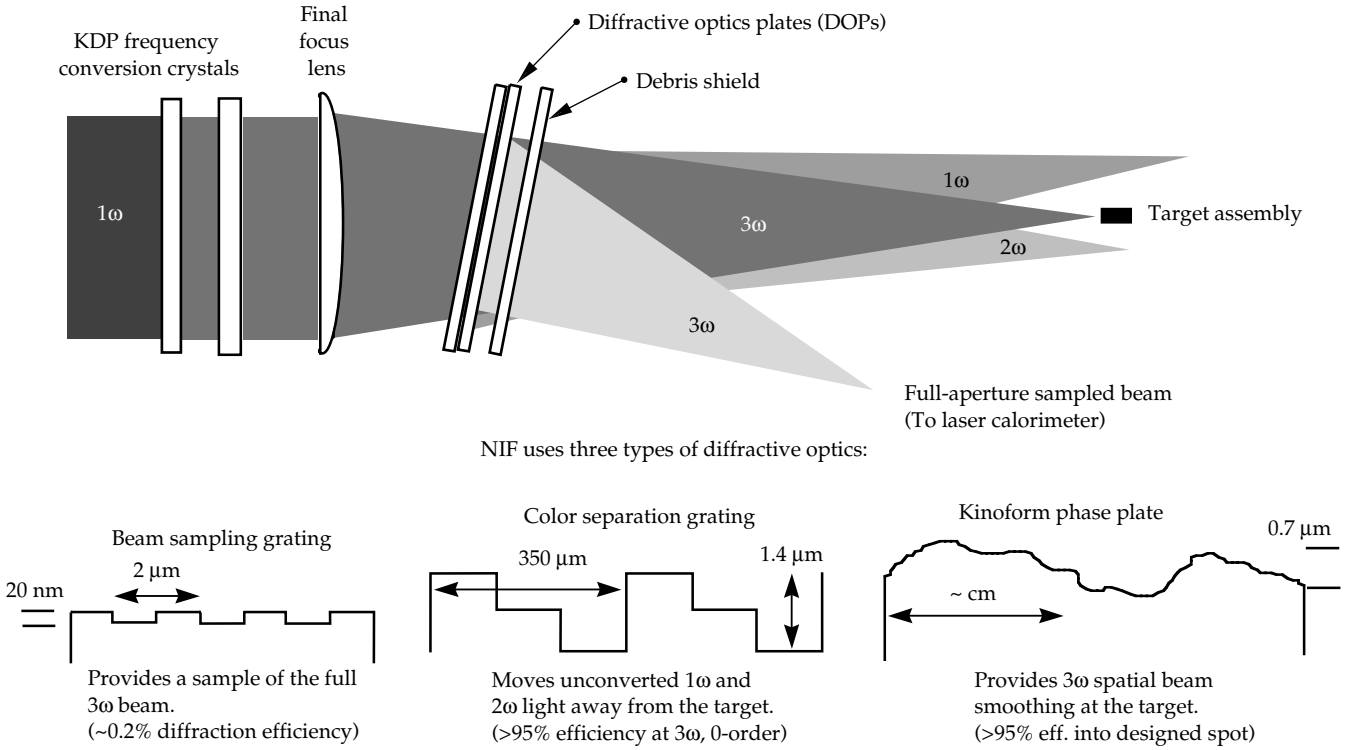

FIGURE 1. Schematic diagram of a NIF final optics assembly, showing the diffractive optics' location, element geometry, and specifications. (70-00-0399-0765pb01)

diffractive structures' patterns must be etched into the bulk fused-silica substrate. Wet chemical etching by a buffered hydrofluoric acid (HF) solution was chosen as the pattern transfer method because (1) the low aspect ratio of these structures is conducive to this process; (2) the process is inherently spatially uniform due to the kinetic control of the dissolution,[7,8] and; (3) it is inexpensive to implement. A flowchart of the processing steps used to manufacture the optics is shown in Figure 2.

The BSG is a lamellar grating with a nominal period of from 1 to 3 μm and a modulation depth of about 20 nm. It is made holographically by projecting two interfering coherent spherical waves onto the photoresist-coated substrate in the appropriate geometry. (These two waves simulate the main beam being focused onto the target and the sampled beam being focused into a calorimeter.) The resulting latent image is developed to give a grating mask in resist. This pattern is transferred to the surface of the substrate by etching the exposed areas between the resist grating lines with HF solution.

The CSG is a stairstep grating design.[2–5] It is made by proximity printing one line of the period through a chrome-on-quartz master mask onto a photoresist layer on the target substrate, developing this pattern, and transfer etching it (again, with HF solution) to a precise depth (equal to one wave of optical phase difference in transmission at the chosen use angle and wavelength). This process is repeated to generate the second line of the period—using the same mask (or a different one) offset laterally, relative to the first line etched.

The KPP is similarly made, by using a four-mask process and transfer wet etching[6] to produce 16 step levels that approximate a continuous, irregular topography over a scale length of several millimeters, with a maximum optical path difference of one wave.

To manufacture diffractive optics plates (DOPs) onsite, we constructed a 2400-ft^2 facility at Lawrence Livermore National Laboratory (LLNL), which became functional in January 1998. During 1998 we fabricated all three types of DOP at NIF sizes, using custom-designed prototype processing equipment and the manufacturing techniques that will be employed for full-scale production. This article focuses on the manufacture and performance of the beam sampling and color separation gratings, two optics that were not previously fabricated at NIF scales. We have made (and reported on) several KPPs for LLNL's Nova laser and other laser systems[6] with processing methods that are identical to those used for the

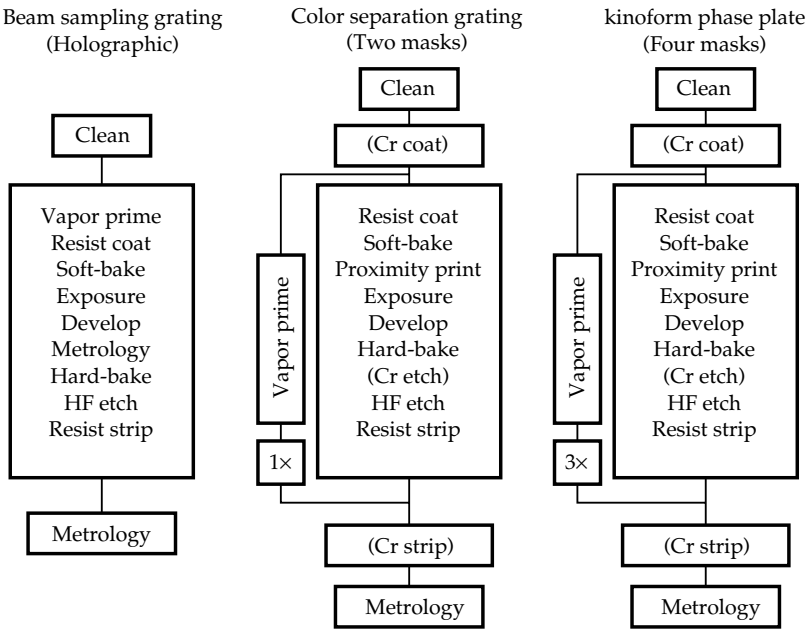

FIGURE 2. Flow diagram of the processing steps required to fabricate the three NIF 3ω diffractive optics. (70-00-0399-0766pb01)

CSG. We also discuss the effects of standard antireflective (AR) coatings on the performance and laser damage characteristics of the diffractive optics, and describe efforts to combine the functionalities of several diffractive elements onto one surface.

The Beam Sampling Grating

A laser interference lithography facility has been constructed at LLNL to fabricate NIF BSGs. Figure 3 shows the geometry of the exposure system. A CW laser with a very long coherence length is required to generate stable, high-contrast fringes in the target plane. We use a 351-nm, Ar-ion laser because its wavelength very closely matches the third harmonic of the NIF. Thus, we can set up exposure geometries that are identical to the deployment geometries in the NIF's final optics assembly and obtain a high-quality focal spot of the diffracted beam with minimal chromatic aberration of the diffracted focus. The laser output in single-mode Tem_{00} operation is about 1.2 W. The exposure table is totally enclosed and is isolated from vibrations by pneumatic supports. Active fringe stabilization is used to ensure high pattern contrast. The major difficulty with this setup is finding suitable high-magnification objectives for transmitting the 351-nm light for the fast-focus sampling beam. All of the multielement objectives tested to date imprint some degree of modulation onto the fringe pattern from defects in the multielement structure, which are difficult to clean and eliminate by spatial filtering.

Using the process outlined in Figure 2, we have made demonstration BSGs on 41- by 39-cm fused-silica plates. A map of the first-order (focused) transmission efficiency of one such grating is shown in Figure 4. This measurement was made at 351 nm with the optic rotated 15° about the vertical axis with respect to the incident beam and with the diffracted beam at an angle of 15° above the optic's horizontal axis; the mean efficiency of 0.37% is within specifications. The spatial uniformity needs to be improved, even though model simulations giving the projected uncertainty of the spatial intensity variations for a NIF beamline suggest that this level of nonuniformity will not contribute substantially to the measurement error. The efficiency variation results from a nonuniform grating linewidth, not an etch-depth variation. The modulation seen in the diffraction efficiency is directly attributable to intensity variations in the spatially filtered, sample-writing beam, using a 40× objective. Improvements to this uniformity will be possible with higher quality objectives.

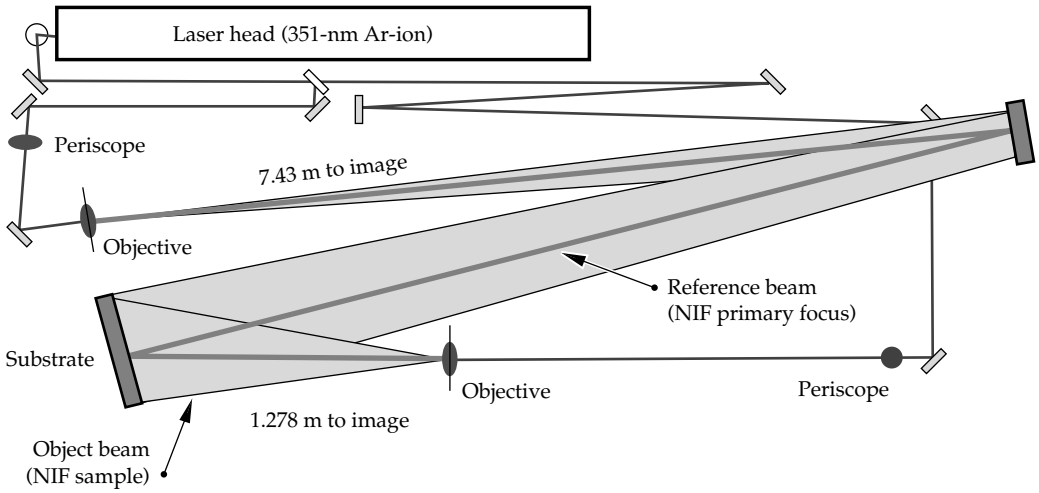

FIGURE 3. Schematic of a NIF beam sampling grating's holographic exposure geometry. (70-00-0399-0767pb01)

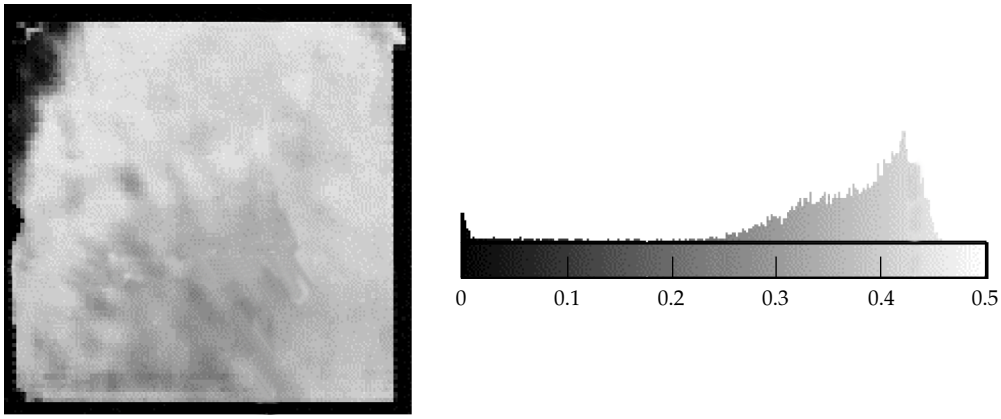

FIGURE 4. Diffraction efficiency (%) at –1 transmitted order, for 351 nm at a 14° incidence angle. The beam sampling grating was manufactured on a 41- × 39-cm fused-silica substrate. The mean efficiency is 0.37%, with a standard deviation of 0.07%. (70-00-0399-0768pb01)

The Color Separation Grating

Several CSGs were fabricated and tested for optical performance. Made by LLNL's laser plotter, the grating mask used for this process consisted of alternating 113-µm-wide clear lines separated by 232-µm-wide chrome spaces, 370-mm long, repeated over a 380-mm field. This pattern was printed on a 65-cm-diam fused-silica substrate. The mask was printed pixel-by-pixel by positioning a 113- by 500-µm-wide aperture with sub-µm accuracy and then, by opening a shutter, exposing the mask (previously coated with an evaporated chrome layer and a photoresist layer) to light from a 413-nm Kr-ion laser. The pattern was transferred to the mask by subsequently developing the resist and etching the exposed chrome.

The CSG target substrates were first coated with chrome and photoresist, and were then exposed through the grating mask to the output of a collimated Hg lamp. Next, the substrates were developed, hard-baked, and chrome-etched. Then, to make the first step, they were HF-etched to a depth of 715±10 nm. To etch the second step (while doubling the depth of the first step) the entire process was repeated, after the mask was laterally shifted 114±1 µm (with the aid of fiducial marks on the mask and by viewing the substrate through confocal microscopes on the mask aligner). During this process, the one- to two-µm undercutting (edge erosion) of the chrome and fused silica edges was taken into account by making the open area of the master mask undersized. The end result was a grating, composed of a series of repeating stairsteps with a 345-µm period, across the clear aperture of the 41- by 39-cm substrate.

A map of the zero-order transmission efficiency of one CSG at 351 nm and 13° incidence angle is shown in Figure 5. The average efficiency was 90.5%. This optic had no antireflective coating, so the maximum theoretical efficiency, accounting for Fresnel losses, is 92.5%. The additional losses, about 2%, are distributed in many higher transmitted diffraction orders. The zero-order transmissions of this optic at 527 nm and 1053 nm are 0.05% and 0.26%, respectively, which exceed NIF specifications for 1ω and 2ω light rejection. We have made several such gratings with similar results.

The Effects of Sol-Gel Antireflective Coatings

Color Separation Gratings

Transmissive optics for LLNL's high-power lasers have for years been coated with high-damage-resistant sol-gel, colloidal-silica, antireflective (AR) films[9] applied by dip coating. Table 1 gives the zero-order 351-nm diffraction efficiency of a NIF-sized CSG, which had its AR coating removed in places on the grating and on the back sides by being gently

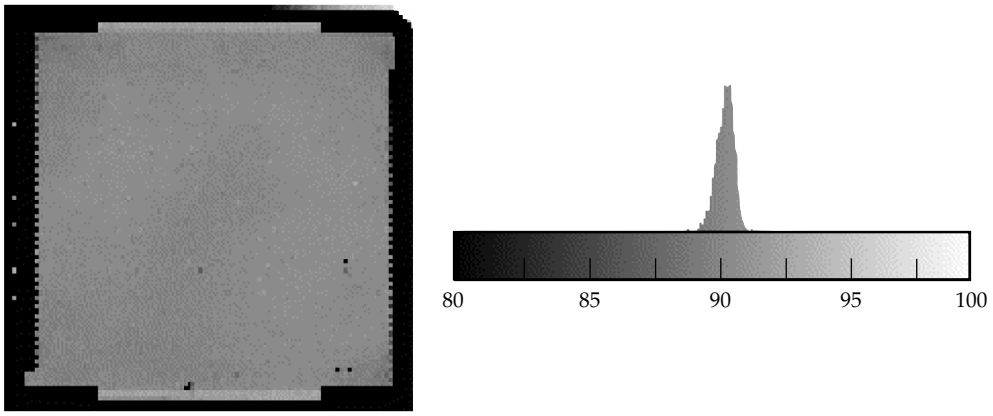

FIGURE 5. Zero-order transmission efficiency at 351 nm for a 41- by 39-cm color separation grating (#O2Z) at a 13° incidence angle. The mean efficiency is 90.5% with $\sigma = 0.75\%$. The zero-order transmission efficiencies at 1ω and 2ω were 0.26 and 0.05%, respectively. Both surfaces were uncoated. (70-00-0399-0769pb01)

wiped with a wet soft cloth. The highest efficiency is obtained with the AR coating removed only from the grating surface. When the AR coating is on the grating surface, the reduction in back reflection is more than compensated for by an increased efficiency for the higher transmitted orders. Thus, the zero-order transmission efficiency drops.

This drop in transmitted zero-order efficiency upon being AR coated results from a partial planarization of the etched structures, caused by surface tension effects as the coating is drying. Recall that the zero-order transmission at 351 nm is maximized when the etched structures are precisely deep enough to have integral wave multiples of phase retardation between adjacent elements. Planarization of the AR coating significantly alters this relation between adjacent steps. Figure 6 compares scanning electron micrographs (SEMs) of bare and AR-coated CSG steps of 1.4 and 0.7 μm (two-wave and one-wave steps). The ideal edge for a wet-etched CSG step is a quarter circle with a radius equal to the etched depth. The bare CSG steps that are shown closely approximate this ideal. The accumulation of colloidal sol-gel particles at the step edges (caused by capillary forces that pull liquid from adjacent areas while the coating is drying but still fluid) results in an increased film thickness many microns away from the edges. In the immediate vicinity of the steps, the coating is sufficiently thick to craze as it dries, due to shrinkage-related tensile stresses.

As a consequence of this effect, sol-gel AR-coated CSGs have significantly worse laser damage characteristics than when left uncoated. Modulation enhancement, due to increased energy in high transmitted orders, causes damage to downstream optics under conditions where minimal damage would normally be expected. Because of the extreme coarseness of the grating period with respect to the wavelength and the size of the beam, this modulation exists for

TABLE 1. Zero-order 351-nm diffraction efficiency of a NIF-sized CSG.

	Both sides bare	AR-coated back side	AR-coated both sides
Zero-order transmission at 351 nm (%)	90.8	93.5	89.6

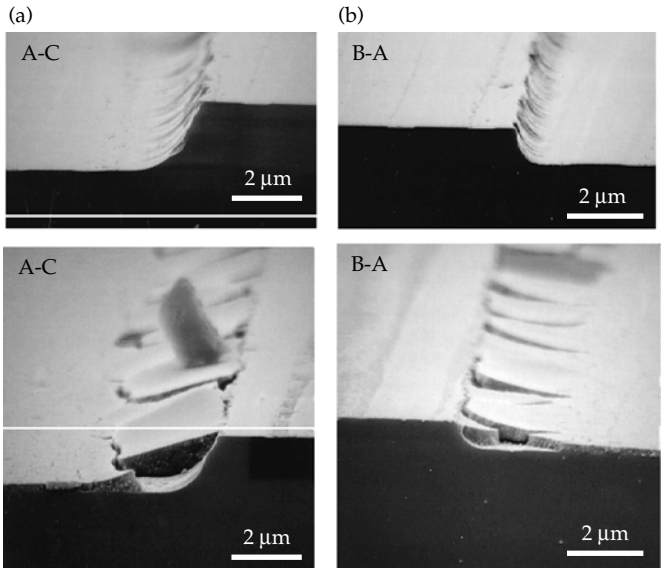

FIGURE 6. Scanning electron micrographs of (a) two-wave and (b) one-wave CSG steps wet etched into bare fused silica (upper) and into fused silica with a sol-gel AR dip coat (lower). (70-00-0399-0770pb01)

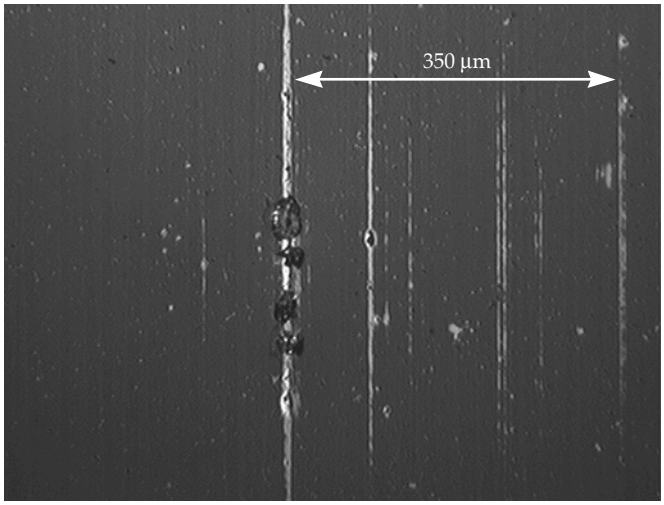

FIGURE 7. A micrograph of output-surface damage on fused silica, caused by modulation from an AR dip-coated color-separation-grating pattern on an input surface that was illuminated with 351 nm light at 18 J/cm^2 from a 1.1-mm rastered beam at 7.5 ns. (70-00-0399-0771pb01)

several meters downstream where the orders overlap. Figure 7 shows a SEM of output surface damage caused by the 351-nm, 7-ns irradiation of a NIF-sized, AR dip-coated optic with a CSG pattern on the input surface. The damage manifests itself as pinpoints that coalesce into lines that correlate with the grating period.

Calculations have been made, using surface profiles of bare and coated CSG steps (as measured by atomic-force and scanning-electron microscopy), to estimate the modulation that imperfect step edges and AR coatings cause. These calculations consider infinitely periodic structures with a resolution of about 0.2 µm, and so capture both the macroscopic effects of the grating and the contributions of single grating steps. However, they do not include the difference in refractive index between substrate and coating. Figure 8 shows the predicted peak-to-average intensity ratio as a function of distance downstream from the surface of various CSGs. A NIF-sized CSG with a period of 345 µm and dip-coated AR coatings is large enough so that maximum intensity modulations of about 2.5 are predicted for several tens of millimeters downstream from it. The bare grating itself exhibits a

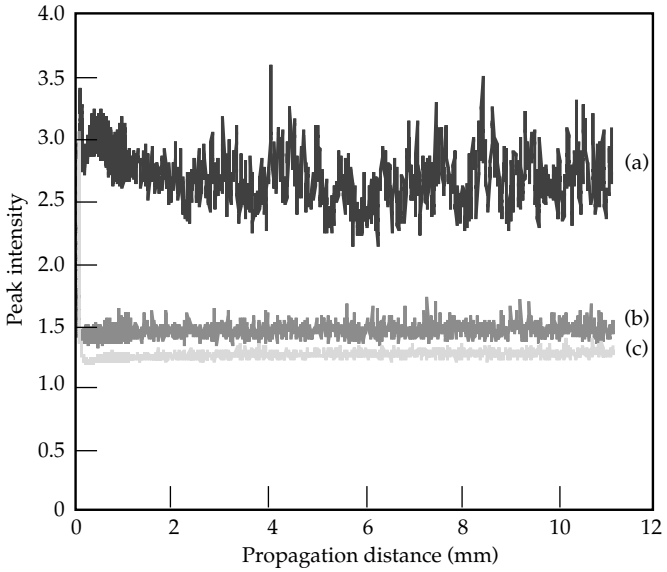

FIGURE 8. The calculated maximum peak-to-average intensity ratio, as a function of distance downstream from a wet-etched color separation grating (with and without a dip-coated AR layer). The calculations were done using measured profiles for the step edges and AR overcoat topography. The calculations did not take into account the refractive index difference between the coating and substrate. (a) = 345-μm grating period with an AR dip coat; (b) = 345-μm grating period, bare; (c) = 1100-μm grating period, bare. (70-00-0399-0772pb01)

modulation enhancement of about 1.5, entirely due to the nonvertical edges of the wet-etched steps. (The calculations assumed ideal etched depths. Errors in the depths of the etched steps are another source of intensity enhancement.) The modulation can be decreased by decreasing the density of the edges (that is, by increasing the period of the CSG). This model predicts that an uncoated CSG with an 1100-μm period will cause an intensity enhancement of about 1.3.

Color separation gratings with vertical edges and perfectly etched step depths would not contribute to intensity enhancement. Ion-beam etching can potentially create substantially vertical sidewalls; but, as this is written, ion-beam etchers that can maintain an etch-depth uniformity of 1% over a 40-cm square aperture on a thick fused-silica substrate are not a proven technology.

As previously stated, dip coating is the baseline process for applying AR coatings to NIF transmissive optics. However, other available coating technologies have been investigated. One, known as spin coating, is a standard coating process in the semiconductor industry using high centrifugation to apply uniform films onto wafer surfaces. It has applied AR coatings that are significantly more conformal (less planarizing) than dip coating on small (5-cm-diam) CSGs. However, spin-coated AR layers on large rectangular parts, relevant to NIF, have exhibited significant and highly variable planarization effects, which depend on the spin rate, orientation of the grating steps, and their position on the substrate. It has been concluded that sol-gel coatings deposited by either method on the CSG's surface are unsuitable for NIF because of the likelihood of damaging downstream optics. An AR coating applied by vacuum-deposition techniques would be largely conformal and would not contribute to downstream modulation; but such coatings that can survive the NIF's 3ω baseline fluence do not exist.

The design for the NIF CSG is evolving toward using the natural dispersion of the focus lens to eliminate 1ω and 2ω light from the target, for all but the central portion of the beam. Here, a subaperture, uncoated CSG with a maximum allowable period (about 1 mm) will divert the 1ω and 2ω light from the target. A schematic of this concept is shown in Figure 9. This design will minimize the area and density of etched steps and will therefore minimize the modulation. The grating period is maximized by using a "split" grating design with the grating's stairsteps facing away from the substrate's centerline, instead of facing in the same direction across the entire aperture. With this design, light of a particular wavelength does not have to cross from one side of the grating to the other at focus, so the deflection angle needed becomes less, and the period can therefore become larger.

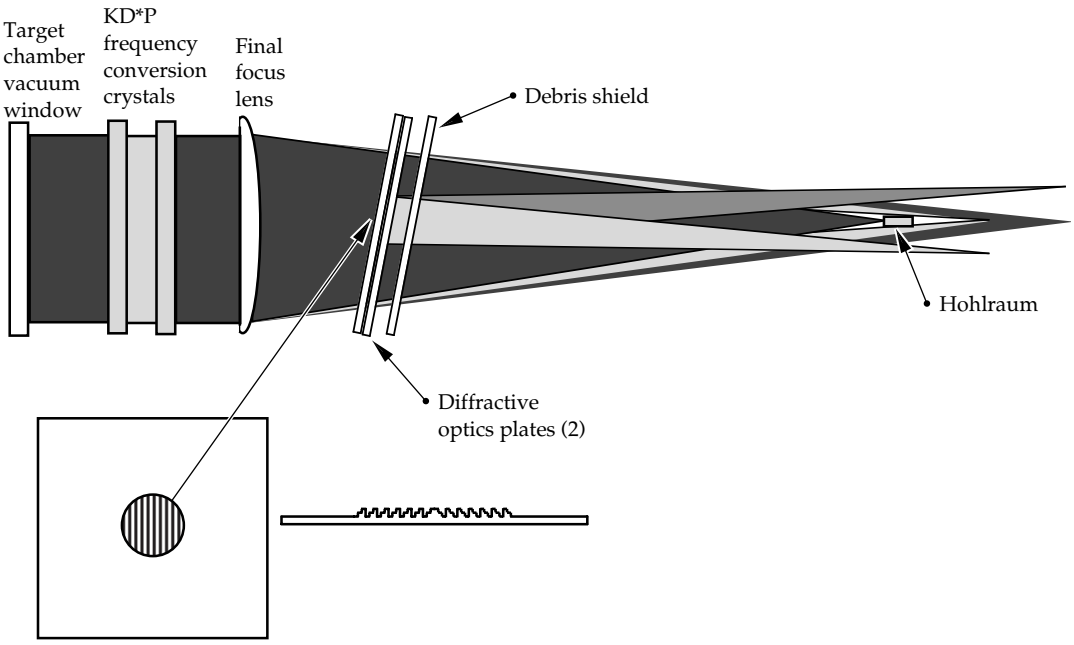

FIGURE 9. Schematic of a subaperture, split, color separation grating design that minimizes the area of the CSG and the etched step density. (70-00-0399-0773pb01)

Beam Sampling Gratings

The performance of a BSG is also influenced by AR coatings. The measured first-order diffraction efficiency of one NIF-scale BSG changed, from 0.4% bare to 0.15%, after a dip-coated AR layer was applied. The BSG structures are significantly shallower than the nominal 3ω AR-coating thickness of 72 nm. Calculations predict that transmitted first-order diffraction efficiency drops by more than a factor of three when the grating is covered with a completely planar AR overcoat. However, it does not change if the coating is completely conformal. These situations are illustrated in Figure 10. These data imply that AR dip coats on the BSGs are indeed largely planar.

The diffraction efficiency of a BSG drops about 40% when the same sol-gel layer is applied by spin coating at about 2000 rpm, suggesting an intermediate degree of planarization. In the case of BSGs, this planarization does not increase the likelihood of laser-induced damage, but the sensitivity of the diffraction efficiency to the coating's characteristics raises the possibility that environmental changes to the coating can cause unacceptable changes to the diffraction efficiency.

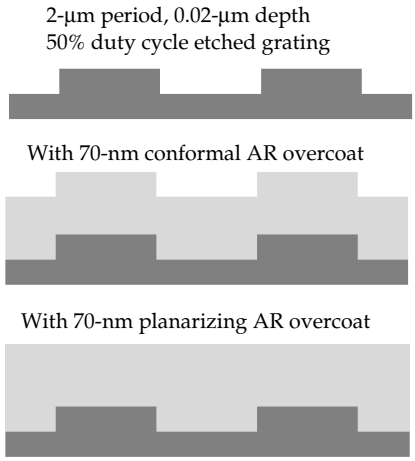

	CALCULATED EFFICIENCY @ 3ω (%)	
	–1 trans. order	Σ (reflections)
2-µm period, 0.02-µm depth 50% duty cycle etched grating	0.27	3.50
With 70-nm conformal AR overcoat	0.28	0.40
With 70-nm planarizing AR overcoat	0.08	0.20

FIGURE 10. Illustration of the calculated effect of sol-gel coating conformality on the first-order diffraction efficiency for a lamellar grating (representative of the NIF baseline design for the beam separation grating). At one extreme of conformality, there is no effect on the grating's efficiency, while at the other extreme (complete planarization) the efficiency is reduced by more than a factor of three. (70-00-0399-0774pb01)

Work is under way to characterize, both experimentally and via modeling, the sensitivity of the diffraction efficiency of AR-coated BSGs to environmental changes (such as those resulting from the presence of humidity and condensable organic contaminants).

Combining Diffractive Structures on One Surface

We have demonstrated the feasibility of combining the BSG and the CSG on the same surface[10] by the wet-etch process. The fine BSG structures are formed first on a featureless substrate, then the CSG is made. (Fabricating the CSG first and then adding the BSG is problematic. Planarization of the resist over the CSG's topography would result in resist film-thickness variations beyond the processing latitude of the holographic exposure technique used to write the BSG pattern.)

The processing steps for both elements of the combined structure are the same as described earlier. Figure 11 shows CSG features that have been profiled by white light interferometry and BSG features that were measured by atomic force microscopy. The measured optical performance of each diffractive structure is not affected by the presence of the other. The slight tapering of the BSG profiles as they are propagated into the bulk during the CSG step etching is predicted by isotropic etching models.[10,11] These model calculations show that the nominal NIF BSG profile can be wet-etched approximately four-μm deep before the grating ridges begin to lose height. Since the combined depth of a CSG/KPP is only 2.3 μm at most and the methods for fabricating the KPP and CSG are the same, it would be straightforward to fabricate all three NIF diffractive structures on the same surface. This is an enabling development, since it might become important to concentrate all diffractive structures onto one surface and leave it bare, in light of the problems that have arisen in finding a suitable AR coating.

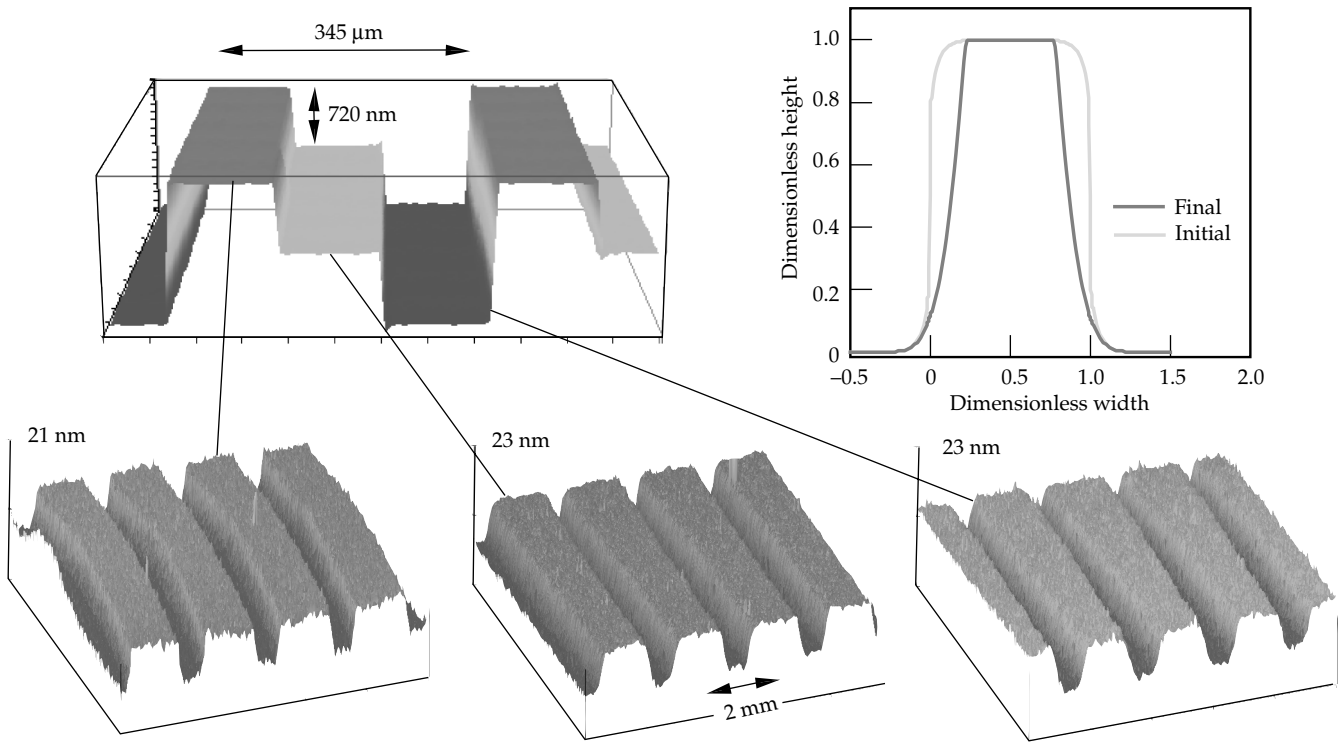

FIGURE 11. Beam sampling grating profiles measured by atomic force microscopy on different CSG steps, which are imaged by white light interferometry. Initial grating aspect ratio (height/width) ≈ 0.015. Upper-right corner shows model calculations for the initial and final BSG shape after etching to the depth of the deepest CSG structure. (70-00-0399-0775pb01)

Summary

We have fabricated demonstration diffractive optics required for the NIF's baseline design at full-scale via a wet-chemical etching of fused silica, using fabrication techniques and processing equipment suitable for large-scale production. We have examined the effect of AR sol-gel coatings on the performance and laser-damage resistance of diffractive optics, and have concluded that the color separation grating must be left bare or the grating must be stripped of its sol-gel coating to minimize modulation effects that will damage downstream optics. We have also demonstrated the feasibility of combining all NIF diffractive structures onto one surface.

Notes and References

1. J. A. Britten, R. D. Boyd, M. D. Perry, B. W. Shore and I. M. Thomas, "Low-Efficiency Gratings for Third-Harmonic Diagnostic Applications," 1st Int'l. Conf. on Solid State Lasers for Application to Inertial Confinement Fusion, M. Andre and H. T. Powell, eds., *Proc. SPIE* **2633**, 121–128 (1995).
2. S. N. Dixit et al., "Color Separation Gratings for Diverting the Unconverted Light Away from the NIF Target," 2nd Int'l. Conf. on Solid State Lasers for Application to Inertial Confinement Fusion, M. Andre, ed., *Proc. SPIE* **3047**, 463–470 (1996).
3. H. Dammann, *Appl. Opt*. **17**, 2273–2279 (1978).
4. M. W. Farn, M. B. Stern, W. B. Veldkamp, and S. S. Medeiros, *Optics Lett*. **18**, 1214–1216 (1993).
5. T. H. Bett et al., "Diffractive Optics Development for Application on High-Power Solid State Lasers," 1st Int'l. Conf. on Solid State Lasers for Application to Inertial Confinement Fusion, M. Andre and H. T. Powell, eds., *Proc. SPIE* **2633**, 129–140 (1995).
6. M. C. Rushford, S. N. Dixit, I. M. Thomas, A. M. Martin, and M. D. Perry, "Large-Aperture Kinoform Phase Plates in Fused Silica for Spatial Beam Smoothing on Nova and the Beamlet Lasers," 2nd Int'l. Conf. on Solid State Lasers for Application to Inertial Confine-ment Fusion, M. Andre, ed., *Proc. SPIE* **3047**, 282–292 (1996).
7. G. A. C. M. Spierings, *J. Mater. Sci*. **28** 6261–6273 (1993).
8. D. T. Liang and D. W. Readey, *J. Am Ceram. Soc*. **70**, 570–577 (1987).
9. I. M. Thomas, *Appl. Opt*. **25**, 1481–1483 (1986).
10. J. A. Britten and L. J. Summers, *Appl. Opt*. **37**, 7049–7054 (1998).
11. S. Lindau, *Opt. Acta* **29**, 1371–1381 (1982).

Producing KDP and DKDP Crystals for the NIF Laser

A. K. Burnham *R. A. Hawley-Fedder* *R. L. Combs*
H. F. Robey *M. Runkel* *R. C. Montesanti*
N. P. Zaitseva *M. Yan* *P. J. Wegner*
J. J. De Yoreo *M. Staggs* *L. J. Atherton*
S. A. Couture

The cost and physics requirements of the NIF have established two important roles for potassium dihydrogen phosphate (KDP) crystals.

1. To extract more laser energy per unit of flashlamp light and laser glass, the NIF has adopted a multipass architecture as shown in Figure 1. Light is injected in the transport spatial filter, first traverses the power amplifiers, and then is directed to main amplifiers, where it makes four passes before being redirected through the power amplifiers towards the target. To enable the multipass of the main amplifiers, a KDP-containing Pockels cell rotates the polarization of the beam to make it either transmit through or reflect off a polarizer held at Brewster's angle within the main laser cavity. If transmitted, the light reflects off a mirror and makes another pass through the cavity. If reflected, it proceeds through the power amplifier to the target.

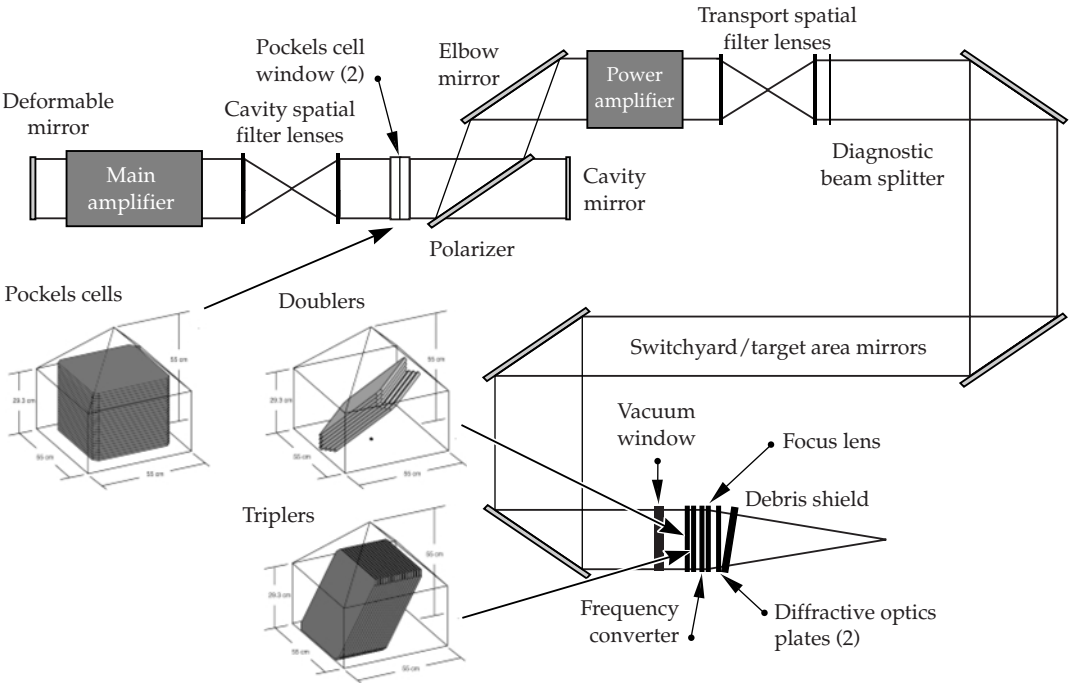

FIGURE 1. Schematic of the NIF laser showing the location of the KDP and DKDP components. Also shown is the orientation of the conversion crystals within the boules.
(40-00-0299-0434pb01)

2. Implosions for ICF work far better at shorter wavelengths due to less generation of hot electrons, which preheat the fuel and make it harder to compress. Compromising between optic lifetime and implosion efficiency, both Nova and the NIF operate at a tripled frequency of the 1053-nm fundamental frequency of a neodymium glass laser. This tripling is accomplished by two crystals, one made of KDP and one made of deuterated KDP (DKDP). The first one mixes two 1053-nm photons to make 526-nm light, and the second one combines a residual 1053-nm photon with a 526-nm photon to make 351-nm light.

The locations of the Pockels cell and frequency conversion crystals in the laser are also shown in Figure 1, along with the orientation of the plates as they are cut from the crystal boule. Although all finished crystals will be 41 cm square, their different orientation with respect to the crystal axes, required in order to accomplish their different functions, causes different boule size requirements for the three types of finished crystals. The Pockels cell crystal is the easiest, since it is cut horizontally with respect to the base of the crystal. As a result a 43-cm square boule is large enough, including a 1-cm buffer for finishing purposes, and the plates stack efficiently up to or even into the pyramidal cap, depending on the size of the base. Only about 15 of these small boules are needed. The KDP doubler crystal is the most challenging, as it is rotated in two axes with respect to the base. As a result, the minimum size base for a single doubler crystal is 51 cm, and a symmetric 55-cm-square by 55-cm-high boule will generate only six doublers, so nearly 35 of these boules will be required. A symmetric DKDP tripler must be a minimum of 55 cm high to be tall enough for a single tripler, but that minimum size will yield about 15 triplers.

Boules of both KDP and DKDP meeting NIF size and quality requirements have been grown by Cleveland Crystals, Inc. (CCI), by what is often called conventional growth. In this case, impurities in the growth solution poison growth of the vertical faces (prisms), thereby maintaining a cross section approximately equal to that of the original seed crystal as the pyramid faces grow. Unfortunately, this pyramidal growth is very slow, and it takes about two years to grow a crystal to NIF size. To provide more programmatic flexibility and reduce costs in the long run, we have developed an alternative technology commonly called rapid growth. Through a combination of higher temperatures and higher supersaturation of the growth solution, a NIF-size boule can be grown in 1 to 2 months from a small "point" seed. However, growing boules of adequate size is not sufficient. Care must be taken to prevent inclusions of growth solution and incorporation of atomically substituted impurities in the prism growth. Other issues important for meeting transmitted wavefront quality, absorption, and laser damage criteria must be addressed also.

During the past year, we made substantial progress towards bringing the rapid growth technology to the stage needed to supply most of the KDP and some of the DKDP needed for the NIF. This article reviews the technical hurdles that were overcome during this period and outlines some of the issues yet to be fully resolved. It also covers some of the efforts to transfer this technology to two potential vendors for NIF crystals—CCI and Inrad—as well as the development of crystal finishing technology.

Crystal Growth

For several years, the rapid growth process has reproducibly grown crystals of high visual quality up to about 20 cm in linear dimensions in tanks containing less than 100 L of solution. These systems demonstrated many of the important conditions needed to grow crystals of NIF quality, such as solution purity and ways to achieve adequate mass transfer at the growing crystal surface. Over the past year, this understanding has been applied at the 1000-L tank scale in order to improve yields of NIF-size boules to the point where rapid growth can become an industrial production process. This section reviews the fundamentals of the growth process and the particular problems that affect the commercial viability of rapid growth for NIF-scale boules.

UCRL-LR-105821-99-2

The fundamental property of nature enabling rapid crystal growth is that KDP can attain very large and stable supersaturations in solution. In other words, KDP will not spontaneously crystallize from solution when a solution is prepared at high temperature and then cooled so that the salt concentration is above its equilibrium solubility. This is because any protocrystal formed by a statistical fluctuation has to reach a minimum size before growth is thermodynamically favorable. (This same nucleation criterion occurs in many aspects of chemistry and physics.) Measurements have shown that stable supersaturations from 35% at 65°C to 100% at 10°C can be attained if the solution is thoroughly preheated to eliminate any nucleation sites, and stability is not affected by impurities at the level of tens to hundreds of parts per million.[1] This supersaturation is much higher than the 3–20% required for growing crystal faces at rates of 10–20 mm/day.

When a seed crystal is introduced into this supersaturated solution, the crystal immediately grows at a rate that depends on a variety of chemical kinetic and mass transfer factors. Practical experience over many years has shown that the best way to start this process is to first partially dissolve an oriented seed crystal of about 1 cm^3 in size above the saturation temperature, then decrease the temperature until the solution supersaturation reaches about 3%, at which time the seed "regenerates."[2] Regeneration is a process in which a rectangular base and pyramid form over the partially dissolved, rounded seed crystal. A picture of a regenerated seed is shown in Figure 2. It is important to accomplish this regeneration rapidly (over 1–3 hours) so that each crystal face will have numerous imperfections called dislocations. The crystal grows by adding atoms from solution to a set of atomic steps that emanate from these dislocations. This configuration is called a growth hillock, and a microscopic picture of a growth hillock is shown in Figure 3.[3] As growth proceeds, the stronger growth hillocks crowd out the weaker ones, and favorable growth proceeds with one to four hillocks on each crystal face. Crystals continue to grow as long as the temperature is decreased to maintain appropriate supersaturations. The growing crystal is rotated back and forth on a horizontal platform with a washing machine-like action to maintain good mass transfer.

Even though the growth solution is stable with respect to homogeneous nucleation, occasional heterogeneous formation of a single unwanted seed at a variety of possible locations can cause the formation of unwanted crystals, which are generally first observed on the bottom of the tank. This crystal, being grown in nonoptimal conditions, usually cracks and subdivides, thereby seeding other parts of the tank. When one of these seeds inevitably lands on the product crystal, its quality will be spoiled and the run ruined. Eliminating these spurious crystals for the entire two months of a growth run continues to be one of the most important challenges for cost-effective production.

Impurities in solution are detrimental for a variety of reasons:

- They affect the growth rates of the prism faces.
- They can enhance the formation of inclusions of growth solution that reduce optical quality.
- They substitute into the atomic lattice in the prism sectors and cause inhomogeneities in the refractive index and loss of optical transmission by absorption.

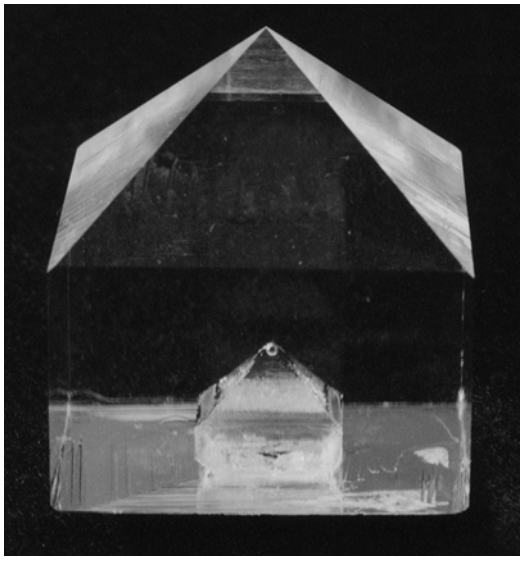

FIGURE 2. Photograph of a recently regenerated seed. The cloudy regeneration layer is covered with about 1 cm of clear growth.
(40-00-0299-0435pb01)

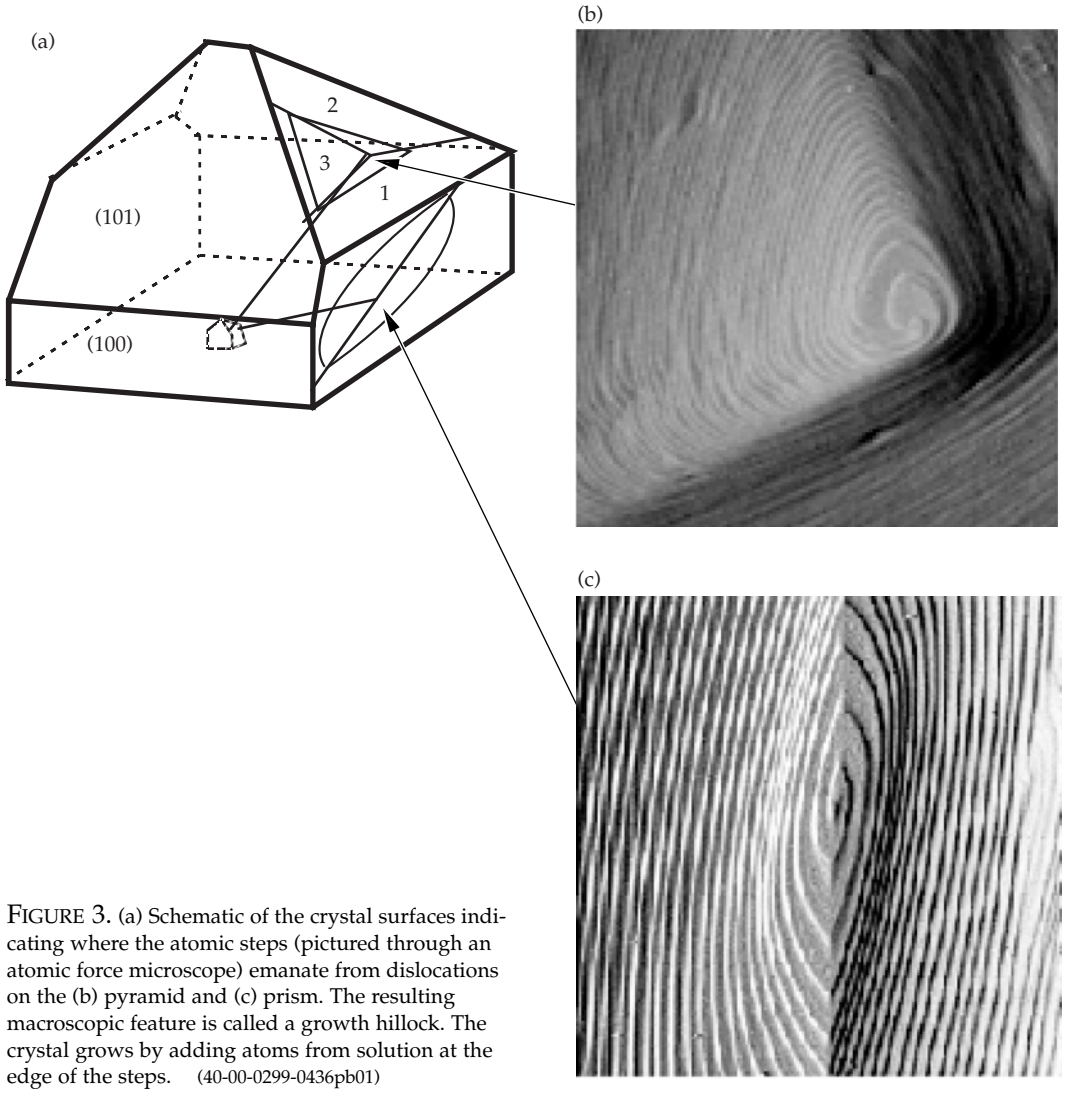

FIGURE 3. (a) Schematic of the crystal surfaces indicating where the atomic steps (pictured through an atomic force microscope) emanate from dislocations on the (b) pyramid and (c) prism. The resulting macroscopic feature is called a growth hillock. The crystal grows by adding atoms from solution at the edge of the steps. (40-00-0299-0436pb01)

- They may form particulates that affect the laser damage threshold of the material.

While the chemical structure of the pyramid face causes typical ionic impurities to be rejected from the growing crystal, the chemical structure of the prism face causes them to be selectively absorbed and incorporated into the crystal.[4] A few examples of this selective absorption and rejection are shown in Table 1. Fe is the most important impurity in terms of transmittance, because $FePO_4$ is highly absorbing at 351 nm, resulting in a maximum acceptable Fe concentration of 200 ppb for salt from which DKDP triplers are to be grown.

TABLE 1. Concentrations of typical impurities in the raw material and in the pyramidal and prismatic sectors of KDP crystals.

Impurity	Raw material*	Pyramid*	Prism*
B	1000	ND	ND
Na	86,000	ND	ND
Al	900	200	4400
Si	12,000	<100	390
Ca	3600	ND	ND
Cr	2000	490	11,000
Fe	5300	110	12,000

*Units of ng/g KDP
ND = not detected

Impurity incorporation into the prism face also affects the relationship between growth rate and supersaturation, as shown in Figure 4.[5] At low supersaturations, impurities effectively stop prism growth, and this condition is called "the dead zone." Conventional growth occurs in this region, and only pure pyramid material is formed. Unfortunately, this corresponds to growth rates less than 1 mm/day, which results in growth times greater than one year for NIF-size boules. In the middle transition zone, relatively small changes in growth conditions can have a drastic effect on growth rate. As is typical for any stable, reliable industrial process, this region should be avoided. This leaves the high-growth region as the most appropriate for development.

While the effect of impurities on growth rates is understood quantitatively over some range of conditions, it is not understood quantitatively for mixtures of impurities and over the wider temperature range used to grow crystals. Rather than attempt to quantify this parameter space in detail, our approach was instead to reduce impurities to the lowest practical level, which is also important for meeting other specifications, and use the qualitative principle of maintaining the highest possible growth rate to minimize the effect of impurities on growth instability. Once the necessary purity of the starting salt was attained (<0.5 ppm impurities), the contribution of impurities from the Pyrex growth tanks was explored. Though usually inert, there is a finite rate of tank dissolution in the hot KDP solutions used for rapid growth.[4] Using measured Pyrex dissolution rates and the uptake coefficients for various impurities in the prism sector, we have successfully modeled the buildup and eventual consumption of Al and Fe in the growth solution,[6] as shown for Al in Figure 5. Elements such as B and Si are not absorbed in the crystal and continue to build up in the growth solution, while others such as Ca are roughly constant during each growth run but increase after each resaturation of the growth solution. Plastic tanks are being considered to eliminate this problem. Another important recent advance for maintaining crystal quality is the successful implementation of constant filtration to remove particulates that come from moving equipment or precipitation.[7]

At high growth rates, another problem becomes important. Variations in KDP concentration on the μm scale at the growing crystal steps can cause inclusions of growth solution. These inclusions can easily be large enough to cause more obscuration by scattering than can be tolerated in the laser. Figure 6 summarizes much historical data on the occurrence of pyramidal

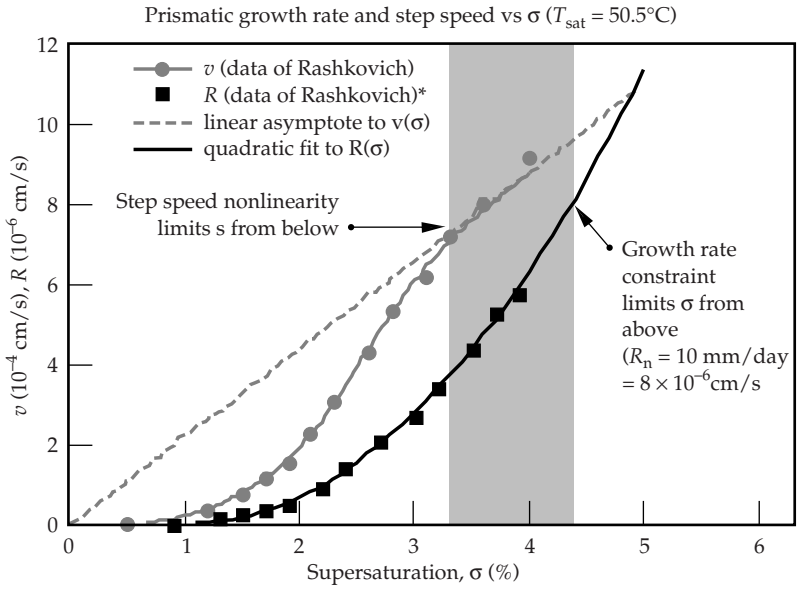

FIGURE 4. Effect of impurities on the step velocity and normal growth rate of KDP. The optimal growth rate is above the nonlinear region of step velocity and an upper bound determined by the uniformity of mass transfer. (40-00-0299-0437pb01)

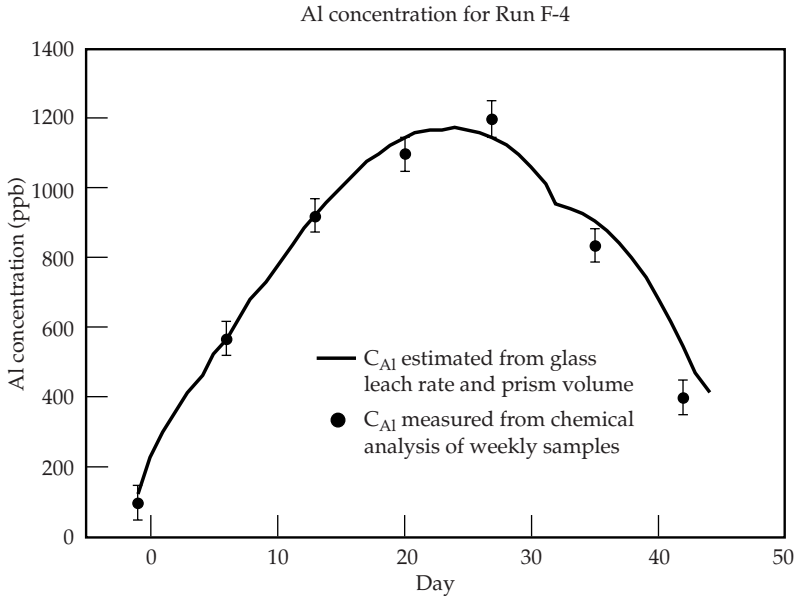

FIGURE 5. Comparison of measured and calculated Al concentration in the growth solution as a function of time. The Al concentration initially rises because the rate of glass tank dissolution dominates when the crystal is small; it later falls because the rate of uptake in the prism face increases with crystal size and exceeds the glass dissolution rate, which drops with temperature.
(40-00-0299-0438pb01)

inclusions in 1000-L growth tanks through 1998, indicating that for low rotation rates pyramidal inclusions are much more prevalent at high growth rates. The same trend occurs for prismatic inclusions. This presents the crystal grower with a dilemma—how to avoid the detrimental effects of impurity buildup and associated degradation of prismatic KDP that occurs at slow growth rates while avoiding the potential formation of massive pyramidal inclusions at high growth rates.

Microscopic investigations, hydrodynamic modeling, and theoretical modeling have been combined to provide a good mechanistic understanding of the

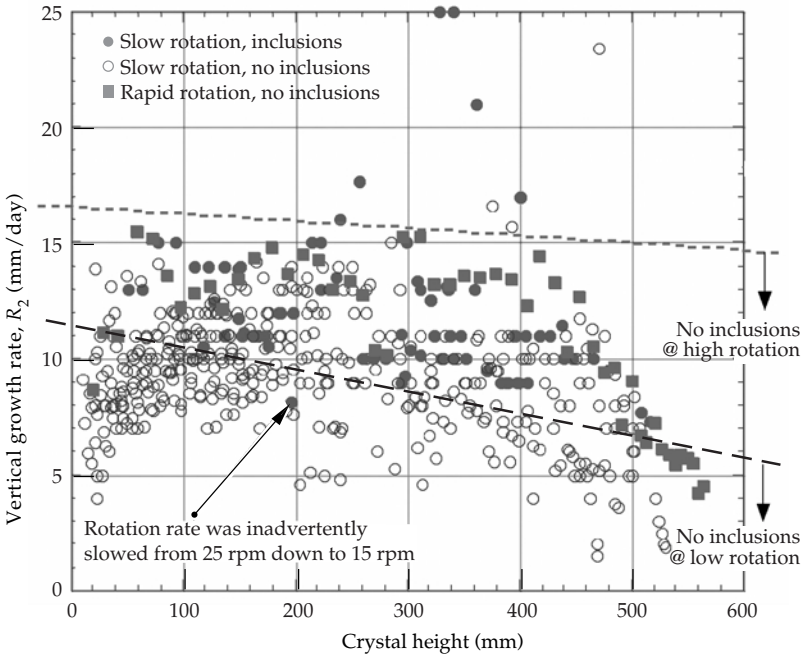

FIGURE 6. Summary of 1000-L growth tank data showing the relationship between pyramidal inclusions and growth rates for slow and fast rotational regimes. For runs prior to late 1998, the rotational rate was typically 25 rpm, while the high rotation rate during the recent run represented by the filled squares was at 50 rpm.
(40-00-0299-0439pb01)

formation of inclusions. A micrograph of one type of unstable growth is shown in Figure 7, in which "fingering" is apparent on the advancing growth step.[8] Although thermodynamics promote the filling of cavities between the fingers during slow growth, kinetics can cause the fingers to grow catastrophically, thereby surrounding and occluding growth solution. Solution moving in the opposite direction of the step advance is depleted in concentration as it moves past the tips of the fingers and towards the cavities, thereby causing a faster growth rate at the tip of the finger than at the base. Rapidly alternating the direction of flow helps prevent this catastrophic growth. A second type of instability involves the bunching and bending of elementary growth steps into macrosteps due to inadequate stirring.[9] When macrosteps from two sides of a growth hillock bend around and approach each other from the opposite direction, a deep valley can be formed. Inclusions also tend to form in the vicinity of this valley. Valley formation can be minimized by rapid rotation, thereby keeping the solution concentration in the center of the crystal face closer in magnitude to that along the edges.

Through a combination of these fundamental studies and growth experiments at various scales over the past year, we have shown that better mass transfer by increased acceleration and rotation rates can increase the inclusion-free growth rate by 20 to 40% over the slow rotation limit shown in Figure 6. The best-quality NIF-size KDP boule grown to the time of this writing, completed in late 1998, followed the solid-square growth trajectory also shown in Figure 6, substantially above that previously considered safe. An important aspect of achieving these higher rotation rates was the design and fabrication of streamlined Al growth platforms coated with a nonleaching Teflon-like coating.

The shape of the product crystal is also a practical problem. When grown rapidly from a pure solution intended to meet quality objectives, DKDP especially tends to grow with a height-to-width (aspect) ratio as low as 0.7. Since our circular growth platforms have a diameter of 90 cm, the maximum symmetric-base is 63 cm, which would produce a crystal only 44 cm high—too short for triplers. A similar though less severe problem occurs for KDP. Improving aspect ratio by allowing more solution impurities to retard prism growth is undesirable, especially for DKDP, which is challenged to meet a more difficult 351-nm laser damage threshold. As a result, we are exploring a variety of ways to improve doubler and tripler yields by making more optimal shapes. One idea is using an off-center seed to promote asymmetric growth of the type shown in Figure 8a, which is appropriate for increased doubler yield. A method for triplers is to grow the DKDP boule horizontally, which increases aspect ratio (now rotated) by eliminating one growth prism and adding a second pyramid. Again very recently, a good-quality horizontal DKDP boule, shown in Figure 8b, was grown for the first time to NIF size. Successful shape control could increase conversion crystal yields by a factor of two over that from symmetric, vertically grown boules.

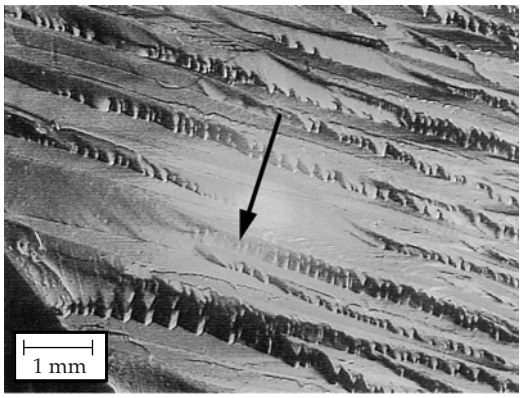

FIGURE 7. Fingering growth of macrosteps on the KDP surface. (40-00-0299-0440pb01)

Laser Damage

At high laser fluences, KDP and DKDP damages in the bulk by forming pinpoint scattering sites a few micrometers in size.[10] The basic consideration driving the laser damage specification is that this scattering should not exceed 0.1% of the laser light per optic traversed at the fluences expected for a 1.8-MJ ignition shot. The relevant fluences are an average of 12 J/cm^2 and 3σ limit of 18 J/cm^2 for 1053-nm light over 3 ns on the KDP doubler and an average of 8.7 J/cm^2 and 3σ limit of 14.3 J/cm^2 for 351-nm light

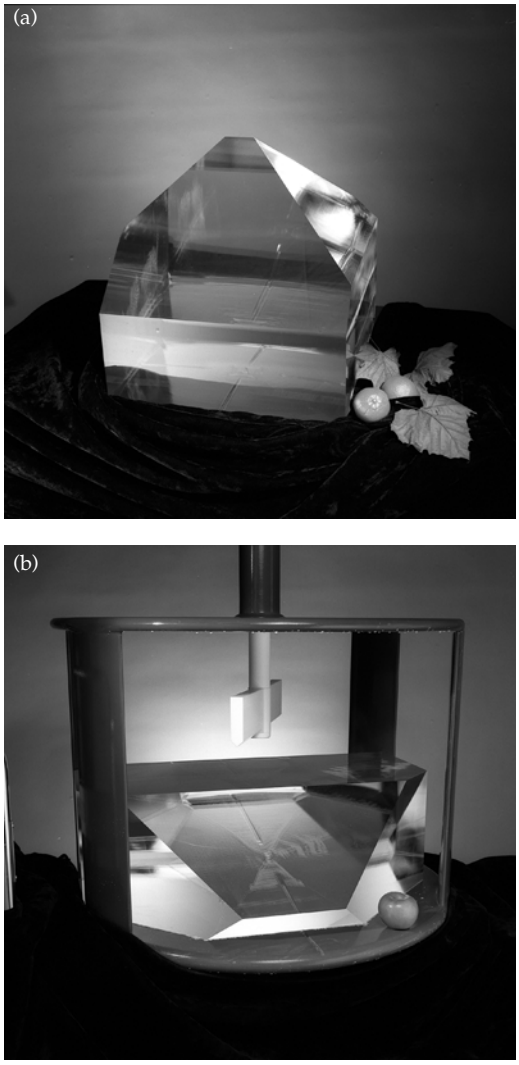

FIGURE 8. Recent rapid-growth NIF-size boules. The top boule will yield about 11 KDP doublers, and the bottom boule will yield about 12 DKDP triplers. (40-00-0299-0441pb01)

over 3 ns on the DKDP tripler. The allowable damage is equivalent to about 100 pinpoints/mm^3 of crystal volume.

In practice, the allowable damage criterion is more complicated. First, the extent of damage occurring at any given fluence depends on the previous laser exposure of the optic: low-fluence shots tend to condition both KDP and DKDP, resulting in less damage at higher fluences than if the material were initially exposed to the high fluences. Second, since much of the damage occurs in areas of the beam with above-average fluences, the accumulated damage over time depends on how much and how fast the areal fluence distribution changes in the NIF beam over many shots. In addition, the amount of damage occurring in KDP can be reduced by thermally annealing the material.

We made progress during the past year in understanding both the relationship of easily measured, laser-damage distribution curves and how to condition the crystals to minimize damage on-line. Through a combination of constant filtration during growth and thermal annealing of the plates at 160°C over several days, damage of KDP at 1053 nm is not a serious issue. On the other hand, the damage characteristics of DKDP at 351 nm are more variable for unknown reasons, and much of the material formed under the best conditions as currently understood and preconditioned by low-fluence shots is only marginal at NIF fluences.

To understand laser damage studies, one must first understand the nomenclature and characteristics of the standard tests:

- 1/1 a single laser shot of specified fluence
- S/1 a set of shots (typically >100) of specified fluence
- N/1 a small sequence of shots from low to high fluence
- R/1 a ramp of many shots (typically >100) from low to high fluence

In addition, the damage characteristics of any material varies from location to location, so results are ordinarily presented in terms of the distribution of fluences at which a specified amount of damage occurs over many 1-mm beam spots, typically 100.

Figure 9 shows a comparison of the S/1 and R/1 damage distributions curves for KDP sample 214, both as grown and after thermal annealing. Note that the R/1 damage curve occurs at higher fluence than the corresponding S/1 curve, indicating the beneficial effect of the laser conditioning inherent in an R/1 experiment. Also note that both the S/1 and R/1 curves shift to higher fluence upon thermal annealing. These results are typical of all KDP samples grown with constant filtration, indicating that thermally annealed KDP normally damages at fluences above that required for the NIF, especially if the laser energy is increased to NIF fluences over several shots. The acceptability of the R/1 threshold is unambiguous, since essentially no damage occurs for the maximum expected NIF fluence, but further clarification is needed for the S/1 case. Even 10%

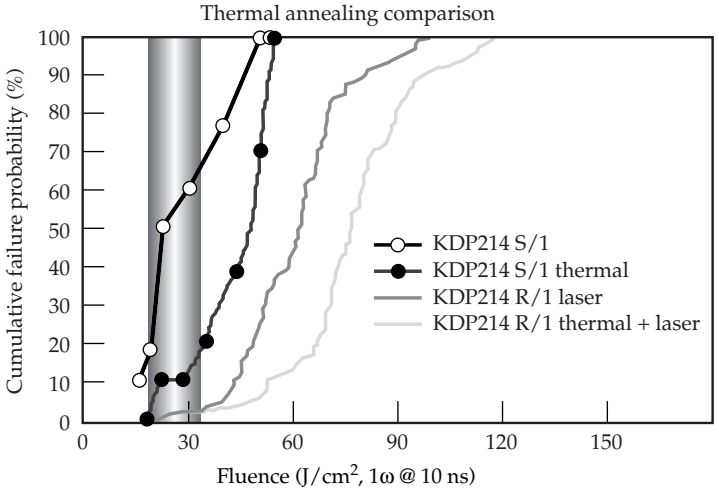

FIGURE 9. Percent of 1-mm aperture beam exposures having detectable damage for a rapidly grown KDP sample exposed to various preconditioning and fluence schedules. The band represents the 4σ fluence distribution on the NIF adjusted for pulse length. (40-00-0299-0442pb01)

failure probability on this scale for the average NIF fluence is not a problem because damage is detected at a level in which most of the light is still transmitted and the damage pinpoints do not grow.

The situation for damage of DKDP at 351 nm is less certain because of fewer data, the greater variability of DKDP properties, and the overall proximity to the damage requirement. Furthermore, enhancement of the damage threshold by thermal annealing is not practical because either decomposition or recrystallization occurs at temperatures required for annealing. A summary of all R/1 data to date for both conventional- and rapid-growth DKDP are shown in Figure 10. Note that the best conventional-growth DKDP has a damage distribution far greater than NIF requirement, indicating that the desired material can be grown. However, the

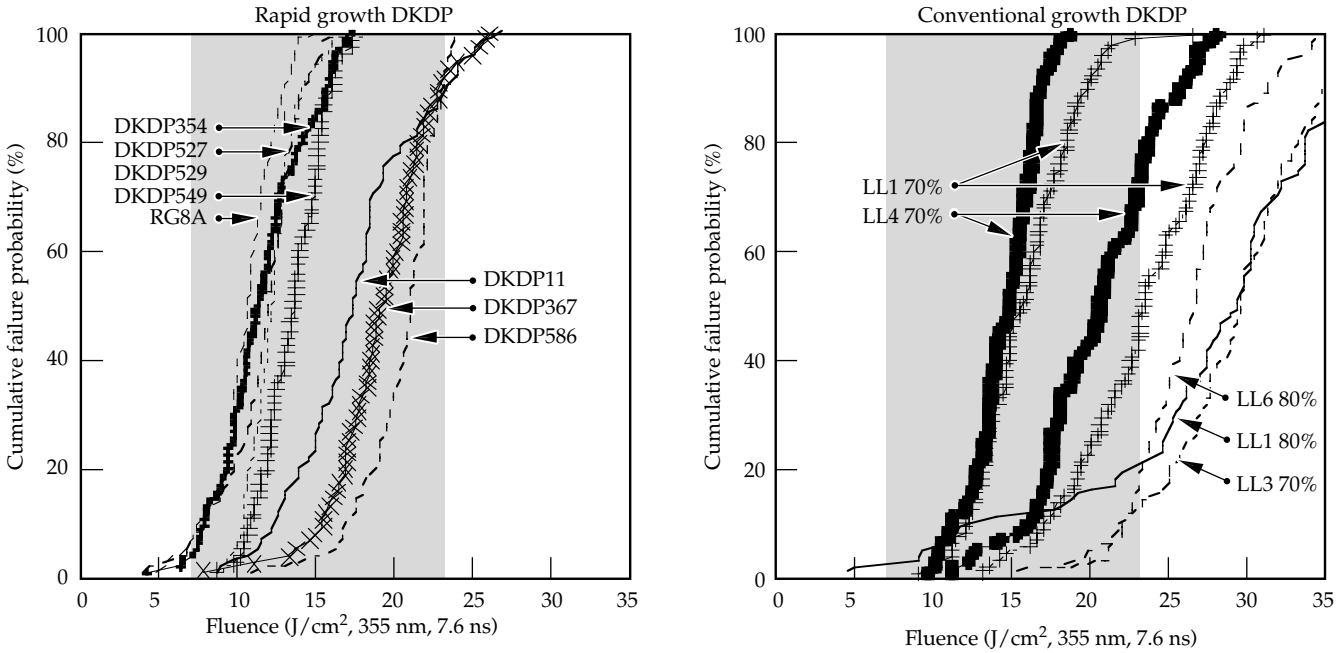

FIGURE 10. Summary of all 3ω damage data for rapidly and conventionally grown DKDP. To compare to NIF requirements, these fluences are scaled to a 3-ns pulse length by dividing by $(7.6/3)^{0.5} = 1.6$. (40-00-0299-0443pb01)

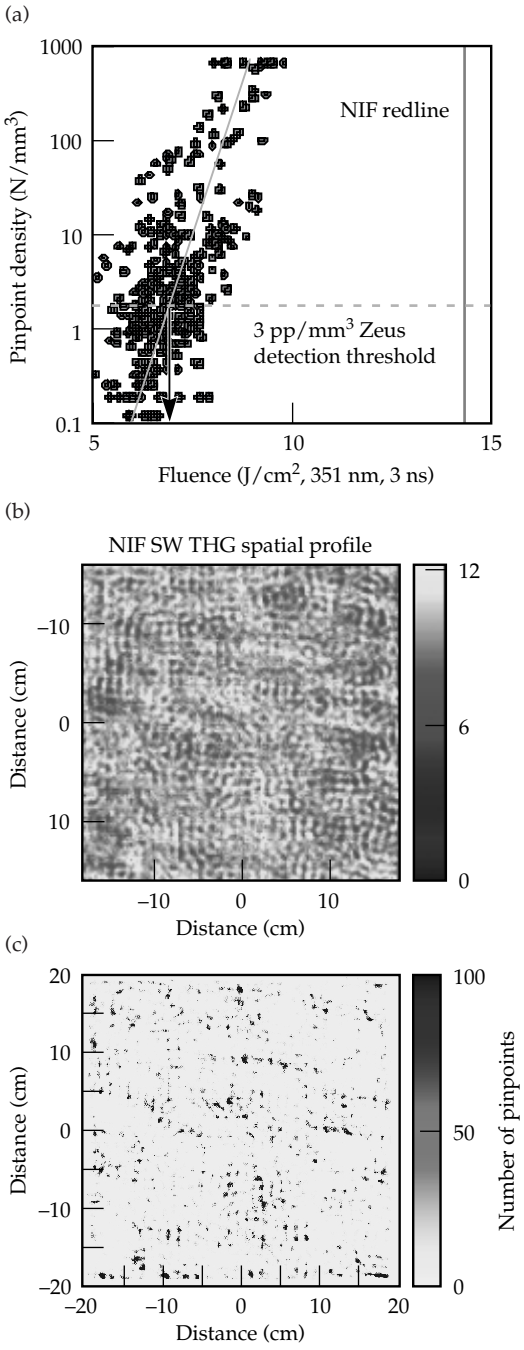

FIGURE 11. Relationships among laser fluence, pinpoint bulk damage, and obscuration at NIF fluences. (40-00-0299-0444pb01)

damage threshold is quite variable for reasons not yet completely understood (discussed below), so highly efficient production is not yet in hand.

Because of the proximity of the damage distribution curve of many samples to the NIF fluence distribution, a closer evaluation is appropriate. Sample DKDP11, one of the best by rapid growth, was exposed to a 1-cm-diam, 3-ns, 351-nm beam with the Optical Science Laser (OSL). Pinpoint density and obscured area for a 1-cm-thick crystal is given in Figure 10 as a function of fluence for an N/1 ramp of 8 shots. When this pinpoint density is convolved with the expected NIF beam fluence profile as shown in Figure 11, 0.3% obscuration is predicted by the time the laser reaches a 1.8-MJ shot. This is close to the desired goal, so the R/1 damage distribution of this sample represents a possible lower acceptable limit.

Crystal RG8A-1 was used to generate 351-nm light on one of the Beamlet experimental campaigns. The crystal was ramped over 9 shots to a maximum fluence of 3.8 J/cm^2 over 1.5 ns, which corresponds to ~5.5 J/cm^2 in 3 ns and 8.6 J/cm^2 in 7.6 ns assuming a $\tau^{0.5}$ scaling law. Essentially no bulk damage was observed, which is consistent with being at the very beginning of damage for the R/1 curve. An estimate of the pinpoint density vs fluence distribution, convoluted with the measured beam profile on Beamlet, leads to a prediction of about 0.1% obscuration loss. However, the average NIF full fluence corresponds approximately to the 80–100% damage level, so RG8A material is not expected to meet the damage requirements of NIF for full-fluence shots. Consequently, the ability to grow NIF-size DKDP boules of sufficient quality by rapid growth is yet to be demonstrated. However, it is encouraging that several samples of sufficient quality have been grown in 20-L tanks.

While conversion crystals initially installed onto the NIF may see a gradual increase in fluence, and thereby achieve laser conditioning on line, subsequent replacements will not have that opportunity. Moreover, uncertain performance during initial start-up provides some risk to the initial conversion crystals. Consequently, it is highly desirable to provide laser conditioning of the conversion crystals by raster scanning prior to installation. Figure 12 shows the improvement of the S/1 damage fluence distribution with one and two raster preconditioning steps. (The two steps are required because attempts to raster-condition crystals in a single scan

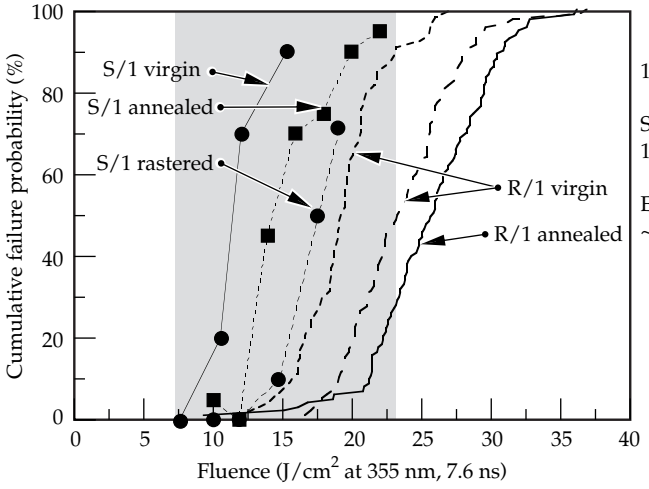

FIGURE 12. Raster conditioning increases 3ω damage performance of KDP. Two successive raster scans at 10 and 14 J/cm^2 increase the S/1 performance to near the R/1 level. (40-00-0299-0445pb01)

is hampered by jitter of the raster beam, which causes too large of fluence jumps.) The two-step preconditioning raises the S/1 damage distribution to near that of the R/1 curve, demonstrating that off-line conditioning can be an effective way to bring new optics on line.

Considerable effort has been invested in discovering the precise mechanism of bulk laser damage so that the damage threshold can be improved. Recall that the NIF fluence is constrained by damage to the crystals. First, a comparison of preexisting laser scattering sites with subsequent laser damage locations reveals no correlation between scattering and damage at either 1053 or 355 nm, presumably because the scattering sites have negligible absorption.[11] Similarly, bulk absorption is not related to damage; the 355-nm damage distributions for prism and pyramid material are the same even though the content of dissolved iron and resulting absorption coefficient are substantially different.[12] Simple thermal calculations show that even a few percent of laser absorption evenly distributed throughout the material should not be a problem, but localized heating from highly absorbing particles in the range of 10–100 nm can easily cause thermal and acoustic shock damage to surrounding material. $FePO_4$ has the required absorption coefficient at 3ω, and addition of $FePO_4$ powder to the growth solution causes a major drop in the 3ω damage curve. In addition, secondary ion mass spectrometric (SIMS) analysis of the material sputtered from three damage sites showed significant amounts of Fe and Cr in addition to major amounts of Ca. Perhaps the Ca buildup from repeated resaturations causes the formation of mixed cation phosphate precipitates. Further work is in progress to test this hypothesis.

Finishing Development

Producing finished crystal optics with an aspect ratio of greater than 40:1 from large boules poses a variety of fabrication challenges. Many of the primary specifications for NIF crystals are difficult to meet. Three of the more difficult specifications are related to crystal surface figure and finish and include: short wavelength surface roughness (3.0 nm rms for λ_{sp} <0.12 mm), surface waviness (6.4 nm rms and power spectral density for λ_{sp} between 0.12 mm and 33 mm), and 5λ ($\bar{\lambda}$ = 633 nm) peak-to-valley surface figure for λ_{sp} >33 mm. Perhaps the most difficult specification is producing finished crystals oriented with respect to the crystallographic axes such that the average phase matching angle for frequency conversion is accurate to ±15 µrad (external angle) for doublers and ± 30 µrad for triplers. Since the phase matching angle is strongly dependent upon use temperature and wavelength, extremely precise finishing machines and metrology tools are required for process control during crystal fabrication. In addition to difficult technical specifications, aggressive cost and

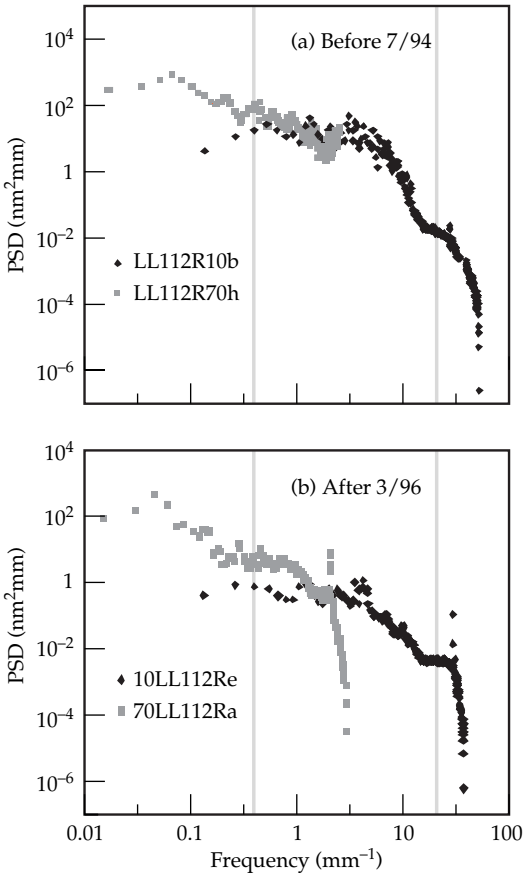

FIGURE 13. Comparison of power spectral density (PSD) for the surface roughness of Beamlet crystals machined on the Pneumo machine at CCI in 1994 and 1996, showing an improvement from 3- to 8-nm roughness to 1- to 2-nm roughness.
(40-00-0299-0446pb01)

production schedules necessitated the development of improved manufacturing process and tools.

Early development activities focused on determining the requirements for long-lead machine tools. The Pneumo Final Finishing Machine at CCI was improved in 1995–96, as illustrated in Figure 13. The inspection data from subsequent parts was used in laser propagation modeling, which validated that diamond-turned parts could meet NIF requirements and established the new finishing machine requirements. However, the Pneumo machine is 20 years old, undersized, and cannot finish parts in the time required. Consequently, a new machine was designed and fabricated by the Moore Tool Company. The resulting machine, shown in Figure 14, is currently undergoing performance acceptance test at LLNL.

While roughness, waviness, and wedge are controlled by the final finishing machine, optical figure is largely determined by the blank fabrication process. Again, current development activities can be traced back several years. The Nova fabrication and finishing process could not reliably produce finished crystals meeting NIF figure requirements. As a result, CCI modified its proprietary blank fabrication process in 1995 during Beamlet crystal production, and the new process has been used to produce many large-aperture crystals that meet NIF figure requirements. As shown in Table 2, the process of producing flat blanks is now well in hand. Again, however, the CCI machines are old, undersized, and too slow to meet NIF production schedules.

FIGURE 14. The Moore Final Finishing Machine has now been assembled and is undergoing acceptance testing.
(40-00-0299-0447pb01)

TABLE 2. A summary of crystals produced for Beamlet since 1996 shows that the flatness process can meet NIF specifications at high yield.

Crystal	Surface figure (waves @ λ = 633 nm)
328-4	8
328-5	5
328-6	4
RG8B-1	2.2
RG8B-2	2.3
RG9B	2.1
345-1	4.5
70% LL37-1	1.1
LL6-11	4.5

Consequently, Lawrence Livermore National Laboratory (LLNL) started developing a new set of custom machine tools in 1997: a boule-facing machine, a profiling mill, and three flatness machines. The flatness machine is the most challenging of the three types. It must produce surfaces that meet the flatness requirements for λ_{sp} >33 mm. A model of it is shown in Figure 15, and the first machine is nearing dry-cut testing. Three z-axis slides provide approximately 100 mm of vertical travel and up to 0.25 degrees of tip and tilt. Compliance tests performed on the z-axis last summer determined the stiffness of the z-axis—an important metric on precision machine tools—to be 36 nm/N (6.5 μin./lb). This is actually slightly better than the existing Pneumo machine and leaves open the possibility that the basic machine design may be good enough to allow one of the flatness machines, with modest upgrading to remove roughness and waviness at scale lengths <33 mm, to serve as a backup final finishing machine.

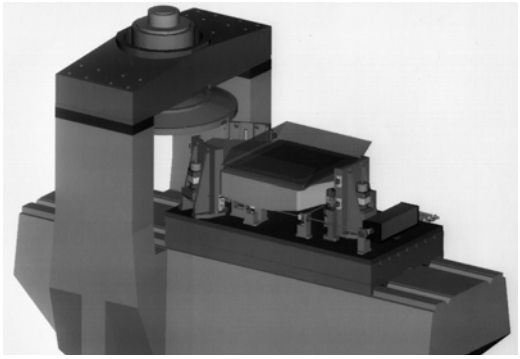

FIGURE 15. The LLNL Prototype Flatness Machine design is highly integrated to reduce complexity during machine assembly. (40-00-0299-0448pb01)

Precise crystal orientation is perhaps the most difficult finishing specification. Beamlet tests in 1997 revealed spatial variations in frequency conversion efficiency that related to bulk crystal features, making the orientation process even more challenging. At the time, the only off-line method that existed for predicting frequency conversion performance of crystals involved using subaperture lasers to measure variations in their phase matching angles. The only production tool for this purpose was the Crystal Orientation Measurement System (COMS) at CCI. COMS compares the peak of the tuning curve of a proof crystal and a crystal being tested by comparing the amount of laser energy converted by each crystal as both are rocked in parallel beams on a common mount. However, the COMS configuration could only be used to access two points on each crystal.

Diagnostic techniques developed during Beamlet frequency conversion experiments have provided a breakthrough in this regard. Variations in frequency conversion efficiency correlate very well with variations in crystal birefringence determined simply by subtracting the transmitted wavefront through crystals at two orthogonal polarizations corresponding to the "o" and "e" transmission axes.[13] This technique, now called "orthogonal polarization interferometry" (OPI), provides a valuable alternative to mechanically complex two-dimensional scanning for determining the relative phase matching angles across the full aperture of crystals. However, OPI determines only the relative values across the crystal, not the absolute phase matching angle needed for NIF production.

The Crystal Alignment Test System (CATS), now under development, relies on OPI to determine the distribution of phase matching angles across a crystal. Small beam frequency conversion data from the CATS

will supplement the OPI with absolute phase matching angles for a line of points along the crystal. The two data sets can then be correlated to provide a map of the absolute phase-matching angle at all points on the crystal and an average phase matching angle that is used to correct crystal orientation during final finishing operations.

The CATS design, shown schematically in Figure 16, is conceptually very similar to the existing COMS in that each measurement is referenced to a precisely oriented proof crystal. Two parallel beams pass through the proof and test crystals, which are mounted on a single diamond-turned chuck. Pentaprisms are used to produce two parallel beam paths, thereby greatly simplifying the mechanical and controls requirements of the system. Because frequency conversion crystals are insensitive to out-of-plane rotation errors in the pentaprisms, there is no need to compensate for slide straightness errors or adjust beam alignment at each point in the scan line. During operation, one beam samples the proof while the other samples the crystal to be tested. The mount is rocked, and converted power is measured in both channels. The resulting tuning curves are curve-fit to determine the phase matching angle offset between the two crystals.

The use of calibrated proof crystals in CATS greatly reduces the sensitivity of the measurements to systematic errors, including temperature, laser wavelength, pointing jitter, etc. For example, by comparing crystals to a known proof, only the relative temperature between the proof and the crystal being tested must be controlled. The system is also insensitive to variations in laser wavelength between the NIF use wavelength and the CATS laser, since both the proof and crystal being tested see the same wavelength. There is only a minor error introduced if the deuteration level of a tripler crystal being measured is different from the tripler proof.

Conclusions

Rapid growth has now grown numerous boules of NIF size. The technical challenge for KDP is to increase process reliability and doubler yields to minimize costs, as all performance specifications have been achieved. Thermal annealing is an important aspect of meeting those specifications. The principal technical challenge for DKDP is to increase 3ω damage threshold at full size to the NIF requirement. The best DKDP grown in small tanks has better 3ω damage properties than needed for the NIF, but that level has yet to be demonstrated in large boules.

The Moore Final Finishing Machine, flatness machines, and CATS together form the primary foundation needed to meet the most difficult of the crystal finishing specifications. The Moore Final Finishing Machine is undergoing final testing. Mechanical assembly of the LLNL Prototype Flatness Machine is nearly complete, and compliance tests were very

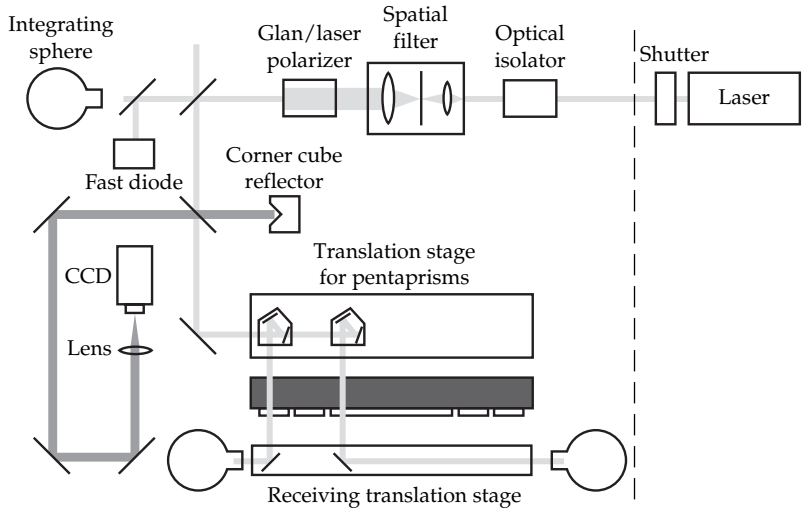

FIGURE 16. The conceptual layout of Crystal Alignment Test System reveals many similarities to COMS, its predecessor. (40-00-0299-0449pb01)

successful. A new CATS design takes advantage of new metrology techniques, and construction of several subsystems are ready to begin.

Acknowledgments

This work represents the efforts of dozens of people including Leslie Carman, Igor Smolsky, Sergey Potapenko, Martin DeHaven, Randy Floyd, Dick Spears, Mike Martin, and Warren Bell in the growth area, and Mary Norton, Jerry Auerbach, Larry Morris, Sue Locke, Gale Johnson, Sam Thompson, Gregg Wilkinson, Dave Kennedy, Stan Locke, Frank Gonzales, Dannie Johnson, Charles Cass, Blaine Beith, Mercedes Dickerson, George Weinert, Timm Wulff, Richard Arney, Dan Schumann, Inge Fine, Wayne Olund, and Chris Steffani in fabrication support.

Notes and References

1 N. P. Zaitseva, J. J. De Yoreo, M. R. DeHaven, R. L. Vital, L. M. Carman, and H. R. Spears, *J. Crystal Growth* **180**, 255–262 (1997).
2. N. P. Zaitseva, I. L. Smolsky, and L. N. Rashkovich, *Krystallografiya* **36**, 198 (1991).
3. J. J. De Yoreo, T. A. Land, L. N. Rashkovich, T. A. Onischenko, J. D. Lee, O. V. Monovskii, and N. P. Zaitseva, *J. Crystal Growth* **182**, 442–460 (1997).
4. N. P. Zaitseva, L. Carman, I. Smolsky, R. Torres, and M. Yan, "The effect of impurities and supersaturation on the rapid growth of KDP crystals," submitted to *J. Crystal Growth*.
5. L. N. Rashkovich and N. V Kronsky, *J. Crystal Growth* **182**, 434–441 (1997).
6. H. Robey, R. Floyd, R. Torres, and A. Burnham, "Impurity leaching rates of 1000 liter growth tanks," Lawrence Livermore National Laboratory, Livermore, CA, UCRL-ID-133365.
7. N. Zaitseva, J. Atherton, R. Rozsa, L. Carman, I. Smolsky, M. Runkel, R. Ryan, and L. James, "Connection between continuous filtration and dislocation structure of KDP crystals," submitted to *J. Crystal Growth*.
8. H. F. Robey and S. Potapenko, "Ex-situ microscopic observation of the lateral instability of macrosteps on the surface of rapidly grown KH_2PO_4 crystals," submitted to *J. Crystal Growth*.
9. H. F. Robey, S. Potapenko, and K. Summerhays, "Bending of steps on rapidly grown KH_2PO_4 crystals due to an inhomogeneous surface supersaturation field," submitted to *J. Crystal Growth*.
10. M. Runkel, J. De Yoreo, W. Sell, and D. Milam, "Laser Induced Damage in Optical Materials: 1997," in *Proc. SPIE*, vol. 3244, pp. 51–63.
11. B. Woods, M. Runkel, M. Yan, M. Staggs, N. Zaitseva, M. Kozlowski, and J. De Yoreo, "Laser Induced Damage in Optical Materials: 1996," in *Proc. SPIE*, vol. 3244, pp. 20–31.
12. M. Runkel, M. Yan, J. De Yoreo, and N. Zaitseva, "Laser Induced Damage in Optical Materials: 1997," in *Proc. SPIE*, vol. 3244, pp. 211–222.
13. P. J. Wegner et al., *Frequency Converter Development for the National Ignition Facility*, Lawrence Livermore National Laboratory, Livermore, CA, UCRL-JC-129725. Prepared for *Proc. 3rd Intl Conf on Solid State Lasers for ICF*.

Engineering High-Damage-Threshold NIF Polarizers and Mirrors

C. J. Stolz

F. Y. Genin

M. R. Kozlowski

Z. L. Wu

Polarizers and mirrors are required in the National Ignition Facility (NIF) to switch the pulse into and out of the main cavity and to direct the laser into the target chamber. Understanding the interaction of lasers with optical materials aids in the development of deposition techniques, coating designs, and postdeposition processes necessary to manufacture optical coatings that survive the fluences required for ignition. The thin-film deposition technique affects the microstructure of coating layers, the formation of defects, and the interface strength between defects and the multilayer. The coating design determines the standing-wave electric field in the coating and the plasma durability of the outer surface of the coating. Postdeposition processing by laser conditioning minimizes the effect of coating damage so that surface morphological changes remain stable with further irradiation. The effect of these damage sites on beam propagation must be understood to determine what size and type of damage is allowable.

Thin-Film Deposition Technology

A multitude of deposition techniques exist over a large range of deposition energies (0.01–5000 eV). The thin-film deposition technique must be carefully selected to meet the stringent coating requirements of the NIF. The optical substrates are large (up to 1 m diagonally) and numerous enough that the process should be scalable for coating multiple optics at a time. Spectral requirements are challenging, requiring complex thin-film designs with thickness control to less than 10 nm and full-aperture nonuniformities less than 1%. Coating stress must be minimized to prevent distortion of the laser beam wavefront. Finally, the coatings must not interact significantly with the laser during exposure to high fluences.

Electron-Beam Deposition

Electron-beam (e-beam) deposition, illustrated in Figure 1, is a technology that scales to large optics with sufficient precision to

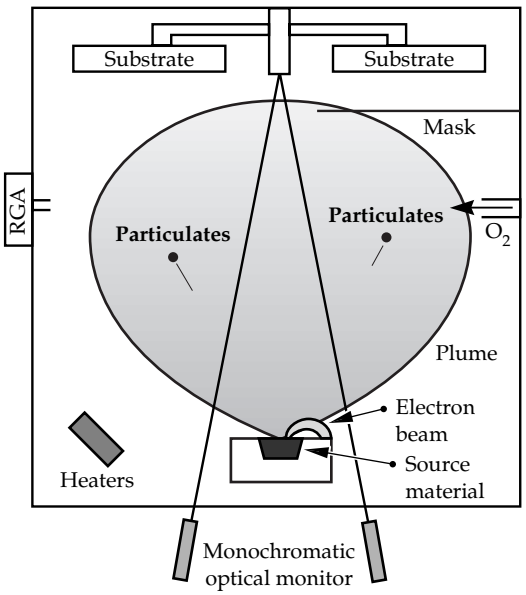

FIGURE 1. Typical e-beam deposition system.
(40-00-0299-0391pb01)

produce complex thin-film designs. This deposition technology has historically been the main tool of the laser-fusion community for making high reflectors and polarizers because laser-damage thresholds have historically increased with the requirements for higher ICF-laser energies. Significantly less effort has been put into alternate deposition processes, so they remain relatively unoptimized for high-fluence, large-aperture fusion optics.

The e-beam deposition process consists of an electron beam generated by thermionic emission from a filament. The beam is focused and directed by permanent magnets to a grounded source material. To minimize source-material drilling, electromagnets are used to raster-scan the beam over the surface. A reactive deposition environment provides greater flexibility in selecting source material compositions that interact more favorably with the e-beam.

The surface topography of the source material affects the stability and uniformity of the deposition plume (Figure 2) that has a cosine function distribution normal to the incident surface. An irregular surface leads to an unstable deposition plume that limits the layer-thickness control required to successfully coat the complex NIF designs. If the source material is an oxide, a small molten pool forms in the immediate vicinity of the e-beam due to the low thermal conductivity of the dielectric source material. The e-beam must be swept over the source material to prevent drilling or boring, which changes the deposition angle. Oxide source materials also tend to have an irregular surface because they are initially formed from multiple pellets. A metallic source material, deposited in a reactive environment to generate an oxide film, has a lower melting point and higher thermal conductivity. Therefore, a large, flat, molten metal surface with minimal drilling produces a stable deposition plume, as illustrated in Figure 2. A 3× improvement in plume stabilization is experimentally observed when switching from hafnia (HfO_2) to hafnium (Hf) source material.[1]

The interaction of the e-beam with the starting material generates particles that can be incorporated into the film as coating defects.[2] Hafnia plugs have poor packing densities due to their low thermal conductivity. Small air voids in these plugs are exposed by the oscillating e-beam, resulting in ejected particles. Additionally, a phase transformation exists in hafnia at ~1700°C. During evaporation the top surface of the hafnia is molten at ~2200°C and the bottom and edge surfaces are in contact with a water-cooled crucible at ~100°C. There is therefore a region in the material that undergoes a monoclinic to tetragonal phase transformation, resulting in a volumetric expansion of 3.8%. Volume-induced stresses, then, may also eject particles.

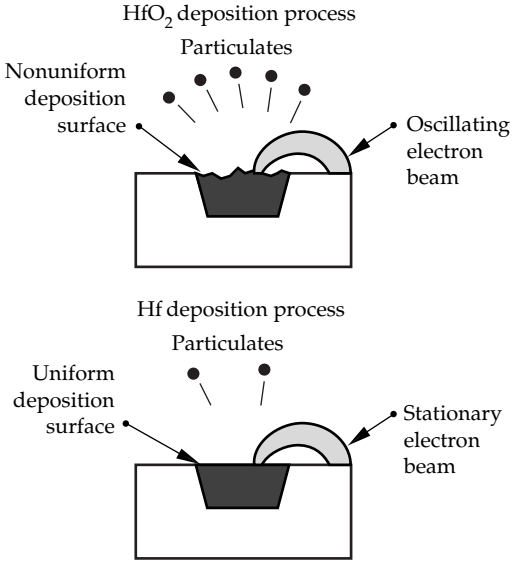

FIGURE 2. Source material composition affects interaction between the electron-beam and the source material, and the density of particle formation.
(40-00-0299-0414pb01)

Ion-Beam Deposition Methods

In the quest to achieve thin films resistant to higher laser energies, other coating processes have been investigated for higher damage thresholds than the e-beam process. Two of the more promising methods that have been studied are ion-assisted deposition (IAD) and ion-beam sputtering (IBS). IAD uses a conventional e-beam source to generate the deposition plume and an ion gun pointed at the optical substrate to increase the energy of the deposited particles (Figure 3). IBS uses an ion source that strikes a target to sputter atoms with higher arrival energies onto the substrate (Figure 4). The higher energy of the deposited particles from these techniques generates denser films than e-beam coatings. These lower-porosity

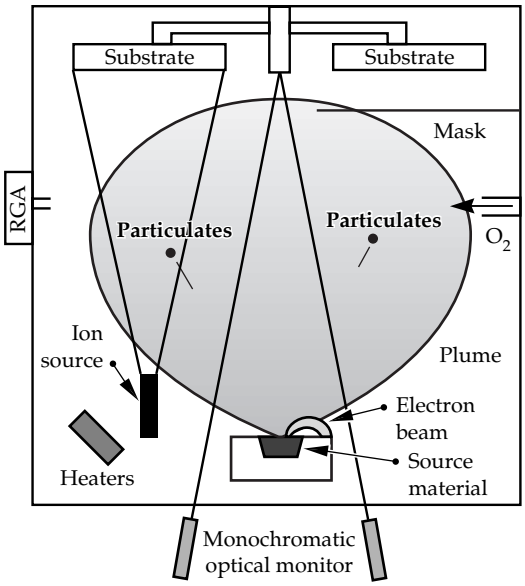

FIGURE 3. Typical IAD deposition system.
(40-00-0299-0415pb01)

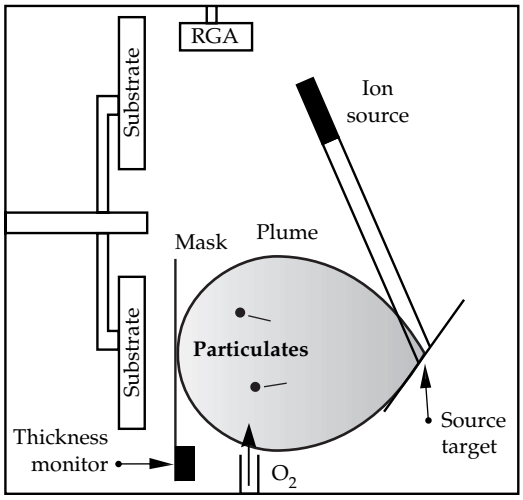

FIGURE 4. Typical IBS deposition system.
(40-00-0299-0416pb01)

films are less sensitive to humidity-induced spectral shift and stress changes.[3] Although environmental insensitivity is desirable from a spectral and stress perspective, the increased film stability causes defects to be more tightly bound resulting in catastrophic ejections during high-fluence irradiation. These damage sites generally grow upon continued irradiation, whereas most e-beam-coating nodular-ejection sites are stable at the NIF peak fluence.[4]

Laser Damage

Lasers create damage in optical thin films when they exceed the damage fluence of the coating. Figure 5 illustrates typical damage morphologies of hafnia–silica multilayer coatings. The four most common damage morphologies are:

- Delaminates.
- Flat-bottom pits.
- Nodular-ejection pits.
- Plasma scalds.

Only damage morphologies that grow, after continued laser exposure, to sufficient size to affect system performance must be prevented. Previous work has demonstrated that damage less than 280 μm in diameter will not degrade the performance of the laser.[5] Because the components must survive multiple shots, we must understand the growth of the various damage morphologies to determine coating lifetimes (Figure 6).[6] Therefore, careful characterization of these morphologies is necessary to determine which are fluence-limiting, how they affect the lifetime of an optical coating, and what are their sources.

Delaminates

Delaminates grow at the lowest fluence and quickest rate, so improvements in the coating damage threshold must start with elimination of this morphology. Delaminates are caused by the removal of the outermost layer, most likely due to thermally induced mechanical stresses such as buckling. Several phenomena imply that a surface plasma causes the delamination damage morphology. Plasmas are always observed during irradiation in coating areas that delaminate, with a strong correlation between plasma size and delaminate size. Delaminates can be found around coating defects and also in defect-free regions. The scanning-electron micrograph (SEM) in Figure 5 reveals signs of mechanical failure, such as curled and torn edges of the delaminated overlayer. The lack of plasma scalding in or around the delaminated site suggests that the scalded overlayer tears when the plasma extinguishes or when the plasma

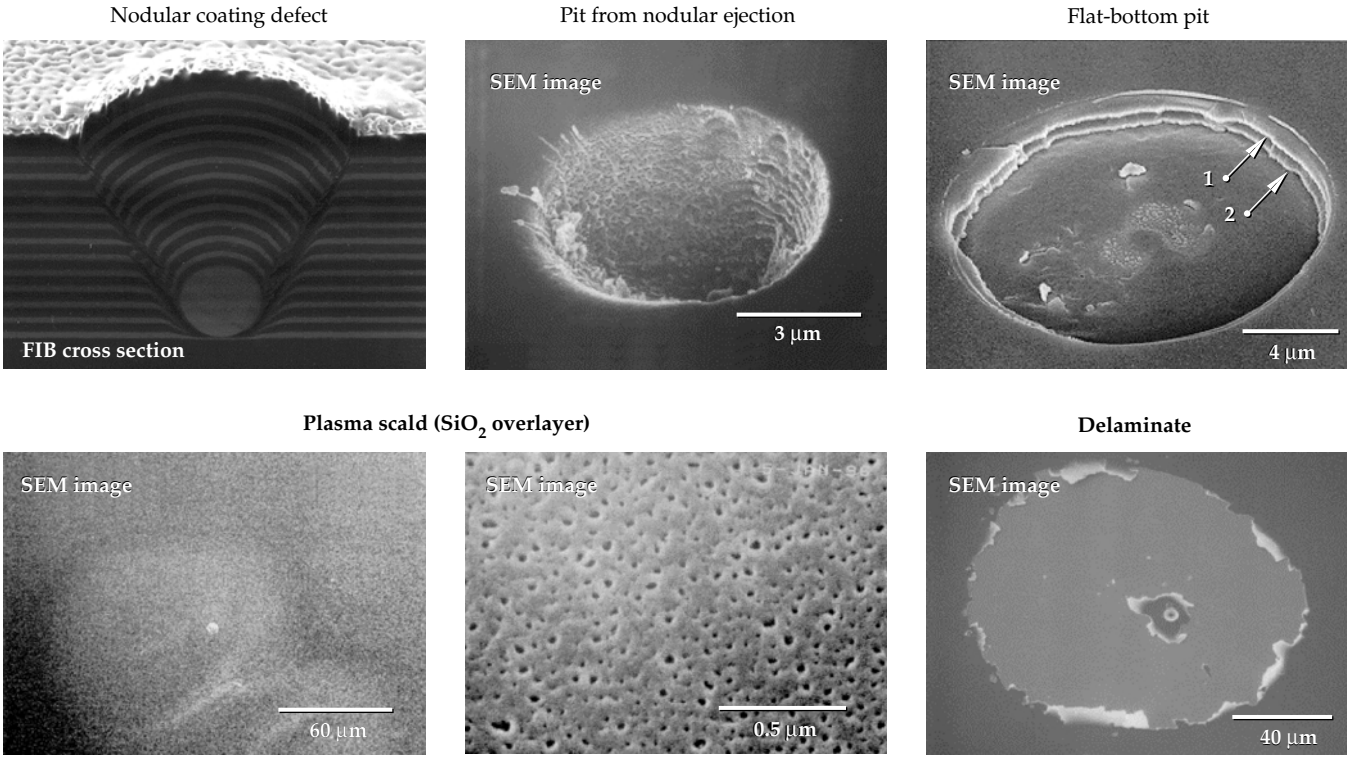

FIGURE 5. SEM images of laser-induced damage morphologies in hafnia–silica multilayer mirror and polarizer coatings. (40-00-0299-0417pb01)

FIGURE 6. Growth of various damage morphologies exposed to multiple-shot irradiation for a range of fluences indicates that delaminates are unstable while the other morphologies are benign at NIF fluences of 10.5 J/cm^2 (polarizers) and 21.9 J/cm^2 (mirrors) at pulse lengths of 3 ns. (40-00-0299-0418pb01)

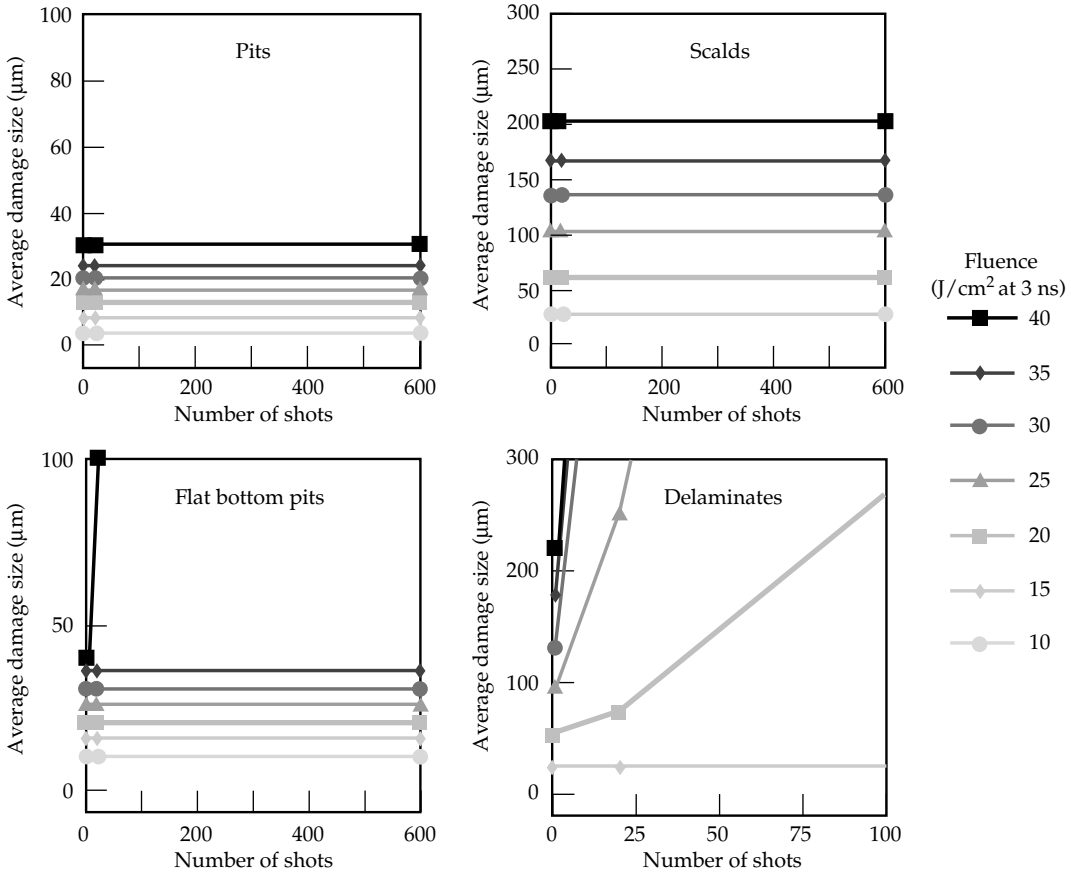

propagates away from the surface during overlayer ejection.

Delaminates in polarizers are affected by laser incident angle. Delaminates occur at Brewster's angle in the Beamlet-design coatings, yet they are eliminated at an incidence of 45 degrees, suggesting an electric-field dependence.

Maintaining a minimum overcoat thickness eliminates delaminates.[7] A polarizer coating consists of three parts—a polarizing stack with antireflection coatings on both sides. The thickness of the outer low-index layer is determined by optimization of the design for high transmission of "P" polarized light. Typical optimized edge-filter-design polarizer coatings, such as those used in the Beamlet polarizer, have overcoat optical thicknesses of about $\lambda/7$ (~150 nm physical thickness). These designs delaminate easily during laser exposure. Polarizer coatings with overcoats thicker than $\lambda/3$ (~300 nm physical thickness) do not show this delamination, even in the presence of plasmas from nodule ejections. Previous work has demonstrated that damage threshold improves for high reflectors with silica overcoats that have a $\lambda/2$ optical thickness.[8] This type of overcoat does not affect the spectral characteristics of the coating at the design wavelength and therefore is an "absentee layer." If the optimized design has a thin overlayer, an additional $\lambda/2$ can be added to the thickness to eliminate delaminates (as shown in Figure 7) without sacrificing optical performance.

Flat-Bottom Pits

Flat-bottom pits are circular divots that fracture along interfaces correlating to electric-field maximums. They are interfacial in nature and typically occur within the first few outer layer pairs. Flat-bottom pits in hafnia–silica multilayer coatings grow at high fluences, so they could affect the optic lifetime. These pits are created around nodular-ejection sites as well as in the absence of visible defects. The current theory is that the presence of embedded nanometer-scale absorbing seeds is responsible for the formation of flat-bottom pits.[9] This theory states that there is sufficient energy at electric-field peaks to create a plasma, leading to film buckling and localized radiation damage.[10,11]

During development of hafnium deposition for high-damage-threshold coatings, it was found that flat-bottom pits did not occur in hafnium-deposited coatings irradiated at NIF fluences, but they did occur in hafnia-deposited coatings. Several factors could explain the dependence of the starting material composition on this damage morphology, including improvement of interfacial strength and elimination of nanometer-scale absorbing seeds. It is not surprising that the interfacial quality in these coatings is material-dependent, because the hafnia layers are polycrystalline and rough while the silica layers are amorphous and smooth. However, starting material composition also affects interfacial quality; coatings deposited from hafnium and silica have fewer interfacial

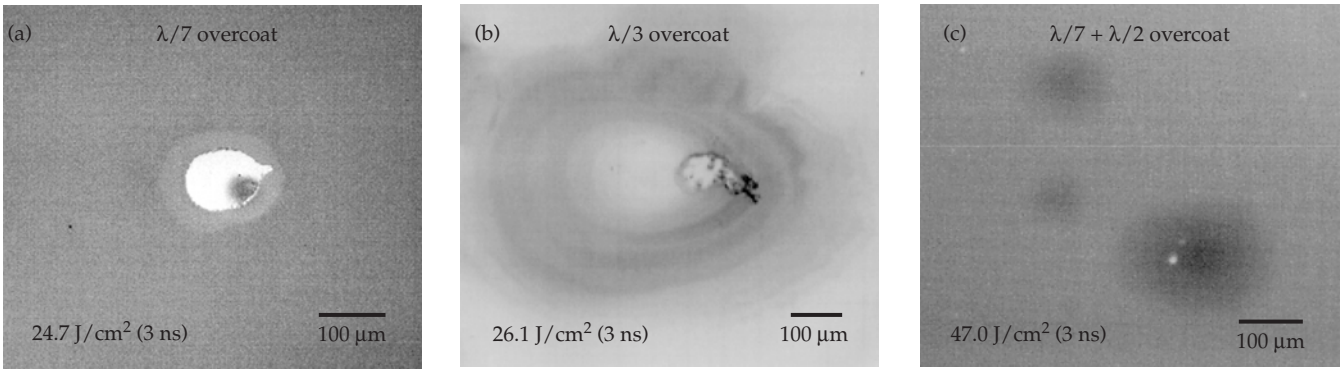

FIGURE 7. Thicker polarizer overcoats significantly improve laser-damage morphology. In micrographs (a) and (b), delamination occurs within the scalds. In (c), no delamination occurs. (40-00-0299-0419pb01)

voids than those deposited from hafnia and silica (Figure 8). The effect of starting material composition on the presence of absorbing seeds is unknown.

To better understand the influence of the two different interfaces, a modified high-reflector design was deposited to cause electric-field peaks at both types of interfaces.[12] Simultaneously, a standard high reflector was deposited as a control piece. The coatings were deposited using hafnium and silica starting materials. After damage testing, flat-bottom pits were not observed on the standard high reflector at up to twice the NIF fluence, although some interfacial damage occurred at the substrate/thin-film boundary. The modified design had flat-bottom pits due to the significantly higher electric fields, but only at the hafnium-over-silica interface (Figure 9).

Nodular-Ejection Pits

The ejection of nodular defects during laser exposure results in a crater-like pit. Modeling of nodular defects reveals up to a 5× increase in the electric field due to the nodule geometry.[13] These enhanced electric fields create localized, thermally induced stresses that are the likely cause of nodular ejection.

To understand the relationship between nodule size and damage threshold, an atomic force microscope (AFM) was used to characterize nodules before and after laser irradiation.[14] A correlation was observed between nodule height (which is proportional to the defect-seed diameter) and damage threshold. The increase of electric-field enhancement with larger seed size correlates well with the observation that

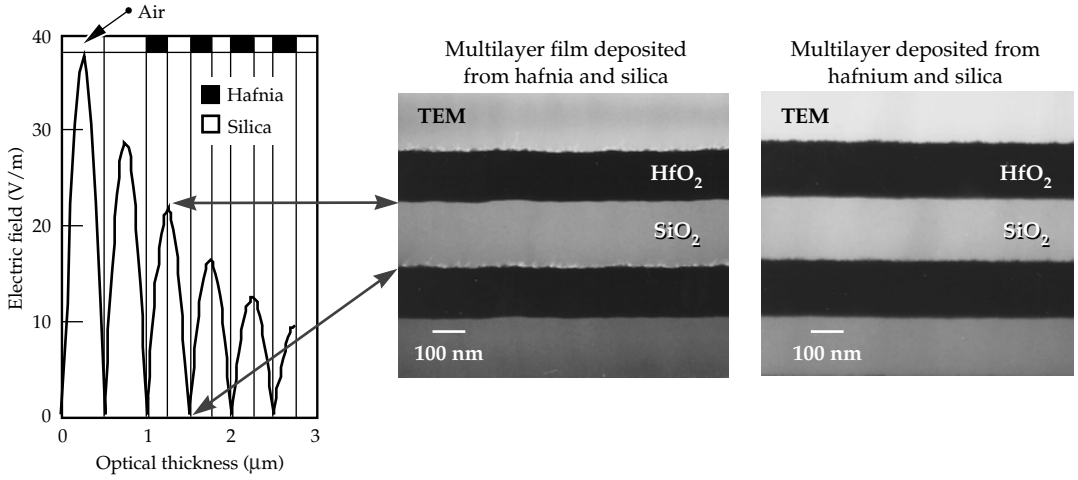

FIGURE 8. Interface quality as a function of starting material composition.
(40-00-0299-0420pb01)

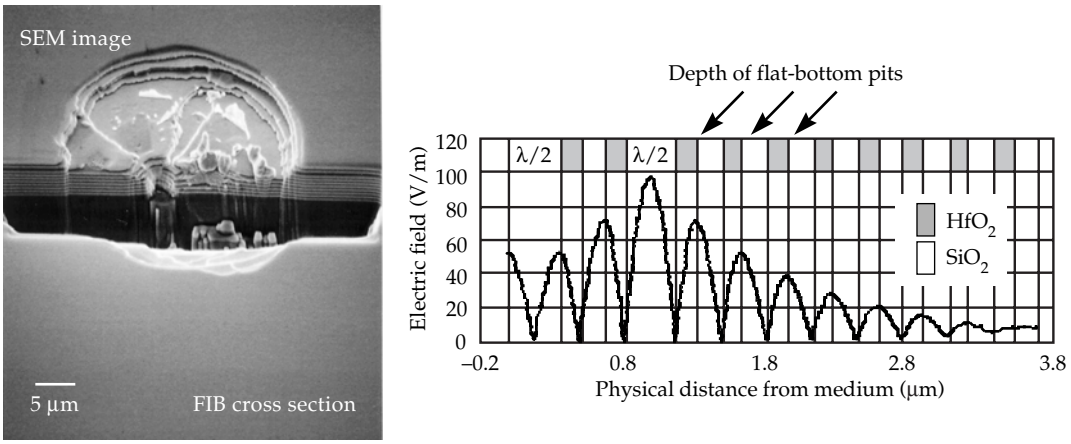

FIGURE 9. Flat-bottom pit depth correlates to hafnia grown over silica interfaces at electric field peaks.
(40-00-0299-0421pb01)

larger-diameter seeds have a lower damage threshold. This information can be used to optimize the coating processes so that defects are too small to damage the coatings at the operating fluence of the NIF laser.

The coating process is inherently unstable, resulting in the generation of particles that become embedded in the coating. The primary defect source in the coating process is material ejected from the source, but defects are also caused by material that flakes off shields around the chamber walls and the tooling, particles from the interaction of the e-beam with the source material, and particles from arcing of high-voltage surfaces.[15] The e-beam coating process takes place at an elevated temperature around 200°C. The thermal expansion of stainless-steel tooling and aluminum shields is different than that of the coating materials, causing the coatings on the interior metal surfaces to delaminate. Fracturing and delamination can also be caused by intrinsic stresses in the coating material (due to the buildup of coatings over multiple runs) and weak adhesion of the coating material (due to the monolayers of adsorbed gasses and organic contaminates from the metal-cleaning process). All these particles can be transported by the thermal plume onto the optical surfaces being coated.[16] Proper chamber preventive maintenance and cleanliness are required to produce high-damage-threshold coatings.

A focused ion beam (FIB) can be used to characterize the nodules to determine their origin.[17] The FIB is positioned perpendicular to the nodule and raster-scanned across it; half of the nodule material is removed by sputtering to reveal a vertical cross section (Figure 10). Once half of the nodule is exposed, the FIB fluence can be decreased and positioned to an incidence angle of about 60 degrees from normal. By bombarding the cross-sectioned surface at this angle, secondary ions are generated and collected to produce high-resolution images of the nodule, which reveal information about the defect seed size, shape, and chemistry (Figure 11). This information can be used to infer the origin of the seed.

Round, smooth-edged seeds indicate molten ejecta from the interaction of the e-beam with the source material. Rough-edged seeds indicate solid ejecta from either e-beam/source interaction, arcing of coated surfaces, or particles that contaminated the substrate before coating. By comparing the contrast of the seed with the individual coating layers, particle composition can be inferred. Thick hafnia flakes and thin multilayer flakes have also been

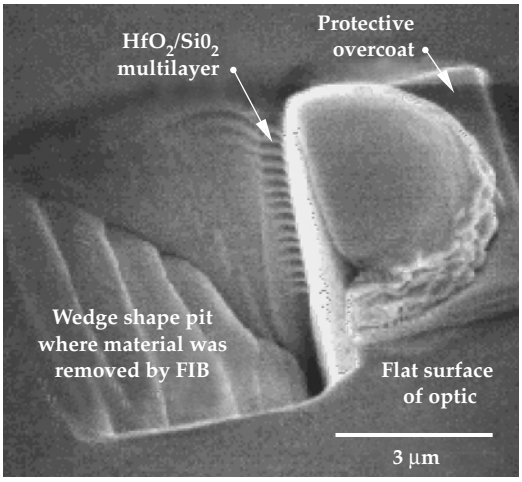

FIGURE 10. Focused-ion-beam milling is used to cross-section coating defects for characterization of the seed. (40-00-0299-0422pb01)

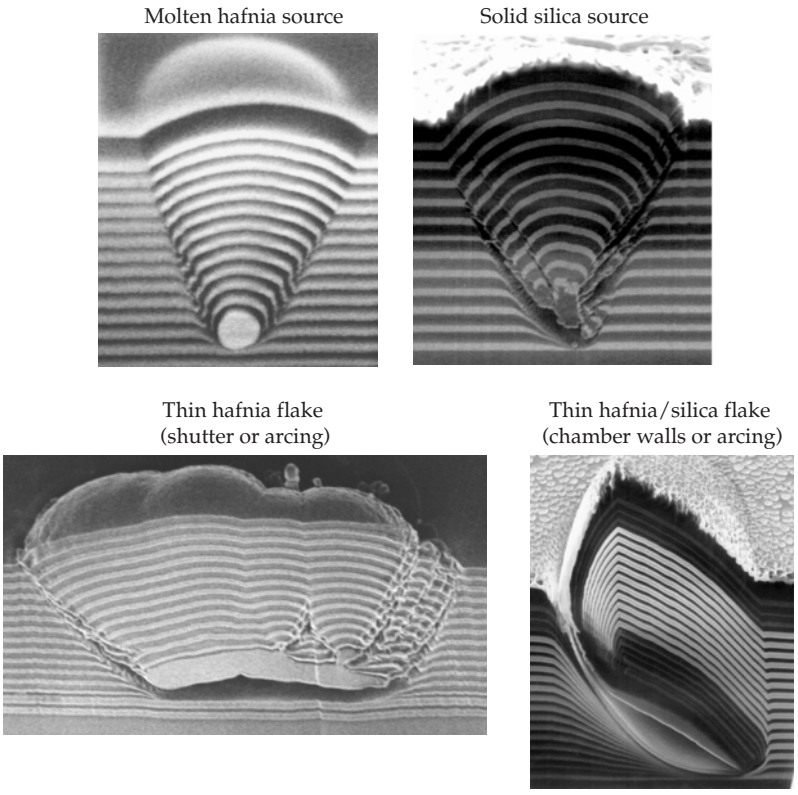

FIGURE 11. Comparison of nodular defect seed geometries from various deposition techniques. (40-00-0299-0423pb01)

observed, indicating that coating flakes from chamber surfaces can become incorporated into the coating during deposition.

Defects in IBS coatings typically occur with a lower density than e-beam coatings. Laser-damage thresholds in small areas are typically very high (>40 J/cm^2 at 3 ns), due to the low probability of irradiating a defect. Unfortunately, large-aperture damage thresholds with a higher probability of containing a fluence limiting defect are significantly lower (~10 J/cm^2 at 3 ns) than those of typical e-beam films of the same coating materials and optic size. One possible explanation is illustrated by the difference in the boundaries between the defects and the multilayer for e-beam and IBS coatings. IBS coatings typically have continuous boundaries, even for large defects, but large e-beam defects have significantly convoluted, weaker boundaries. Laser-interaction experiments on IBS coatings show that large defects ejected at low fluences grow considerably with repeated irradiation, but large ejected defects in e-beam coatings typically have significantly less damage that is more stable.

Laser Conditioning to Minimize Damage

The severity of pitting can be reduced by ejection of nodular defects at fluences lower than the peak NIF fluence. The process of irradiating the coating at lower fluence is termed laser conditioning. Figure 12 illustrates the laser conditioning method used to raster-scan a large-aperture optic, with each subsequent scan at a higher fluence. Nodular defects have different damage thresholds depending on the diameter and depth of the seed.[18] The lower the laser fluence that is used to eject a nodular defect, the smaller the plasma that is created, reducing the probability of microcracks propagating from the pit and decreasing the size of the plasma scald. After the nodule is ejected, a high-damage-threshold pit remains because electric fields are low in smooth pits. Nodules ejected at higher fluences have a greater probability of generating microcracks, which on subsequent shots result in electric-field-enhancement sites for plasma formation that can lead to runaway growth.

Large-aperture laser conditioning of coatings has been demonstrated to improve the damage threshold of optical coatings.[19] To reduce the cost of laser conditioning, a single-step laser conditioning method was tested.[20] By exploiting the Gaussian shape of the beam and raster scanning, the surface is exposed to a fluence ramp needed for conditioning (Figure 13). Beamlet mirrors were successfully conditioned with this technique.

Plasma Scalds

A plasma scald is created when a plasma forms during irradiation and erodes the overlayer. In the eroded area, a rougher surface with higher surface energy is observed; the improved wettability of the scalded surface indicates surface cleaning or charging by the plasma. Previous work has shown that the damage threshold of a coating can be significantly increased by adding a $\lambda/2$-thickness low-refractive-index layer, which does not affect the spectral performance of the coating.[8] Although the reasons for the

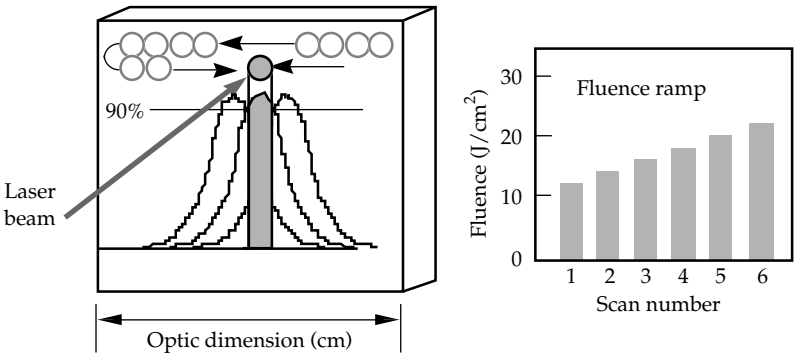

FIGURE 12. Six-step laser conditioning process.
(40-00-0299-0424pb01)

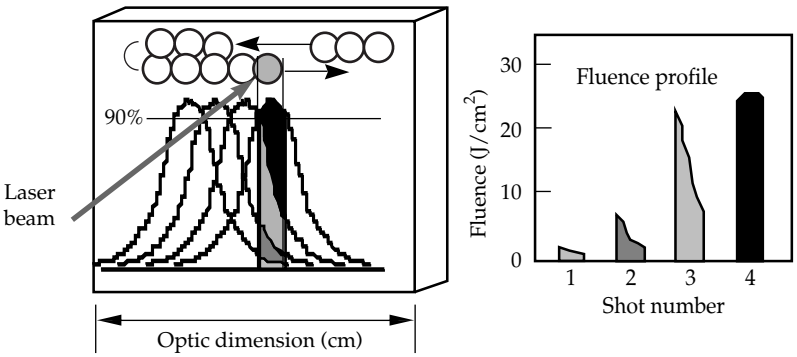

FIGURE 13. Single-step laser conditioning process.
(40-00-0299-0425pb01)

improvement in the damage threshold are not well understood, the difference in the magnitude of surface erosion due to the presence of a plasma during irradiation is significant. Upon repeated exposure to laser pulses, low-index material shows minimal erosion (~6 nm), but high-index material erodes completely through to the next layer (~140 nm; Figure 14).

The only observable, stable, damage morphology larger than the critical 280-μm size was plasma scalding, so the effect of the scalds on the laser beam was characterized. Plasma scalds are the result of partial erosion of the outer layer, so they can be modeled as micromirrors. To create sufficient focusing to overcome diffraction effects, the erosion thickness would have to penetrate the overlayer.[21] Typical depths of plasma scalds with silica overcoats are less than 5% of a layer thickness, so they behave as scatter sites, not as focusing elements.

Measurements were also conducted to understand the influence of the increasing surface roughness on the reflectivity of the scalded area. A 50-mm-diameter plasma scald was clearly visible to the naked eye as a discoloration of the coating. However, reflectivity measurements at the NIF laser wavelength showed no degradation within the resolution of the Nova photometer with an accuracy of ± 0.2%.

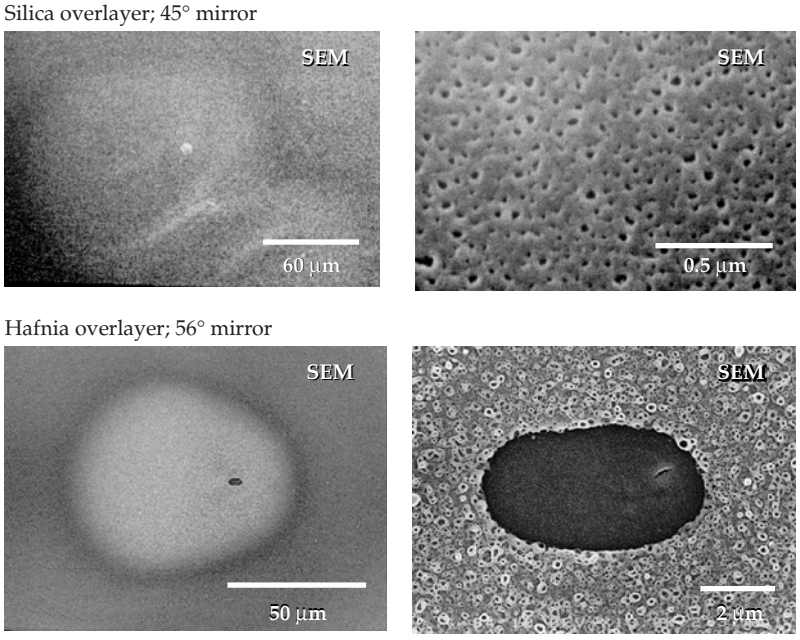

FIGURE 14. Plasma-scald erosion depth is minimized with a silica overlayer.
(40-00-0299-0426pb01)

Current Technology Status

Under the NIF coating-development program, laser-conditioned coatings typically have zero to four defects, over the Beamlet aperture, that limit the peak fluence. Previous laser-interaction studies were done on small samples because of their larger defect density, maintaining a statistically significant sampling of defects; these smaller samples are easily characterized under a variety of techniques, including AFM, SEM, and FIB. To characterize fluence-limiting defects, a nondestructive technique that can scan the entire surface will have to be used. Photothermal microscopy currently holds the greatest potential for nondestructively identifying fluence-limiting defects, as shown by the good correlation between high photothermal signal and low damage threshold illustrated in Figure 15.[22,23] However, the current data-acquisition rate is so slow that scanning a NIF-size optic would take approximately 200 days.

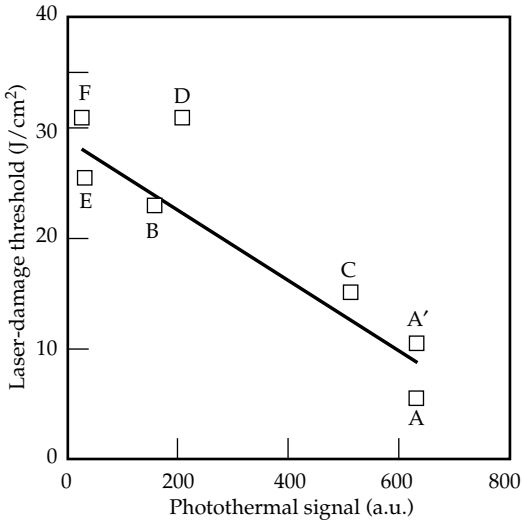

FIGURE 15. Photothermal signal correlates well with the laser-damage threshold. (40-00-0299-0427pb01)

If fluence-limiting defects are present on NIF optics, their effect on optic lifetime will be mitigated by several statistical factors. Because only a small percentage of the coated surface is exposed to the NIF peak fluence, damage growth will only occur when a low-density, fluence-limiting defect—which populates only ~0.0005% of the surface—is struck by the highest-fluence regions of the beam. The average growth rate of damage sites will be reduced because many of the NIF shots will be below peak fluence. Finally, coatings will be conditioned at fluences slightly below peak to minimize conditioning-induced damage, also slowing damage growth.

Summary

Optical coatings can be generated by several energetic processes, including e-beam deposition, ion-assisted deposition, and ion-beam sputtering. E-beam coatings have demonstrated the highest large-aperture damage thresholds for fusion lasers. By understanding the sources of various damage morphologies, the coating process and design can be engineered to produce coatings capable of withstanding NIF fluences. Delamination can be eliminated by selection of an appropriate overcoat thickness. Flat-bottom pits can be eliminated through strengthening the layer interfaces by starting with hafnium instead of hafnia or reducing the peak electric fields at the layer interface. Nodules are reduced by good substrate-cleaning techniques, proper chamber maintenance, and the use of hafnium instead of hafnia to reduce ejected particles. The severity of nodular-ejection pits and plasma scalds can be minimized by laser conditioning—irradiating at successively higher fluences to induce nodular ejection at fluences below operational values—to reduce plasma formation and microcracking.

Notes and References

1. C. J. Stolz, M. K. Von Gunten, R. P. Bevis, and D. Smith, "The advantages of evaporation of hafnium in a reactive environment to manufacture high damage threshold multilayer coatings by electron beam deposition," in *Proc. SPIE*, to be published.
2. R. Chow et al., *Appl. Opt.* **32**, 5567–5574 (1993).
3. P. J. Martin et al., *Appl. Opt.* **22**, 178–184 (1983).
4. C. J. Stolz et al., *Proc. SPIE* **2714**, 351–358 (1996).
5. J. T. Hunt, K. R. Manes, and P. A. Renard, *Appl. Opt.* **32**, 5973–5982 (1993).
6. F. Y. Genin, C. J. Stolz, and M. R. Kozlowski, *Proc. SPIE* **2966**, 273–282 (1996).
7. C. J. Stolz et al., *Proc. SPIE* **2966**, 265–272 (1996).
8. B. E. Newnam, "Laser-induced-damage phenomena in dielectric films, solids and inorganic liquids," Ph.D. dissertation, Univ. of Southern California (1973).
9. J. Dijon et al., *Proc. SPIE* **2714**, 416–424 (1996).
10. J. Dijon, T. Poiroux, and C. Desrumaux, *Proc. SPIE* **2966**, 315–325 (1997).
11. J. Dijon, G. Ravel, and B. André, *Proc. SPIE*, **3578**, 398–407 (1998).
12. S. C. Weakley et al., *Proc. SPIE*, **3578**, 137–143 (1998).
13. R. H. Sawicki, C. C. Shang, and T. L. Swatlowski, *Proc. SPIE* **2428**, 333–342 (1995).
14. R. J. Tench, R. Chow, and M. R. Kozlowski, *J. Vac. Sci. Technol. A* **12**, 2808–2813 (1994).
15. F. L. Williams, G. A. Peterson, R. A. Schmell, and C. K. Carniglia, *Proc. SPIE* **1624**, 256–270 (1991).
16. S. Matteson and R. A. Bowling, *J. Vac. Sci. Technol. A* **6**, 2504–2507 (1988).
17. C. J. Stolz, R. J. Tench, M. R. Kozlowski, and A. Fornier, *Proc. SPIE* **2714**, 374–382 (1995).
18. M. R. Kozlowski, R. J. Tench, R. Chow, and L. M. Sheehan, *Proc. SPIE* **2253**, 743–750 (1994).
19. L. M. Sheehan, M. R. Kozlowski, F. Rainer, and M. C. Staggs, *Proc. SPIE* **2114**, 559–568 (1994).
20. C. J. Stolz et al., *Proc. SPIE*, **3578**, 144–153 (1998).
21. F. Y. Genin and C. J. Stolz, *Proc. SPIE* **2870**, 439–448 (1996).
22. C. J. Stolz et al., *Proc. SPIE* **3244**, 475–483 (1998).
23. Z. L. Wu et al., "Characterization and laser damage testing of fluence limiting defects in hafnia/silica multilayer coatings developed for the National Ignition Facility," to be published.

Improved Antireflection Coatings for the NIF

P. K. Whitman
J. Fair
R. Aboud
A. K. Burnham
S. C. Frieders
I. M. Thomas
C. B. Thorsness

For many years, quarter-wave porous-silica antireflection (AR) coatings prepared by a sol-gel process have been used on the transmissive optical components of high-powered fusion lasers. These include the two most powerful machines now operating: the 10-beam Nova laser at Lawrence Livermore National Laboratory in Livermore, California, and the 60-beam OMEGA laser at the University of Rochester's Laboratory for Laser Energetics in Rochester, New York. Although the optical performance of these sol-gel coatings is no better than coatings prepared by other methods, their laser damage threshold is two to three times higher.[1] It is thought that this enhanced damage threshold results from the extremely high purity obtained by distilling the starting materials and the lack of collateral damage when small particulate contaminants are ejected. Optical component damage has always been the limiting factor for power output, so sol-gel coatings have made a significant contribution to high-power laser development.

One-layer, porous, colloidal sol coatings can meet the optical and damage requirements for all of the National Ignition Facility's (NIF's) transmissive optics, except for the two mixed-wavelength surfaces on the frequency conversion crystals. Developing two-layer broadband coatings and coating processes that are compatible with the conversion crystals' requirements has been one area of focus for improving NIF laser AR coatings. The second area of active research is the long-term performance of both one-layer and broadband AR coatings using porous sol layers. The high specific surface area of sol coatings makes them susceptible to contamination by vapor adsorption from their environment. This contamination has been linked to decreases in optical performance and laser-damage thresholds. Furthermore, water vapor adsorption by the highly reactive surfaces of diamond-turned potassium dihydrogen phosphate (KDP) crystals can promote their degradation. Methods to reduce contamination uptake and processes that reduce the partial pressure of organic contaminants in the ambient use environment have yielded notable improvements in the lifetime performance of porous sol-coated transmissive optics.

Antireflection Coating Development

The sol-gel AR coatings consist of a layer of porous, near-spherical silica particles, 10 to 40 nm in diameter, randomly stacked on the substrate surface. Inter-particle voids combine with the particles' interior porosity to produce a film refractive index very near to the square root of the indices of many common optical substrates (1.46 to 1.52); nearly 100% transmission can therefore be obtained. Unfortunately, such highly porous coatings have high specific surface areas and are therefore very susceptible to contamination by vapor adsorption from their environment. The majority of the NIF's AR coatings must have an optical thickness tailored to deliver 99.50% (or better) transmission per optic at the primary laser wavelengths of

1053 nm (1ω) and 351 nm (3ω). Figures 1a and 1b show the acceptable refractive-index and film-thickness ranges, respectively, for one-layer AR coatings. In order to deliver the required performance, the total coating process variation, including manufacturing variances and effects from contaminants, must remain within the largest limits shown in Figure 1. Those transmissive optics that also serve as diagnostic surfaces (the diagnostic beam splitter, final focus lens, and beam sampling grating) have even stricter reflectance error tolerances. Thus, in some instances, the production coating capabilities must be compatible with these more demanding requirements.

The KDP/DKDP (deuterated) conversion crystals are the only optics in the NIF laser chain that must simultaneously transmit mixed wavelengths of light with very high efficiency. This requirement has implications for selecting acceptable AR-coating designs and thin-film processes. To independently optimize the coating for each crystal surface, it is necessary to develop a spin-coat process for 41-cm square optics with acceptable uniformity, repeatability, and low particulate contamination. In addition, for the output surface of the doubling conversion crystals and the input surface of the tripling conversion crystals, the single AR-coating design must be simultaneously optimized for both 1053-nm and 525-nm light. This can be accomplished by coating the surface with an AR layer having an optical thickness that produces a minimum of reflectance between these two wavelengths. Figure 2 compares the calculated reflectance from such a one-layer "compromise" coating (currently being used on deuterated tripling crystals) with that of a two-layer broadband AR coating used on KDP crystals for Nova and Beamlet. The one-layer coating surpasses the 0.7% goal for reflection losses established for these surfaces, while the two-layer coating meets the NIF's requirements.

Because the third-harmonic conversion efficiency is sensitive to the ratio of the photon fluxes of the fundamental and the second-harmonic beams incident upon the frequency tripling crystal, an excess of 1053-nm photons does not compensate for a loss of 525-nm photons, or vice versa. Hence, the optimal coating minimizes the larger of the reflection losses at either 1053 nm (1ω) or 525 nm (2ω). Figures 3a and 3b compare and contrast the sensitivities of the one-layer compromise coating and the two-layer broadband coating

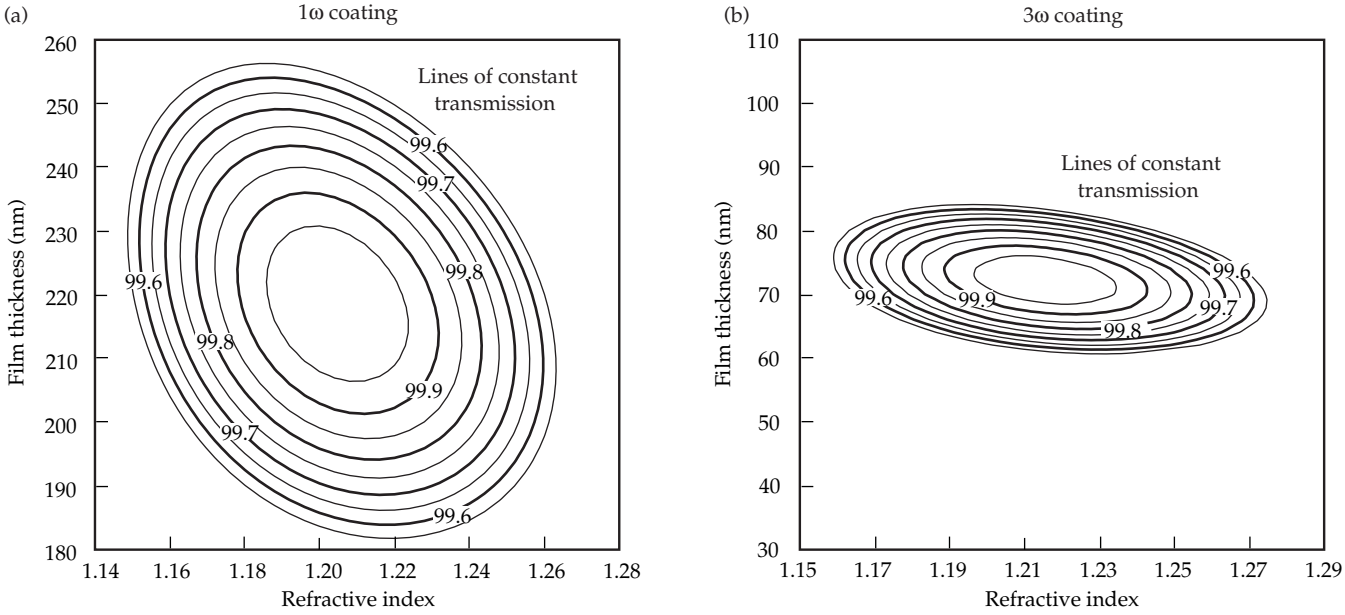

FIGURE 1. Optic transmission as a function of sol AR coating thickness and index: (a) contour for 1ω; (b) contour for 3ω coating.
(40-00-0299-0383pb01)

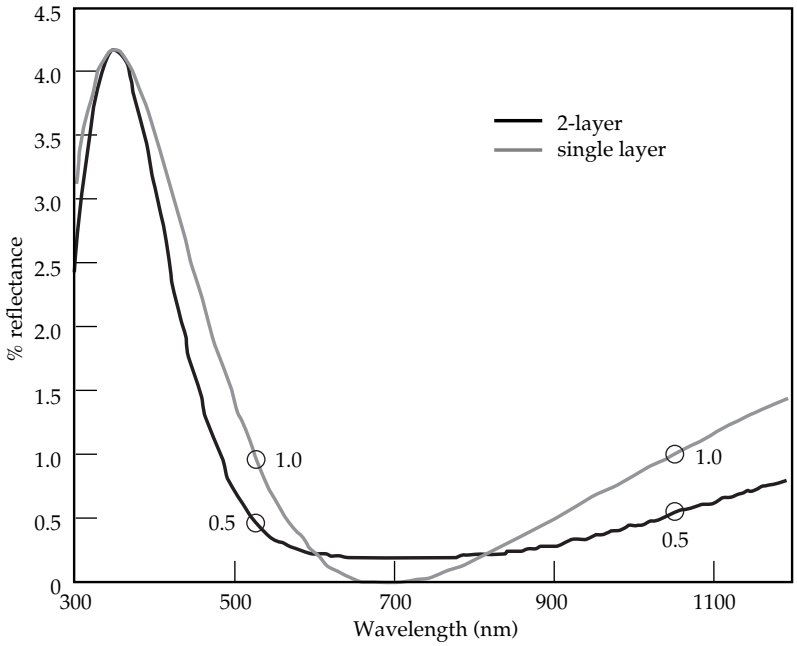

FIGURE 2. DKDP reflectance spectra calculated for a single and a two-layer broadband coating design for unpolarized light.
(40-00-0299-0384pb01)

designs to the expected variability in their manufacture. These coatings are much more sensitive to coating process errors, as well as being centered at a much higher theoretical reflectance than are the single-use wavelength coatings, as described in Figure 1. Compared to the one-layer compromise coating, the broadband coating design does not greatly reduce sensitivity to the sol-coating-layer's

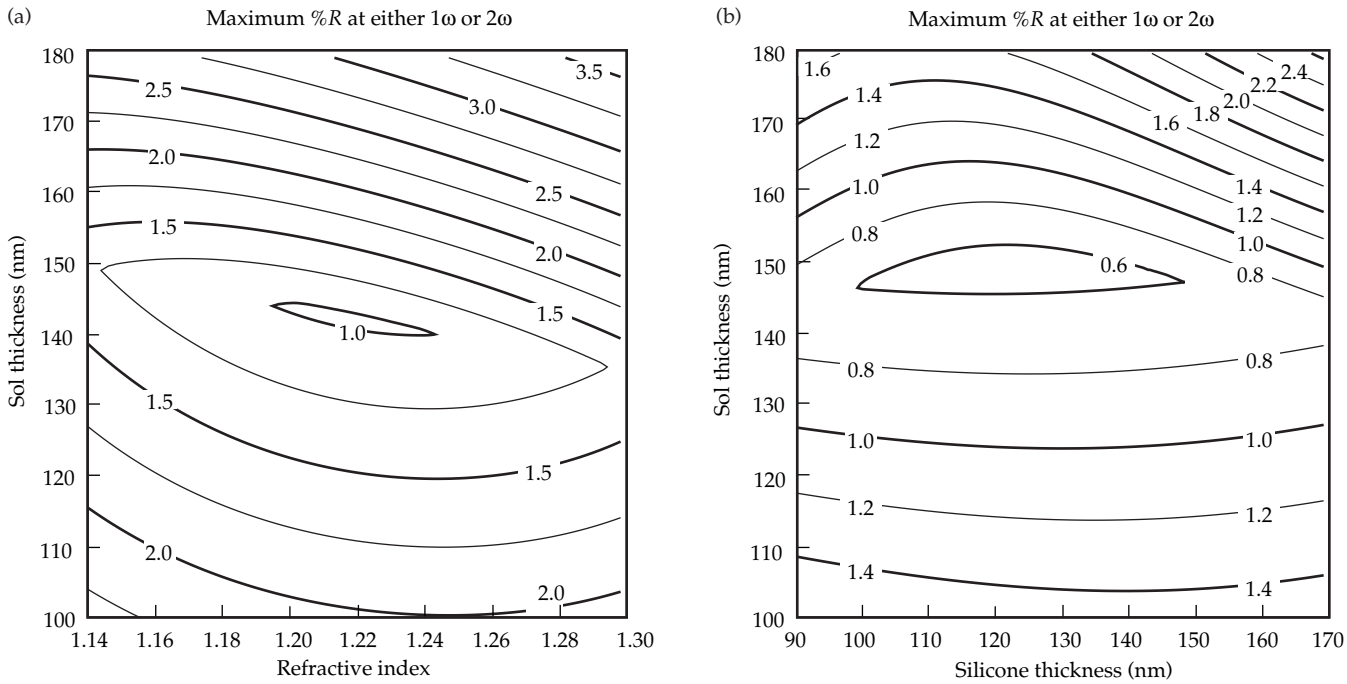

FIGURE 3. Single surface reflection for KDP coated with a 1–2ω compromise coating: (a) one-layer AR performance as a function of sol thickness and index; (b) two-layer broadband AR performance as a function of sol and silicone layer thickness, at fixed index (silicone, 1.43; sol, 1.22).
(40-00-0299-0385pb01)

thickness. However, since the two-layer coating design is centered at a lower reflectance, it yields a better performance for the same manufacturing variability. Due to the asymmetric contours for either a single- or a two-layer coating, a targeted coating thickness of 140-nm (slightly below optimum) allows a higher fraction of optics to fall within the desired reflectance specification.

Spin-Coat Process Development

The sensitivity of compromise coatings to variations in optical thickness increases the need to maximize their uniformity. Unfortunately, the spin-coat process used for Nova and Beamlet crystals has exhibited relatively poor uniformity and repeatability when compared to dip coating. The Nova/Beamlet spin coater relied on fairings to minimize air turbulence at the edges of the square crystals.

We recently purchased a commercial spin coater that was developed for coating large, rectangular substrates (such as flat-panel displays). In this system the cover spins with the optic, creating a quiescent, highly saturated air pocket with low air turbulence and slow solvent evaporation. Nevertheless, spin coating a sol from ethanol solvent with this system produced higher single-part and part-to-part variability than was desired. Therefore, we searched for a KDP-compatible solvent with a lower evaporation rate, and tried secondary butanol. At first, its higher viscosity and surface tension prevented us from coating the corners of the 37-cm square optics. We then replaced only two-thirds of the ethanol solvent with secondary butanol and improved the coating uniformity across a 37-cm part from a standard deviation of 0.1%, to one of 0.04%. Table 1 compares the capability of our current spin-coating process to the dip-coat and spin-coat processes used for Beamlet.

TABLE 1. A comparison of 1064-nm reflectance uniformity for 37-cm crystals that were coated by various processes.

Process	Solvent	$\sigma(\%R)$
Beamlet—dip coat	Ethanol	0.08
Beamlet—spin coat over dip coat	2-butanol over ethanol	0.15
NIF—spin coat	Ethanol	0.1
NIF—spin coat	2-butanol:ethanol (2:1)	0.04

Broadband Coating Development

The two-layer KDP coating used on the 27-cm Nova and the 32-cm Beamlet crystals consists of a methylsilicone bottom layer (with a refractive index of 1.43) that has been overcoated with porous silica.[2] The silicone coating is GR-650™, a commercial material available from Techneglas. It is applied from an alcohol solution and requires curing at 140°C. After being heat-cured, the material is insoluble and won't wash off when the colloidal sol coat is subsequently applied from a second alcohol solution.

The first 37-cm KDP crystal was coated with a two-layer broadband coating on one surface and a one-layer, 3ω sol coating on the opposing surface using the new (NIF) spin coater. Despite initial concerns that, with such a large crystal, either shrinkage of the silicone layer or the thermal cycle itself might distort the reflected wavefront, there was no measured change in the transmitted wavefront. Table 2 compares the NIF's goals to the measured reflectance and uniformity of this coated crystal.

The NIF's frequency-tripling crystals must be deuterated to suppress parasitic oscillations from stimulated Raman scattering. Deuterated crystals have catastrophically failed when heated above 100 to 120°C, so they are not compatible with the thermal treatment required by the existing broadband coating. It was therefore desirable to modify the chemistry of the intermediate-index (silicone) material to eliminate the need for elevated cure temperatures.

Coating Chemistry

The commercial silicone that we have used for many years is a polymer prepared by an acid-catalyzed hydrolysis of very high purity methyltriethoxysilane (MTS).

UCRL-LR-105821-99-2

TABLE 2. The performance of a 37-cm KDP crystal, coated by the NIF process and the spin coater.

Coating design	Wavelength (nm)	Reflectance (%)	σ(%*R*)
2-Layer compromise	1064	0.47	0.02
2-Layer compromise	532	0.34	0.07
One-layer 3ω	352	0.09	0.02

We have synthesized this polymer in our laboratory using MTS that was fractionally distilled under nitrogen.[3] The hydrolysis is done at pH 2, using a water/silane ratio of 2:1 and no solvent. The reaction is

$$n CH_3Si(OC_2H_5)_3 + 1.5n\ H_2O \rightarrow (CH_3SiO_{1.5})n + 3n\ C_2H_5OH\ . \quad (1)$$

The material produced by this reaction is incompletely cured and can be applied from an alcohol solution. This coating, as deposited, requires additional heat treatment to produce a fully cross-linked insoluble product. However, the polymerization of MTS, a trifunctional monomer, can be enhanced by adding a tetrafunctional monomer, such as tetraethylorthosilicate (TEOS). The extra functionality speeds up polymerization and increases the cross-linking required for rapid insolubility. The copolymerization of TEOS and MTS can be carried out in any proportion to obtain a soluble prepolymer, which can be cured to insolubility with little or no additional heating, depending on the relative proportions of the monomers.

The refractive index of the final product ranges between 1.42 and 1.43, which is indistinguishable from the original GR-650™ silicone and produces the same optical performance. The nominal laser damage threshold of this low-temperature-cure silicone is equivalent to that obtained with the commercial GR-650™ silicone and exceeds the expected peak fluences of the combined 1053- and 525-nm laser light.

There are actually two applications for an AR coating using this room-temperature cured, intermediate-index layer: conversion crystals and blast shields for the NIF amplifier assemblies. Although the preferred cure times are somewhat different for the two applications, we were able to accommodate both. When equimolar quantities of MTS and TEOS are premixed and then hydrolyzed with water at pH 2 (with no solvent), we prepare a coating that becomes insoluble on standing at room temperature for a few hours, or preferably overnight. It can be easily washed off within an hour of its application, if any error is made; an admirable feature when coating valuable conversion crystals.

Blast-shield coatings have different requirements. First, they are applied by a meniscus coating process on large (6- by 2-foot) pieces of relatively cheap float glass. Secondly, the first (base) coat must be insoluble within 10 to 15 minutes, so that the second coat can be applied without any delay, or without having to remove the glass from its holder. For this application, we use 100% TEOS hydrolyzed in water at pH 2 with ethanol as the solvent. The two-layer coatings perform well over a broad spectrum (from 400 nm to 1000 nm) at incident angles of up to 60°. They have also survived 10,000 shots in the NIF prototype flashlamp chamber without any substantial degradation of their optical performance.

Effects of the Use Environment on Sol Coating Performance

Unfortunately, highly porous coatings have high specific surface areas and are therefore very susceptible to vapor

adsorption contamination from the use environment. Contamination of the AR coating decreases laser efficiency due to increases in reflectance and absorption; increased laser damage can also result. For instance, the increased reflected energy could produce laser damage if it focuses on another optic or on a laser-vessel wall to cause ablative contamination. Contamination-related damage has occurred on Nova,[4] OMEGA,[5] and Beamlet.[6] Guch and Hovis[7] and Hovis et al.,[8] also discuss organic contamination damage in lasers.

While contamination has caused increased maintenance and some minor damage on today's lasers, the problem might become more serious for future lasers designed to operate at fluences that are three to four times higher. This is especially true for the NIF laser, which has more motors, slides, and mechanisms near optics than previous lasers have had. Therefore, without improved technology, contamination effects could become quite serious.

Practical contamination effects can vary widely, according to the use environment. At the time of Beamlet's decommissioning, measurements were made on some of its laser optics to determine their reflectance and transmission characteristics. Table 3 shows clear differences between surfaces operating in vacuum vs those operating in atmospheric-pressure nitrogen. Table 3 also shows the beneficial effect of the intermittent presence of a partial-oxygen plasma at the Pockels cell windows.

Even though surface adsorption is an equilibrium process, transport characteristics often influence observed contamination levels—for experimental time scales that are too short to establish a source/sol-coating equilibration. High-vacuum environments promote very rapid approaches to equilibria, due to the inverse pressure dependence of gas diffusivity. Conversely, the slow transport rates of heavy adsorptives at atmospheric pressure can slow the approach to equilibrium to times of a month or more. Figure 4 shows the transmission loss of an optic over eight months of exposure to laboratory room air. The persistent downward trend in transmission indicates that equilibrium was not achieved, even after more than 200 days. Not surprisingly, intermediate contamination rates are observed at intermediate vacuum levels or when mass transfer is enhanced by forced convection at higher pressures.

Effects of Contamination on the Aggregate Refractive Index

As adsorbed contaminants displace air in the pores of the coating, the immediate effect is to increase the refractive index and hence, the optical thickness. The net effect on optical transmission (for either 1ω or 3ω) can easily be inferred from Figure 1 by moving along a line of constant physical thickness (in the corresponding contour plot) from the initial index to the index of the contaminated sol-coating mixture. The tolerance to a shift in the refractive index is approximately equal for 1ω and 3ω films, when their thicknesses are nearly optimal. However, when a 3ω

TABLE 3. The transmittances (%*T*) and reflectances (%*R*) of Beamlet's 1ω optics when it was shut down.

Optic	Time on line (months)	%*T*	%*R* (vacuum side)	%*R* (air side)
1ω vacuum window	0.25	99.20	0.7	0.1
SF4 lens	8	99.35	0.7	0.2
SF1 lens	12	98.00	1.9	0.1
Pockels cell (Window 1)	41	99.80	0.2	0.1
Pockels cell (Window 2)	41	99.80	0.2	0.05

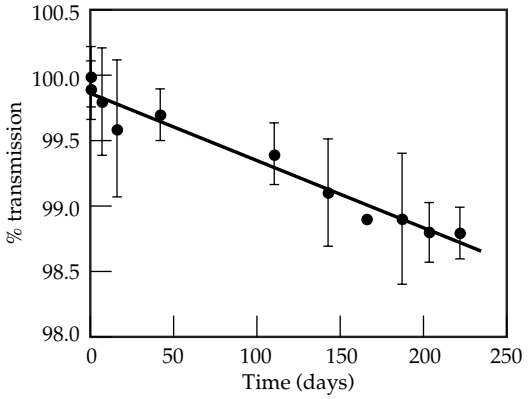

FIGURE 4. Transmission loss of sol-coated optic exposed to laboratory room air. (40-00-0299-0386pb01)

coating varies from its optimum thickness by only ±5 nm, the sensitivity of the reflectance to index variation increases significantly. It is interesting to note that if the film's initial refractive index was below its optimal value, its transmission can actually improve with contamination—even to the point of reaching its optimal index.

In practice, the amount of relatively heavy organic compounds adsorbed (from exposures to environmental contaminants) can be related to changes in a sample optic's transmission. The measured change in transmission is interpreted as being the product of changes in the two single-surface transmissions. Each single-surface transmission change is modeled by calculating Fresnel coefficients[9] in the usual way, using the shift in the film's refractive index away from its initial value. The volume fraction of adsorbed contaminant can then be estimated from the composite refractive index, using an effective media approximation (EMA) for the composite dielectric function of the film (such as the Bruggeman[10] EMA).

Postdeposition Treatment of Sol Films

Because it is not always possible to select engineering materials with negligible outgassing properties, or to bake them out before using them, it is highly desirable to reduce the tendency of the sol-gel coatings to adsorb organic contaminants. For fused-silica optics, chemically treating the sol-coated surface can decrease its affinity for atmospheric contaminants. However, the effects of the chosen treatment must not alter the refractive index or the thickness of the final coating beyond the acceptable ranges shown in Figure 1. We have demonstrated an acceptable treatment program offering some improvement in adsorption properties in all cases that we have tested so far.

Adsorption characteristics are related to both the microporosity and surface polarity of the silica. Therefore, it is potentially beneficial to decrease the surface area and replace polar surface groups with nonpolar ones. This can be accomplished in two steps.

The first step is to expose a coated surface to ammonia (NH_3) and water vapor at room temperature. This hydrolyzes residual ethoxyl groups on the silica particles to hydroxyl groups and catalyzes the condensation of many hydroxyl groups to siloxane linkages. The condensation reaction cross-links and binds together adjacent silica particles, thereby increasing the coating's abrasion resistance and adhesion strength. This hardening effect was first reported by Floch and Belleville[11] and has been adapted for use on the Phebus fusion laser in France.

The second step is to expose the coating to hexamethyldisilazane (HMDS) vapor, also at room temperature. The HMDS converts the remaining hydroxyl groups to trimethylsiloxy groups. After eliminating these polar groups, the surface is almost entirely covered by nonpolar trimethylsilyl groups. Further details of this treatment process can be found in Thomas.[12]

Table 4 shows some of the progressive changes in physical and optical properties of the sol coating after each treatment step. All of the initial, intermediate, and final refractive indices are well within the optimal ranges shown in Figure 1. The range of porosity (void fraction) for these films is between 0.48 and 0.54, almost 50% higher than the theoretical void fraction for lattices of close-packed spheres. The shift in physical thickness is primarily associated with the ammonia-vapor treatment step and the downward trend in porosity indicates a corresponding increase in packing density. The

amount of shrinkage is quite significant and will shift an initially optimum coating well outside the desired optical thickness range. Consequently, these postdeposition treatments require the initial film-thickness to be corrected upward to compensate for the inevitable shrinkage. The shrinkage, while sensitive to the film's thickness, has been repeatable in all the tests that we have done. Therefore, the correct adjustments to the deposition parameters are easily made.

Naturally, the effects of these chemical treatments on the specific surface area (m^2/g) and porosity characteristics of the final film are of interest, particularly with respect to surface adsorption behavior. Figures 5 and 6 show isothermal nitrogen adsorption plots (obtained by the surface-acoustic-wave[13] method) for both as-deposited and ammonia-treated films. The resulting adsorption isotherm shapes are classified as type IV.[14] This may loosely be taken to mean that there is an inflection point in the low relative pressure region, $0.05 < p/pv < 0.4$, while in the higher relative pressure region the capillary condensation mechanism dominates—indicating considerable mesoporosity within the film.

Adsorption behavior over a limited pressure range often agrees fairly well with simple adsorption theories, such as those put forward by Brunauer, Emmett, and Teller[15] (BET), or by Langmuir.[16] For the porous surface, conformity to BET or to (the simpler) Langmuir behavior can be tested and exploited to derive the specific surface area and an adsorption equilibrium constant. Table 5 summarizes BET- and Langmuir-derived characteristics for various porous silica preparations. The high relative pressure, capillary-condensation region can be analyzed to yield an approximate pore-size distribution.

Table 5 also shows the results of this calculation as done according to the BJH[17] method. This reveals an upward shift in pore size distribution and the appearance of some porosity in the 1- to 2-nm range as a result of the ammonia treatment step. Adsorption data for HMDS-treated films were not available, so data for bulk sol samples are given, to show the relatively small change in surface area and porosity characteristics that are associated with this surface-treatment step. BJH calculations done for the HMDS step on the bulk samples indicate an upward shift in pore-size distribution and the appearance of small pores in a fashion similar to that in the film samples.

If the silica particles were just simple hard spheres, the decrease in surface area that is associated with the vapor treatments is inconsistent with a decrease in film thickness. With the packing pattern of the silica particles being roughly equivalent to that of

TABLE 4. The effects of treating a film with respect to its refractive index and thickness. (The average effect on seven samples, as measured by ellipsometry.)

	Refractive-index data					Film-thickness data				
	As deposited sol index	After NH_3 hardening	After HMDS treatment	Change in sol index from as deposited to HMDS treated		As deposited	After NH_3 hardening	After HMDS treatment	Change in film thickness from as deposited to HMDS treated	
Film	n_0 (f_{void})	n_{NH_3} (f_{void})	n_{HMDS} (f_{void})	Δn	Change (%)	d_0 (nm)	d_{NH_3} (nm)	d_{HMDS} (nm)	Δd (nm)	Change %
1ω	1.198 (0.528)	1.210 (0.502)	1.218 (0.484)	0.020	1.6	224.8	195.4	195.2	29.6	13.16
3ω	1.192 (0.541)	1.211 (0.499)	1.221 (0.477)	0.029	2.5	70.4	59.7	59.3	11.1	15.82

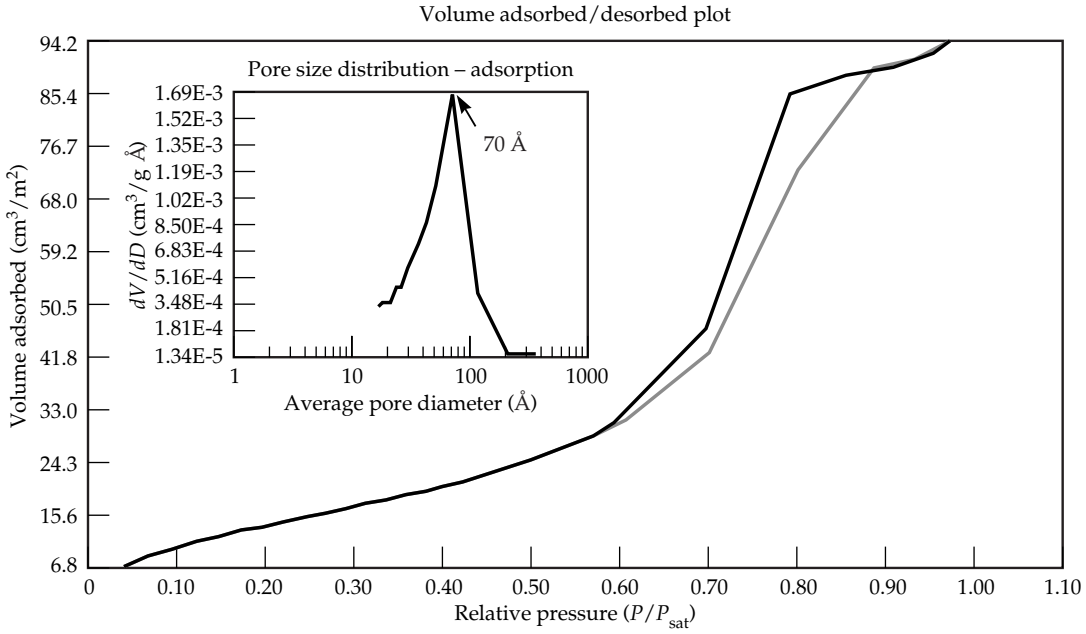

FIGURE 5. N adsorption isotherm for untreated sol film. (40-00-0299-0387pb01)

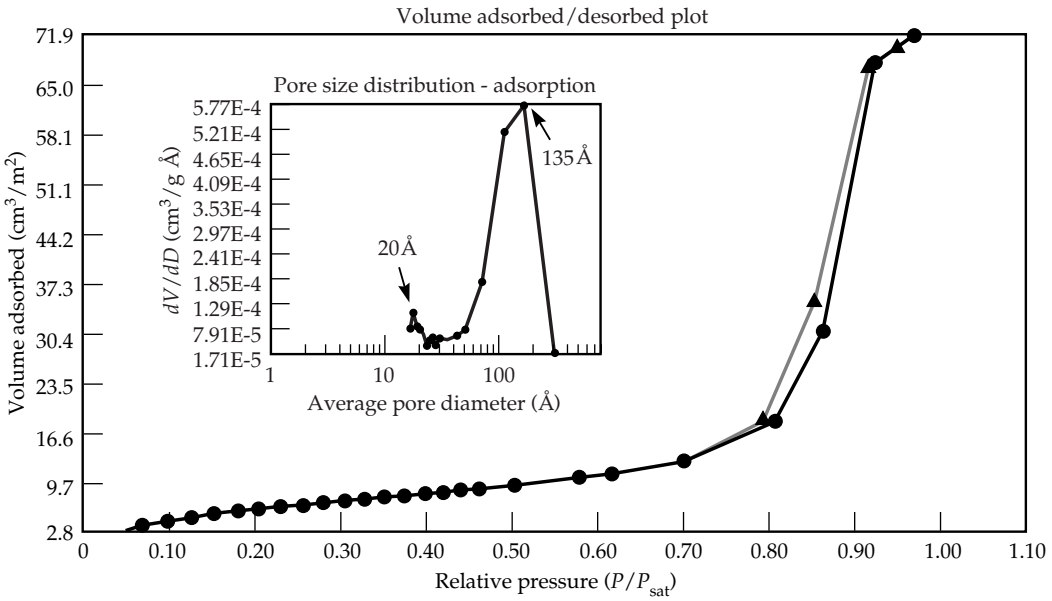

FIGURE 6. N adsorption isotherm for NH_3 treated sol film. (40-00-0299-0388pb01)

a simple cubic lattice (consistent with a porous fraction of about 0.48), the observed film shrinkage should lead to a corresponding decrease in average particle diameter of about 20%. If a change in particle size were the only effect, the specific surface area should *increase* by approximately 30% as a result of the NH_3 vapor treatment. The observed *decrease* in specific area therefore indicates that the silica particles are not smooth spheres, but rather must contain a significant amount of surface roughness and/or internal "microporosity." This interpretation is consistent with previous sol-particle morphology studies done by direct transmission electron microscopy (TEM) imaging.[18]

The equilibrium constants (C-factors), included in Table 5, are indications of the surface affinity for the particular adsorptive.

TABLE 5. A summary of BET and Langmuir calculations derived from nitrogen isotherm data. (L) = Langmuir; all others, BET.

Sample	Specific area (m^2/g)	Pore peaks (Å)
As-deposited film	174	70
NH_3-treated film	76	135 and 20
Evaporated bulk sol	564	55
NH_3-treated bulk	238 (L)	100 (L)
NH_3 + HMDS-treated bulk	215	150 and 20

They are included only to help quantify the characteristic shape of the isotherm. Although using nitrogen as a probe is convenient for surface area and porosity determinations, it yields no specific information about the chemical characteristics of the surface with respect to organic contamination.

Because a key characteristic of sol-gel derived AR coatings is a relatively high laser-damage threshold, it is crucial that any postdeposition treatment process not degrade this essential property. We have compared laser damage thresholds at the primary NIF wavelengths for fused silica coated with as-deposited and ammonia/HMDS-treated films. There appears to be no significant difference in laser damage thresholds between fused silica coated with treated or untreated films.

As a full-scale demonstration of the treatment process, a Nova spatial filter input lens was coated to an initially thicker than normal specification and then treated by the general methods previously described. A second lens was coated to the normal specification to act as a control. Both lenses were installed in Nova beam lines and will be evaluated after about five months of service when the Nova laser is decommissioned in mid-1999. As Table 6 shows, within the normal photometer error of ±0.1%, both lenses have identical transmission and reflection properties at their 1053-nm use wavelength.

TABLE 6. Nova SF-7 1064-nm transmission and reflection (NH_3 + HMDS treated vs untreated).

	$\%R_{input}$	σ_{input} %	$\%R_{output}$	σ_{output}	$\%T$	$\sigma\%T$
Untreated lens	0.01	0.01	0.01	0.01	99.83	0.09
NH_3 and HMDS-treated lens	0.06	0.01	0.07	0.03	99.78	0.08

Sensitivity of Sol-Gel Coatings to Organic Vapors

The contamination resistance of the coatings was tested under three different sets of temperature and pressure conditions. Room-temperature atmospheric tests with forced convection simulated realistic operating conditions for some of the laser optics. Room temperature high-vacuum tests were used to simulate operation in the NIF spatial filters and target chamber. High-temperature atmospheric pressure tests increased contaminant vapor pressures by several orders of magnitude and enhanced gaseous diffusion. In all cases, the presence of real engineering materials ensured a realistic sampling of organic contaminants.

The standard analytical technique was to measure the total transmission at a fixed wavelength, which (as noted earlier) is a sensitive indicator of any refractive index change in the optical coating. Therefore, a spectral transmission measurement of the optic before and after being exposed to contaminants is sufficient to determine the extent of contaminant adsorption within the film.

Treated and untreated samples were similarly exposed in separate tests to silicone-, butyl-, and EPDM-rubber samples. As Table 7 shows, at 560-nm the untreated samples lost 1.2%, 0.5%, and 1.0% of their transmittance. The ammonia-hardened coating lost 0.2% transmittance for the silicone rubber, but all other changes were 0.1%, or less. Another test explored the importance of contaminant polarity by

exposing the three coating types to Fomblin oil vapor, a perfluorinated polypropylene. The transmittance losses were 3%, 1.5%, and 0.5%, respectively, for the conventional, ammonia-hardened, and HMDS-treated optics. While there is still a significant advantage to the treatments in reducing adsorption of hydrophobic materials, it is less than for more polar compounds.

Table 7 also reports the volume fraction of adsorbed organic material calculated with the Bruggeman EMA and an assumed contaminant refractive index of 1.51. These calculations indicate that the observed improvement in contamination resistance is approximately proportional to the reduction in available surface area. Local compaction of the film might also effectively shield some portion of the total porosity from penetration by large contaminant molecules due to physical exclusion (a molecular sieve effect). Most BJH calculations, using adsorption data from ammonia-hardened films, show that some porosity from the treatment will appear in the one- to two-nanometer range. Any remaining changes in adsorption behavior are logically associated with surface-chemistry effects.

A contaminated optic can usually recover its full transmittance by spray-washing it with ethyl alcohol or methylene chloride. If the contaminant source is an engineering material, analysis of the wash by gas chromatography–mass spectroscopy usually shows the presence of compounds logically found in the material, such as silicone oils in silicone materials, caprolactam in nylon, and plasticizers (especially dioctyl phthalate) in the vast majority of elastomeric components.

Similar vacuum outgassing experiments with conventional evaporative coated optics have indicated that organic adsorption is not limited to sol-gel coatings. Single-sided hard AR coatings lost, on average, only three times less transmittance than the double-sided sol-gel coatings.

It has been demonstrated that a bakeout of most engineering materials and mechanical components at 200°C removes offending compounds (most often plasticizers) fairly effectively. A 110°C bakeout removes contaminants in the C_{15} to C_{20} range (with vapor pressures of about one Torr at that temperature). However, a 200°C bakeout is needed to remove C_{30} contaminants, which have vapor pressures of about one Torr at the higher temperature. Of course, vacuum and time can achieve more effective removal at lower temperatures, but a detailed study of these parameters has not been done.

Degradation of the Optical Performance of Sol-Coated KDP

Figure 7 shows the transmittance degradation of the rapid-growth frequency doubling crystal, RG8B-2, which was used for the final Beamlet conversion and high-damage-threshold campaigns in the Beamlet vacuum mule. This optic is representative of the doubling and tripling crystals being operated in vacuum. Unlike the

TABLE 7. Changes in the transmission of treated and untreated optics, after being exposed to various contaminating environments.

Contaminant source	P (atm)	T (°C)	Untreated		NH_3-treated		NH_3+HMDS	
			$\Delta\%T$	f_{org}	$\Delta\%T$	f_{org}	$\Delta\%T$	f_{org}
Silcone rubber	1	110	1.20	0.19	0.20	0.08	<0,10	0.05
Butyl rubber	1	110	0.50	0.12	<0.10	0.05	<0.10	0.05
EPDM rubber	1	110	1.00	0.17	<0.10	0.05	<0.10	0.05
Fomblin oil	1	110	3.00	0.30	1.50	0.21	0.50	0.12
Prototype HEPA air system	1	30	0.35	0.11	0.21	0.08	0.07	0.04
Amp motor	10^{-9}	30	0.14	0.06	0.03	0.02	—	—
Conex fiber-optic cable	10^{-9}	29	0.75	0.15	0.13	0.07	—	—
Poron cellular urethane	10^{-9}	29	1.73	0.23	0.60	0.13	—	—
Fiber-optic splitter	10^{-9}	23	3.23	0.31	0.51	0.12	—	—

fused-silica optics presented in Table 1, the decrease in KDP/DKDP transmittance is not accompanied by a commensurate increase in reflectance, and the original transmittance is not regained when the optic is washed with a suitable solvent.

This transmittance loss is attributed to the formation of discrete etch-pits on the crystal surface under the porous sol coating. These pits, generally one- to two-microns wide and a few hundred nanometers deep, have characteristic geometries that depend on the crystal-surface's orientation. Figure 8 shows the diamond-shaped pits that are found on type I crystals, such as doubler RG8B-2. The type II crystals, used for third-harmonic generation on Beamlet, develop triangular pits. The Z-cut crystals, used for the Pockels switch, develop square etch pits. The etch pits on the Beamlet's tripling crystals elongated to become "slits" up to 40-microns in length, which cause wide-angle diffraction. This scatter loss dominated the crystal's performance, far outweighing any transmittance drop from organic contaminants adsorbed into the porous sol.

A loss of transmission, attributed to surface roughening of contaminated KDP surfaces in the presence of water vapor, was observed sporadically on Nova.[19] In the early '90s, we began using a 122-nm-thick thermal-cured silicone layer on all Nova crystal surfaces as an environmental, as well as an optical, coating.[2] However, no silicone coatings were used on the 37-cm Beamlet crystals—and it was recently discovered that the room-temperature cured silicone does not always prevent etch-pit growth. We are still in the early stages of defining and resolving this issue. Besides defining the contributions of coating- and finishing-process variables, residual contamination, and relative humidity to etch-pit initiation and growth, we plan to investigate ways to passivate the surface and minimize the water-vapor adsorption

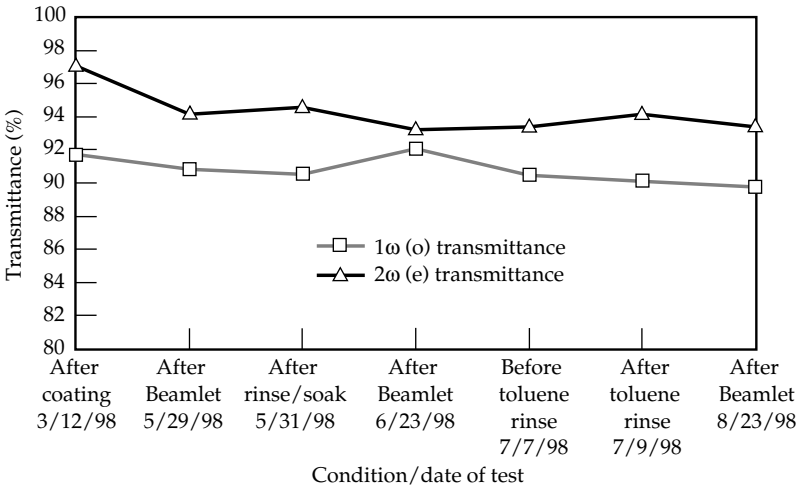

FIGURE 7. Transmittance loss over time for the Beamlet rapid-growth doubler crystal, RG8B-2. (40-00-0299-0389pb01)

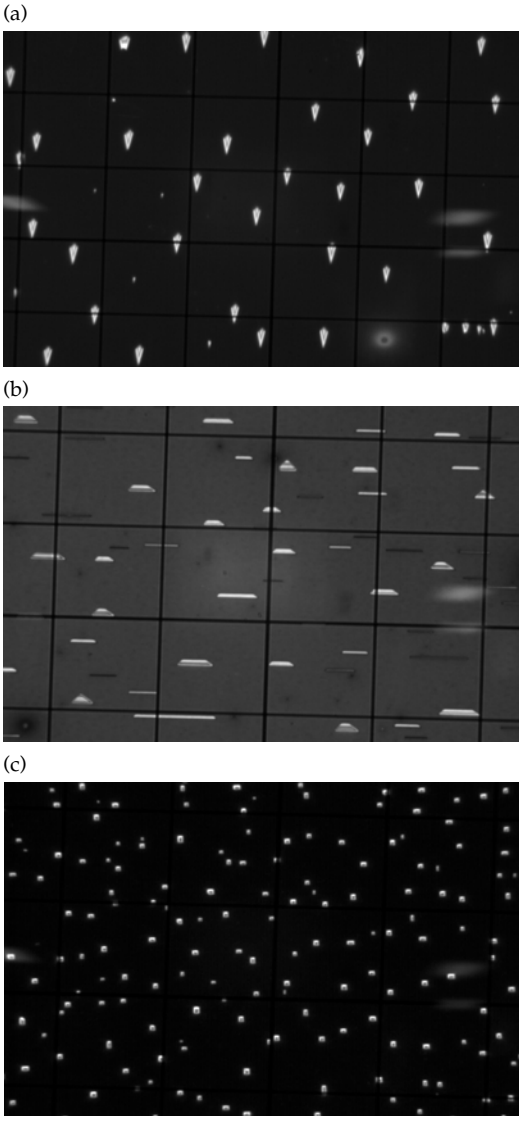

FIGURE 8. Etch pits formed under the AR coating on KDP and DKDP surfaces: (a) type I (doublers); (b) type II (triplers); (c) Z-cut (switch) crystals. (40-00-0299-0390pb01)

of the AR coating, either by treating or eliminating the porous sol.

The effect of volatile organic contamination on porous sol coatings for KDP crystals is expected to be similar to that observed for fused-silica optics. We attribute the lack of degradation of the vacuum surfaces of Beamlet's Pockels cell windows to a combination of the ammonia-hardened sol and a small oxygen bleed that is used in conjunction with the plasma to oxidize adsorbed organic contaminants. However, the ammonia vapor and HMDS vapor processes that have just been described are incompatible with KDP's surface chemistry. Instead, we expect that the oxygen/plasma cleaning will be sufficient to maintain the switch crystals' performance without modifying the sol coating. Furthermore, it is expected that a very clean, low-vacuum environment (at about 1 Torr) will suitably retard contamination degradation of the conversion crystals.

In addition, we are exploring alternate sol-preparation techniques, which allow us to exchange the native surface ethoxy and silanol groups with HMDS in an ethanol solution. The excess HMDS can then be evaporated, along with the ammonia catalyst, before the sol is applied to the crystal surfaces. Although this treatment will not benefit from the reduction in surface area inherent in the ammonia-hardening process, it is hoped that sensitivities to water and polar organic contaminants can be reduced. Other options (besides porous sol coatings) for reducing organic contamination sensitivity rely on eliminating porosity by using low-index, high-purity fluoropolymers developed for the photonics industry.[20, 21]

Conclusions

Antireflection coating designs and materials have been developed to meet NIF requirements for fused-silica and KDP-transmissive optics. Postdeposition chemical treatments, which reduce the surface area and polarity of sol-gel AR coatings, decrease the tendency of sol coatings to absorb organic contaminant vapors from the use environment. An added advantage of these treatments is the increase in abrasion resistance imparted to the sol coating. Intermediate-index materials, such as a room-temperature cured silicone, have been developed that allow broadband coatings to be applied to deuterated tripling crystals to allow optimal performance at two wavelengths. Substantial progress has been made toward a spin-coating capability, which will allow us to place an optimum-thickness coating on each surface of the conversion crystals. Efforts are currently shifting focus from manufacturing process development to developing methods to better control and minimize the interaction of these coatings with their use environments.

Acknowledgments

We gratefully acknowledge the measurements of optics contamination for various materials and mechanisms done by Tom McCarville, Mike Benapfl, John Ertel, Brian Kelly, and Dan Behne; the photometry measurements done by John Prior; and the Beamlet crystal processing and interferometry measurements done by Mary Norton, Mick Werve, and Will House.

Notes and References

1. I. M. Thomas, "High Damage Threshold Porous Silica Antireflective Coatings," *Appl. Opt.* **25**, 1481 (1986).
2. I. M. Thomas et al., "Processes for the Elimination of Fogging on KDP Crystals Prior to and During Use in Laser Systems," Boulder Damage Symposium, Boulder, Colo., October 23–25, 1991 (UCRL-JC-108273).
3. I. M. Thomas, "A Two Layer Broadband Antireflective Coating Prepared from a Methyl Silicone and Porous Silica," *Proc. of SPIE Sol-Gel Optics IV*, Vol. 3136, pp. 215–219 (1997).
4. P. G. Wegner, *1987 Laser Program Annual Report*, Lawrence Livermore National Laboratory Report UCRL-50021-87, pp. 3–16.
5. A. L. Rigatti and D. J. Smith, "Status of Optics on the OMEGA Laser After 18 Months of Operation," Laser-Induced Damage in Optical Materials: 1996, 28th Annual Boulder Damage Symposium, in *Proc. SPIE* (H. E. Bennett, et al., eds.) Vol. 2966, pp. 441–450 (1997).
6. J. H. Campbell et al., *Performance Results for BEAMLET: A Large-Aperture, Multipass Nd: Glass Laser*, Lawrence Livermore National Laboratory, Livermore, CA, UCRL-120799 (1995).
7. S. Guch, Jr. and F. E. Hovis, "Beyond Perfection: the Need for Understanding Contamination Effects on Real-World Optics," Laser-Induced Damage in Optical Materials: 1993, 25th Annual Boulder Damage Symposium, in *Proc. SPIE* (H. E. Bennett, et al., eds.) Vol. 2114, pp. 505–511 (1994).

8. F. E. Hovis, B. A. Shepherd, C. T. Radcliffe, A. L. Bailey, and W. T. Boswell, "Optical Damage at the Part-per-Million Level: the Role of Trace Contamination in Laser-Induced Optical Damage," Laser-Induced Damage in Optical Materials: 1993, 25th Annual Boulder Damage Symposium, in *Proc. SPIE* (H. E. Bennett et al., eds.), Vol. 2114, pp. 145–153 (1994).
9. R. M. Azzam and N. M. Bashara, *Ellipsometry and Polarized Light* (North Holland, 1977), p. 286.
10. D. A. G. Bruggeman, *Ann. Phys.*, **4**(24) (1935).
11. P. F. Belleville and H. G. Floch, "Ammonia Hardening of Porous Silica Anti-reflective Coatings," Sol-Gel Optics III, in *Proc. SPIE* (J. D. MacKenzie, ed.), Volume 2288, pp. 25–32 (1994).
12. I. M. Thomas, A. K. Burnham, J. R. Ertel, and S. C. Frieders, "Method for Reducing the Effect of Environmental Contamination of Sol-gel Optical Coatings," Lawrence Livermore National Laboratory, Livermore, CA, UCRL-LR-129705. Prepared for Solid State Lasers for Application to Inertial Confinement Fusion Conference (June 7–12, 1998), UCRL-JC-129705.
13. G. C. Frye and S. J. Martin, *Applied Spectroscopy Reviews*, **26**(1,2), 73–149 (1991).
14. S. J. Gregg and K. S. W. Sing, "Adsorption, Surface Area and Porosity," Academic Press, New York, 1982.
15. S. Brunauer, P. H. Emmett, and E. Teller, *J. Am. Chem. Soc.* **60**, 309 (1938).
16. I. Langmuir, *J. Amer. Chem. Soc.* **38**, 2221 (1916).
17. E. P. Barrett, L. G. Joyner, and P. P. Halenda, *J. Amer. Chem. Soc.* **73**, 373 (Jan. 1951).
18. A. van Blaaderen and A. P. L. M. Kentgens, *Journal of Non-Crystalline Solids* **149**(1992), 161–178 (1992).
19. M. R. Kozlowski et al., "Influence of Diamond Turning and Surface Cleaning Processes on the Degradation of KDP Crystal Surfaces," Lawrence Livermore National Laboratory, Livermore, CA, UCRL-JC-105835. Prepared for SPIE International Symposium, July 21–26, 1991.
20. I. M. Thomas and J. H. Campbell, "A Novel Perfluorinated AR and Protective Coating for KDP and Other Optical Materials," Boulder Damage Symposium, Boulder, CO, Oct. 24–26, 1990.
21. S. Papernov et al., "Laser-Induced Damage in Optical Materials," in *Proc. SPIE* **1624**, 314–318 (1991).

Developing Optics Finishing Technologies for the National Ignition Facility

T. G. Parham *C. Stolz*

T. Baisden *M. Kozlowski*

C. Kiikka *D. M. Aikens*

The National Ignition Facility (NIF), which will house a 192-beam laser system capable of generating two million joules of ultraviolet light, is being constructed at Lawrence Livermore National Laboratory (LLNL). To build this laser system, LLNL's industrial partners must produce more than 7500 meter-class optics. Their large precision-optics manufacturing facilities began producing the optics in 1998 and will finish their production by 2003.

In 1994, a series of cost studies made it clear that in order to fabricate (at the lowest possible cost) this unprecedented number of large precision optics in so little time, new technologies would have to be developed and new factories, based on them, would have to be constructed.[1] At that time, working with three suppliers of large optics, LLNL began three-year-long optics-finishing programs to develop these technologies. Although each development program centered on the specialties and often proprietary technologies already existing at the suppliers' facilities, many technologies for the low-cost manufacturing of these optics were common to two, or sometimes all three, of these programs.

Because many advances in these programs stem from the vendors' intellectual property and trade secrets, they cannot be completely described in a public forum. Nevertheless, many nonproprietary advances have been made and are now being used by the companies under contract: Eastman Kodak, SVG-Tinsley Division (formerly Tinsley Laboratories and referred to hereafter as Tinsley), and Zygo. The nonproprietary, optics-fabrication, developmental highlights for the manufacturing steps of shaping, grinding, polishing, figuring, and metrology are discussed[2] in a general sense in this article.

The NIF Optics Finishing Development Plan

The developmental effort in optics-fabrication technology was divided into three parts:

- A small internal LLNL effort (optics finishing R&D, wavefront analysis, and specifications).
- Three fabrication-development subcontracts for flats.
- Two fabrication-development subcontracts for aspheric lenses.

All vendor subcontracts were initiated by competitive solicitation. The three companies selected worked closely with LLNL to advance the technologies most critical to their own manufacturing processes. In most cases, successful subscale experiments were followed by full-scale experiments on production equipment. Table 1 lists the funded activities.

TABLE 1. Funded development activities.

Technology	LLNL	Vendors
Fixed-abrasive grinding	None	Hybrid-tool grinding; ELID dressing
Table lapping/loose-abrasive grinding	Double-sided lapping	High-speed, pellet-lap grinding
Polish out	High-pressure polishing; thernal figure control	High-speed polishing; variable-pressure polishing; synthetic-lap polishing
Deterministic figuring	None	Reduced-ripple, small-tool polishing: deterministic planetary polishing; ion-beam figuring; variable-pressure polishing
Metrology	PSD-based, wavefront specifications	Various
Other tools/processes	Cladding and cleaning specifications; automated cleaning	Optic handling; improved tooling; cladding technology
Laser-damage-performance improvements	Grinding-material selection; slurry; optimization; subsurface damage minimization; inspection-tool development	Slurry optimization; subsurface damage minimization

Overall, the program was highly successful; each vendor demonstrated a process that would satisfy all (or nearly all) of the NIF's performance requirements, at a fraction of the pre-NIF cost. The facilities construction has been completed, or is nearly complete, at all three vendors. They will yield about a ten-times-higher capacity for large precision optics than their previously existing facilities based on earlier technologies—and at prices that are roughly one-third the cost of equivalent Beamlet optics.

Shaping, Grinding, and Polishing

Although substantially more than half the fabrication cost of a precision optic accrues during the final figuring and metrology steps, the easiest way to reduce these costs is often before polishing—by improving the part's surface quality, smoothness, figure, and reducing the amount of subsurface damage. Consequently, about half of the development projects were in the areas of shaping, surface grinding, and the polish out of the optical surfaces to remove diffuse scatter before the first in-process optical test.

The first step in producing a NIF optical component is "shaping." Many detailed variations on this process step exist, but the goals are all the same:

- Complete the outside dimensions to the specified length and width dimensions and tolerances.
- Produce an edge finish that can be precision cleaned (a rms surface microroughness of 0.2 μm).
- Generate the precision optical surfaces.

Optical surface-shape (or figure) control is critical. This is especially true during the early process steps, as most of the material is removed at this stage. Therefore, the ability to correct surface shape or orientation, relative to other optical surfaces, decreases as the optic is processed. Furthermore, if the optical surface shape is not maintained throughout processing, the depth of material removal at subsequent process steps will not be uniform. Residual subsurface damage could then reduce laser-damage thresholds in the areas of lesser material removal.

In the past, a two-part grinding process was used: a fixed-abrasive grinding step for coarsely shaping the optic to remove a

UCRL-LR-105821-99-2

large amount of material and a second step of loose abrasive grinding that is done in several stages, each with a smaller grit size and less material removed.

The NIF development vendors have adapted commercial computer numerical controlled (CNC) mills to shape the outside edges of the parts. One example is a hybrid rotary tool (Figure 1) developed by Tinsley for use on their CNC mill, which eliminates the need for loose abrasive grinding to the final surface roughness. It features two surface-generating areas on the tool, each with a different abrasive size. This allows removing large amounts of material in a single pass, with good surface figure control, while simultaneously producing a smooth, finished surface. Internal cooling channels are used to rapidly remove the heat being generated. Edging tests demonstrated removal rates consistent with optics production from saw-cut blanks using a single CNC edging machine. Their new machine now allows them to produce NIF lenses and windows for a lower overall cost, since lower-cost blanks with saw-cut surfaces can now be purchased, instead of blanks with finely ground surfaces.

Zygo is using a recent advance in fixed abrasive grinding, a technique called Electrolytic In-process Dressing (ELID), to produce smoother optical surfaces with fewer process steps. Typically, flat or spherical optical surfaces are generated using a coarse, bound abrasive wheel—followed by successively finer, loose-abrasive grinds. Published reports on the ELID technique indicated that near-specular finishes could be obtained from a fine, bound, abrasive over small apertures.[3] This work indicated the existence of a technology that might be applicable to large optics to eliminate at least one loose-abrasive grinding step, or possibly more.

FIGURE 1. The hybrid grinding/shaping tool developed by Tinsley to improve the efficiency of initial blank shaping. (40-00-0499-0806pb01)

The major restriction of conventional fixed-abrasive grinding has been an inability to effectively use grinding wheels with small diamond grit without having to constantly dress the wheel. This must be done to expose fresh sharp diamonds and remove the buildup of "swarf," or ground glass, which binds between the exposed diamonds on the surface of the matrix.

The ELID process uses an electric current to enhance the surface oxidation of a conductive matrix holding the diamonds. This oxidation erodes the matrix, which prevents the build up of swarf and exposes fresh sharp diamonds, as illustrated in Figure 2. Therefore, as the wheel cuts the optic surface, it is also self-dressing and maintaining a good grinding surface. Since they are self-dressing, the ELID grinding-wheels' wear rate is significantly lower than that of conventional fixed-abrasive wheels, which require very aggressive dressing to remove swarf, expose fresh diamonds, and return their cutting surfaces to a nominally plano figure.

Small-scale development results for this technology, as applied to phosphate-based laser glass, are illustrated in Table 2.[4,5] Analysis of these data shows an improvement in material removal, a reduction in machine hours, and less wheel wear with the ELID technique. In addition, the resulting surfaces all had sufficiently good finishes to go directly to the polishing step. As this is being written, a large-scale demonstration of this technology is under way on equipment that will be used to manufacture large optics for NIF.

For a high-speed polish out, Tinsley developed a computer-controlled, high-speed grinder/polisher to rapidly lap (fine grind) lenses and flats and then

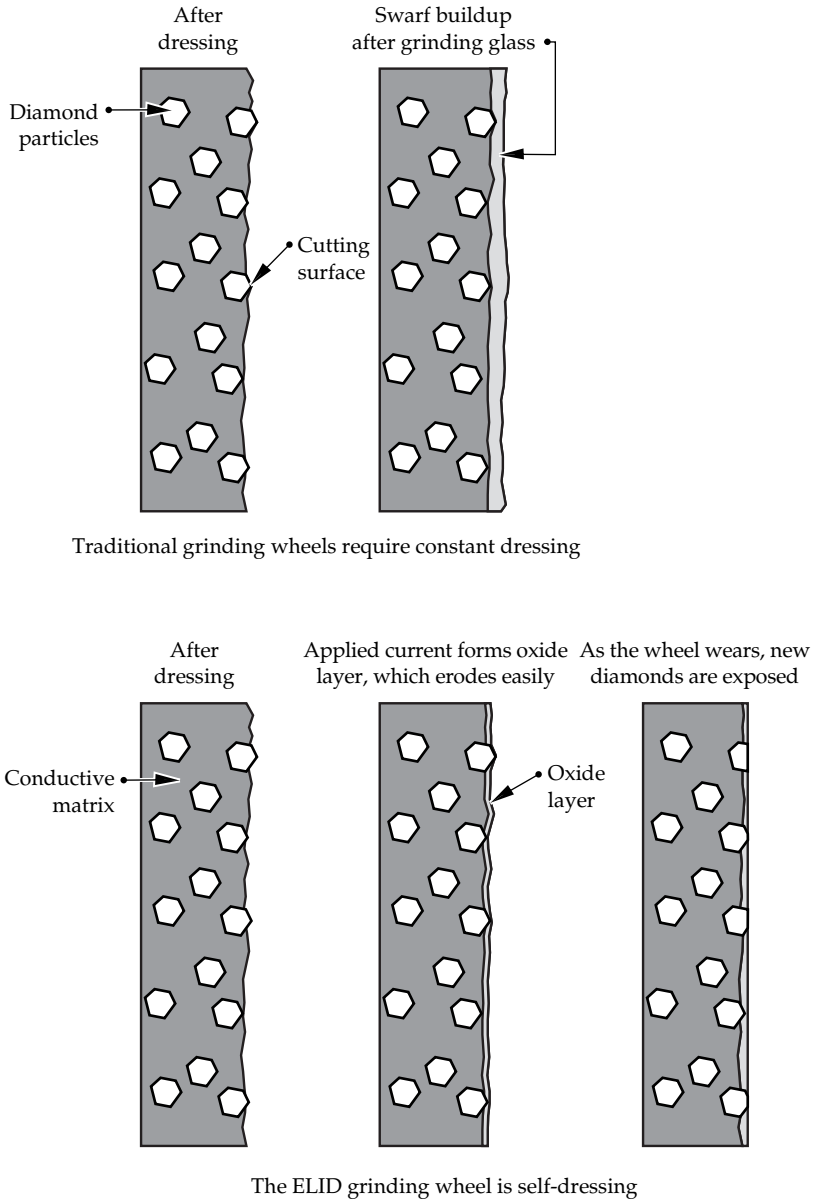

FIGURE 2. A comparison of traditional and ELID grinding. (40-00-0499-0807pb01)

TABLE 2. Summary of ELID vs conventional grinding performance data (time in hours).

Test condition	Coarse and fine generation time	Grinding time	Polish out time	Wheel wear rate (μm/hr)
ELID grinding	0.46 ± 0.04	0.66 ± 0.03	4.83 ± 0.69	11.0
Conventional grinding	0.17 ± 0.00	3.24 ± 0.47	5.67 ± 0.47	47.1

polish them out (Figure 3). An advanced version of the overarm spindle machines commonly used in lens production, its advanced features include automated control of the part and tool speeds, and of the pressure between the tool and optic. The high-speed lapping tool is an array of bound abrasive pellets attached to a backing plate, which is matched to the shape of the surface being finished. The machine and process are now optimized to remove 500 µm of material from the surface of a typical 440-mm-square optic to a 9-µm finish, in about two hours.

By replacing this lapping tool with a similar tool covered with a synthetic lap material, the same machine can also be used for high-speed polishing. During a high-speed polish out of the same part, an additional 36-µm-thick, fused-silica layer can be removed in three to four hours.

Deterministic Figuring and Precision Polishing

All three vendors investigated methods of figure control using advanced, highly deterministic processes and modern optical metrology tools and control systems. Figure control for large optics is generally accomplished in one of two ways: precision planetary polishing or computer-controlled, small-tool polishing.

The primary impediments to the planetary polishing of large precision plano-optics are the high capitalization costs for large planetary polishers and the frequently encountered lack of determinism associated with this technology. Both Zygo and Kodak were very successful with combinations of machine improvements, new diagnostics, and metrology—not only in adding determinism to their planetary polishing processes, but also in obtaining projected throughput increases of three to six times and lowering costs for their planetary polishers (Figure 4).

The shape of the pitch-polishing lap has a significant impact on an optic's final figure. At Zygo, a computer algorithm was devised that maintains a lap's flatness to within λ/20-wave, peak-to-valley, as measured on a 10-inch glass monitoring plate. Previously, without the intervention of a highly skilled optician, lap flatness diverged up to λ/3 wave, peak-to-valley,

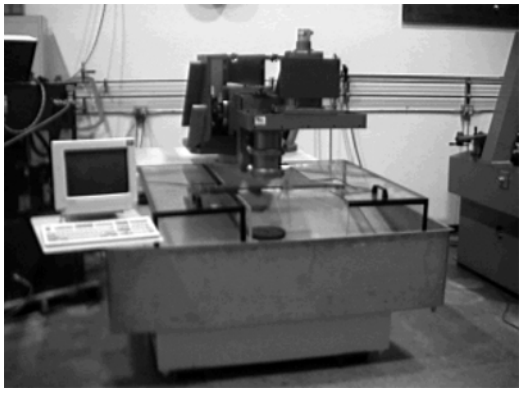

FIGURE 3. The high-speed lapper/polisher developed by Tinsley for a high-speed polish out of diffuse scattering ("gray") using pellet grinding. (40-00-0499-0808pb01)

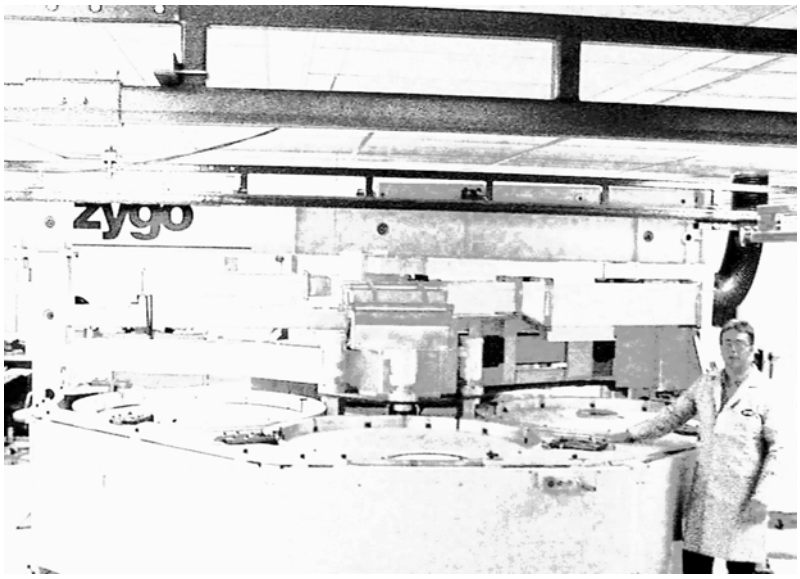

FIGURE 4. The 168-in. continuous planetary polisher used for the deterministic figuring of large NIF flats. (40-00-0499-0809pb01)

from a flat surface over the same 50-hour interval—as illustrated in Figure 5. This work has resulted in a computer-controlled, pitch-polishing lap that maintains a desirable figure, thus freeing the operator to concentrate on other tasks.

In the past, inherent wavefront ripple has limited the performance of optics fabricated by subaperture figuring, such as that done with a small-tool polisher. Ripple refers to periodic residual errors with a magnitude of 1 to 6 nm (λ/600 to λ/100) for spatial scalelengths of from 0.1 to 30 mm. In high-power laser applications, wavefront ripple causes dispersion that leads to near-field beam-intensity modulation. Wavefront ripple with spatial periods from 2 to 10 mm are nonlinearly amplified, which can result in laser damage and interference with beam propagation.[6,7]

In an effort funded by LLNL, Eastman Kodak developed a process using a computer-controlled, small-tool polisher (Figure 6), by which large (flat, spherical, or aspheric) optics can be polished "ripple-free." Kodak's process developments resulted from advances in metrology, which were combined with Fourier analysis and extensive finishing-process modeling.

Specifically, Kodak developed an algorithm for assessing mid-spatial-frequency errors from phase measuring interferometry data, which employs Fourier analysis to identify the signature frequencies and orientations of the periodic errors. Then, by modeling the motion of various mechanical and electronic parameters across the aperture, they are able to match—and then reduce or eliminate—the source terms giving rise to the signature frequencies.

Figure 7 compares a typical subaperture wavefront with mid-spatial-frequency ripple, from a laser-amplifier slab—after conventional small-tool polishing (a)—to a similar wavefront produced from a sample polished using Kodak's new small-tool polisher process (b). Using these data, the 1D plots of the power-spectral-density (PSD) analysis for the respective parts are compared in Figure 8. For reference, the line shown in each plot represents the PSD specification as a function of reciprocal mm (mm^{-1}) for the NIF laser. Figure 8 shows that Kodak significantly reduced

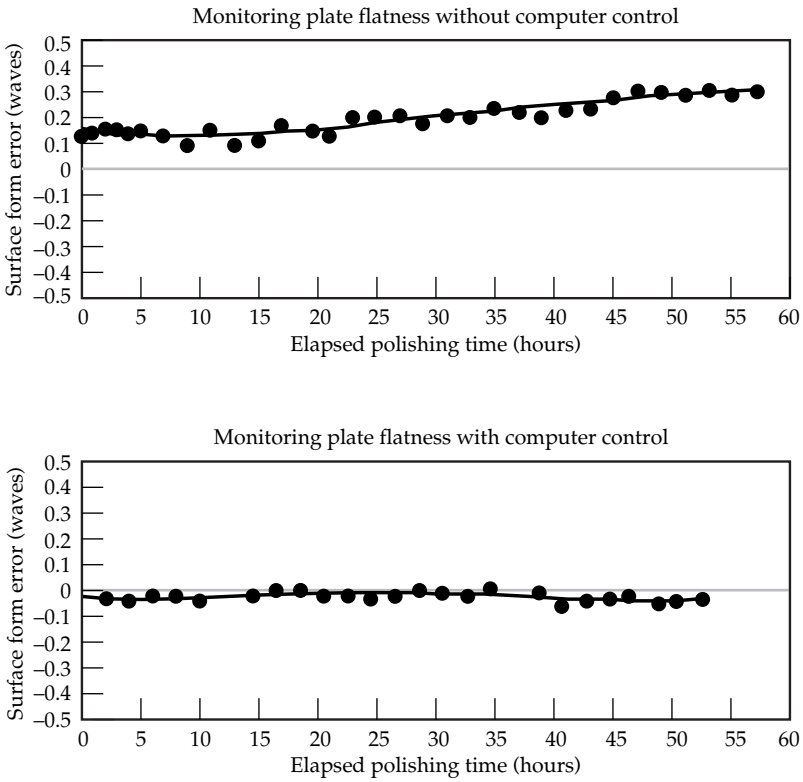

FIGURE 5. Without computer control or highly skilled operator intervention, the surface developed by a polishing lap diverges from flatness. (40-00-0499-0810pb01)

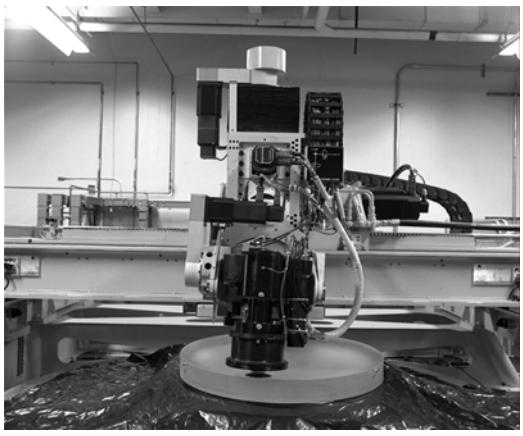

FIGURE 6. Kodak's small-tool machine. (40-00-0499-0811pb01)

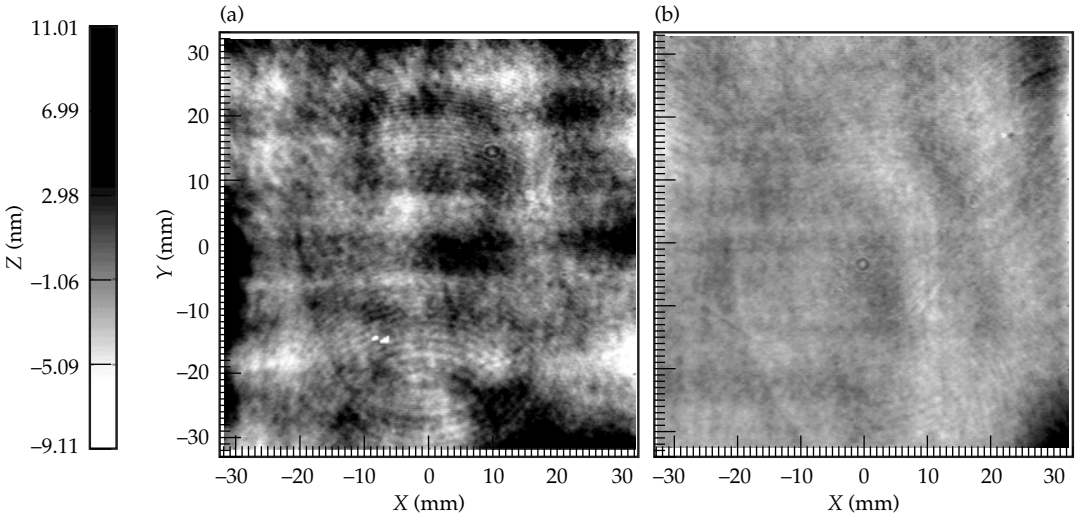

FIGURE 7. (a) The transmitted wavefront from a Beamlet amplifier slab with significant small-tool ripple. Note the grid-like striations with ~10-mm spacing across the part. (b) Process improvements made by Kodak have significantly reduced variations in the transmitted wavefront from this slab. (40-00-0499-0812pb01)

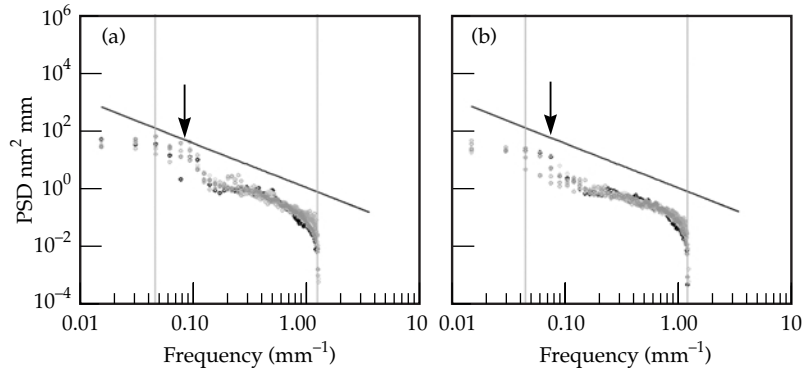

FIGURE 8. A 1D power-spectral-density (PSD) analysis of the two slabs described in Figure 7. The earlier Beamlet slab (a) has a spatial-scale ripple amplitude (at ~12 mm) that is 10 times higher than that of (b). (40-00-0499-0813pb01)

the periodic ripple errors by an order of magnitude in PSD amplitude, while figuring a 0.9-m optic to better than λ/6 peak-to-valley flatness.

This "ripple-free," computer-controlled, small-tool polishing process capitalizes on the advantages of other small-tool processes (in terms of high convergence and cost effectiveness), while also achieving a precision of figure and ripple control similar to that of the continuous-polishing process. For large-flat optics fabrication, significant cost savings in labor and capital investment result, compared to conventional flat-polishing techniques.

Tinsley has developed another small-tool technology, with similar capabilities, for figuring and polishing large flat, spherical, or aspheric optics. Their early efforts to apply small-tool figuring to lenses suffered from ripple in the 6- to 12-mm spatial regime, as can be seen from the PSD of a Beamlet lens, shown in Figure 9a. LLNL funded work at Tinsley to reduce ripple power, with results similar to those demonstrated by Kodak on amplifier slabs. Ripple was reduced through proprietary process changes in machine precision, dwell times, by adding randomness, and by eliminating periodic-error functions. The improvement is apparent in Figure 9b, which shows the PSD for a NIF SF1/2 cavity spatial-filter lens fabricated at Tinsley in late 1998. This is just one of several Tinsley-fabricated NIF first-bundle lenses that meet all NIF

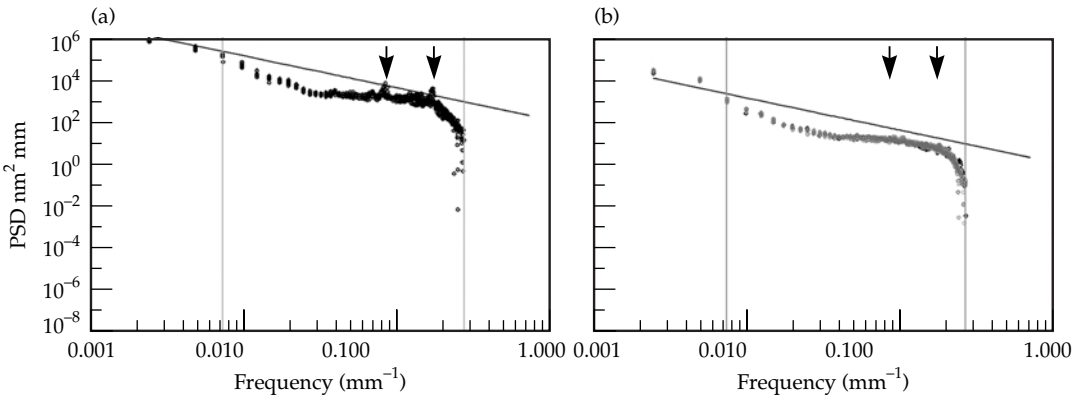

FIGURE 9. Comparison of power spectral density curves for (a) a Beamlet diagnostic lens with small-tool ripple vs (b) a NIF SF1/2 cavity spatial filter lens, where ripple was reduced to meet NIF specifications for PSD-I over spatial periods of from 33 mm to 2.5 mm.
(40-00-0499-0814pb01)

specifications. High-resolution, reflected-wavefront measurements were made with a microinterferometer (Figure 10a) to evaluate the PSD-II (waviness-2) spatial periods (between 2.5 and 0.12 mm) and the NIF PSD-III roughness specification (over spatial periods > 0.12 mm), as shown in Figure 10b.

Compensating for Material Inhomogeneities

Total system cost minimization has always been one of the primary goals of LLNL's optics-development efforts. One opportunity for cost minimization is the relation between material inhomogeneities and finishing processes. In the past, the fused-silica inhomogeneity specification for lenses and windows on large laser systems (such as for Nova and Beamlet) has been at two parts per million—the highest quality material that could reasonably be purchased from Corning or Heraeus in large quantities for the apertures of interest. The inhomogeneity is $\Delta n = e\lambda/t$, where e is the error in fractions of a wavelength, λ is the measurement wavelength, and t is the thickness of the part along the path traveled by the light. When measured at 633 nm, two parts per million translates into a transmitted wavefront error of ~$\lambda/7$ for a 46-mm-thick NIF spatial-filter lens. Thus, at an inhomogeneity of 2 ppm, the material consumes about 45% of the transmitted wavefront specification of $\lambda/3$ for NIF spatial filter lenses. This leaves 55% of the transmitted-wavefront error budget for the finishing vendor.

LLNL has pursued aggressive cost targets for all steps in optics fabrication, including purchasing the fused-silica blanks. One lever used to achieve a lower cost for fused silica was recognizing that finishing processes can compensate for

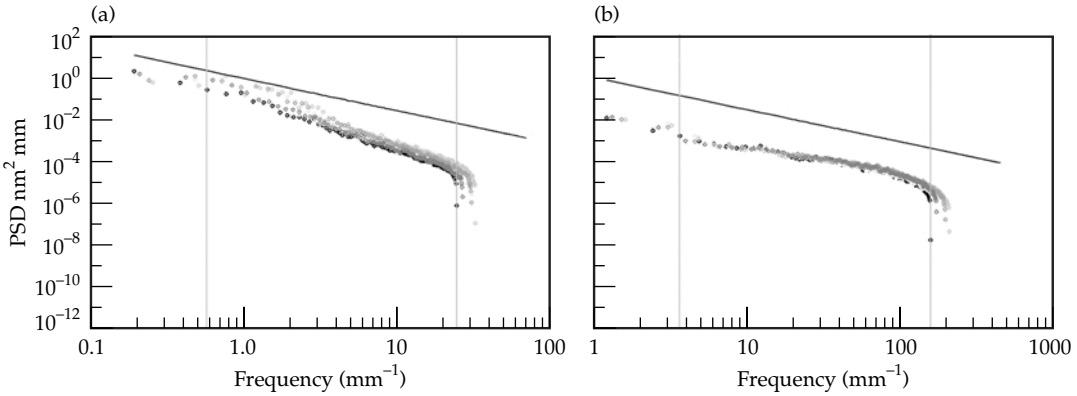

FIGURE 10. (a) NIF SF1/2 cavity spatial filter lens meeting the NIF PSD-II waviness-2 specification for spatial periods ranging from 33 mm to 0.12 mm and the PSD-III roughness specification for spatial periods >0.12 mm (b).
(40-00-0499-0815pb01)

certain types of inhomogeneities in the blank. This tradeoff means buying less-expensive fused silica and taking advantage of the recently developed capabilities of our finishing vendors.

Analyses of typical material inhomogeneities, and our detailed knowledge about the finishing processes, have led to material specifications that give substantially higher yields (at lower costs to us) from the material vendor, without significantly increasing the cost of optic finishing. For instance, power (spherical errors) and astigmatism (cylindrical errors) are typical residual errors that are corrected during the course of continuous planetary polishing by the optician during final polishing. The techniques used by opticians to do this include weighting and controlling the lap's shape through the position of the conditioner. The process used to correct a residual error is the same, whether the error is due to irregularities in the surface figure or to inhomogeneities in the material. As long as the errors vary slowly over the surface and the optic is tested in transmission while it is being corrected, material inhomogeneities can be compensated for by a surface-figure change. For instance, the NIF window-blank specification permits up to $\lambda/4$ of power to be subtracted from the homogeneity error before the final analysis. Indeed, a $\lambda/4$-power error is typically encountered and removed during final finishing.

As just described, both Tinsley and Kodak developed small-tool figuring processes that can remove transmitted wavefront errors with scale lengths larger than the size of the polishing tool. All the lenses in the NIF are aspheric, with small spherical surface-figure departures of between 1.4 and 9 μm. Because of these small aspheric departures, the NIF lenses are typically processed through all of the conventional steps for producing a spherical lens; then the required aspheric departure from the spherical surface is polished in. Since polishing can only remove material, the correct surface form is approached in a step-wise manner by an iterative process. Each polishing step is followed by a precision-metrology step, which identifies where (and how much) additional material must be removed. If too much material is removed from the wrong location, the whole surface must be brought down to bring the final surface to the correct form. To be conservative, the first polish of the aspheric zones of the lens is necessarily shallow and the residual error can be on the order of several waves.

To take advantage of the fact that small-tool figuring is typically used to produce the NIF's lenses, the material specification for lens blanks was relaxed to allow subtracting up to $\lambda/4$ of spherically symmetric error (power) and up to $\lambda/7$ of nonsymmetric long-wavelength error, before calculating the material's inhomogeneity. Long-wavelength errors were defined as errors with a spatial period >100 mm—significantly greater than the typical tool size.

Figure 11 shows a fused-silica blank, especially selected to verify that long-wavelength errors of this type and magnitude can be removed by small-tool figuring without significantly modifying the standard lens fabrication process already developed at Tinsley for NIF's spatial-filter lenses. In addition to the long-wavelength error that we intended to evaluate in this experiment, this particular blank also had a small diameter (30-mm) localized index inhomogeneity of ~$\lambda/3$ amplitude (readily visible in Figure 11). This was associated with a collection of small bubbles, which

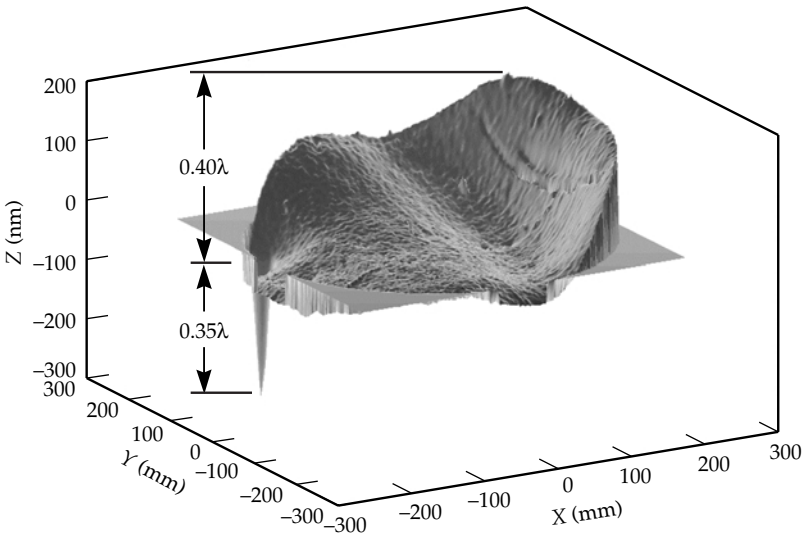

FIGURE 11. Transmitted wavefront from a fused-silica blank (oil-on-flat inhomogeneity) with a high long-spatial-scale inhomogeneity error (0.4λ). This blank also had a small-diameter, (~30-mm) discrete inhomogeneity (0.35λ) associated with a cluster of bubbles that had been sliced off. (40-00-0499-0816pb01)

was sliced off when the blank was removed from the boule. This type of localized inhomogeneity does not pass the NIF specification for P-V amplitude or for gradient rms (<λ/100 waves/cm) due to the high local gradients associated with the defect. (The blank was used despite the defect because it was difficult to obtain glass with long-wavelength error near the top end of the newly revised NIF lens-blank inhomogeneity specification.)

We expected that Tinsley's small-tool figuring process would remove long-wavelength errors in the blank, while most of the error associated with the localized inhomogeneity would remain. If the localized defect is ignored, the blank's index inhomogeneity was 5.4 ppm before the long-wavelength errors (those with spatial periods >100 mm) were subtracted—and 1.5 ppm after their subtraction. With the localized defect included, the blank had an inhomogeneity of 8.4 ppm, which far exceeds the 2-ppm historical specification for optics of this type. For a NIF spatial filter lens, this level of inhomogeneity translates to a 0.6-wave error—twice the NIF specification for P-V error on the finished lens.

Figure 12 shows the lens after the first cut at polishing the aspheric surface form into the lens. The total transmitted wavefront error at this early stage in figuring is 2.8λ. The long-wavelength material errors from the fused-silica blank are insignificant, compared to the residual errors resulting from the normal processing of the part through small-tool aspherization. This suggests that it is possible to relax the amplitude specification for allowable long-wavelength errors in lens blanks even further than λ/7, without affecting the quality of the finished NIF lenses. After the final small-tool processing, the total transmitted wavefront error for this SF1/2 cavity spatial-filter lens was reduced to <λ/5 vs the specification of λ/3—even including the error associated with the localized inhomogeneity.

The localized defect is apparent in Figure 13, but it was reduced in amplitude by a factor of seven during normal small-tool figuring to <λ/20. The finished lens met all NIF PSD and wavefront specifications, except in the subaperture containing the residual error from the original discrete inhomogeneity. This experiment demonstrated the ease with which small-tool figuring of NIF lenses can accommodate a significant amount of long-wavelength error. It also reinforced the importance of avoiding localized inhomogeneities in the raw material that are too small in scale to be removed by the small tool.

Lenses are the only NIF optics with small-tool correction of long-wavelength

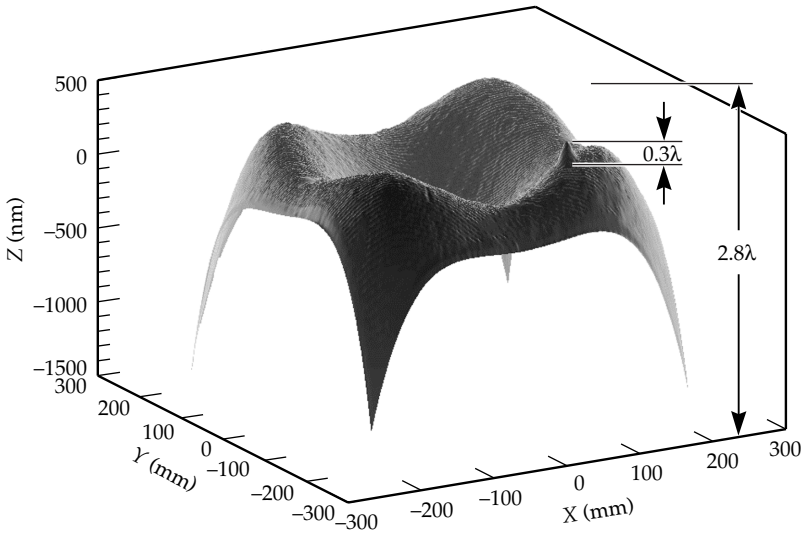

FIGURE 12. The transmitted wavefront from a lens that has been partially fabricated from the fused-silica blank shown in Figure 11. The discrete inhomogeneity is readily apparent, but the long spatial-scale error in the raw material is insignificant, relative to the total amount of error induced at this early stage of the work. (40-00-0499-0817pb01)

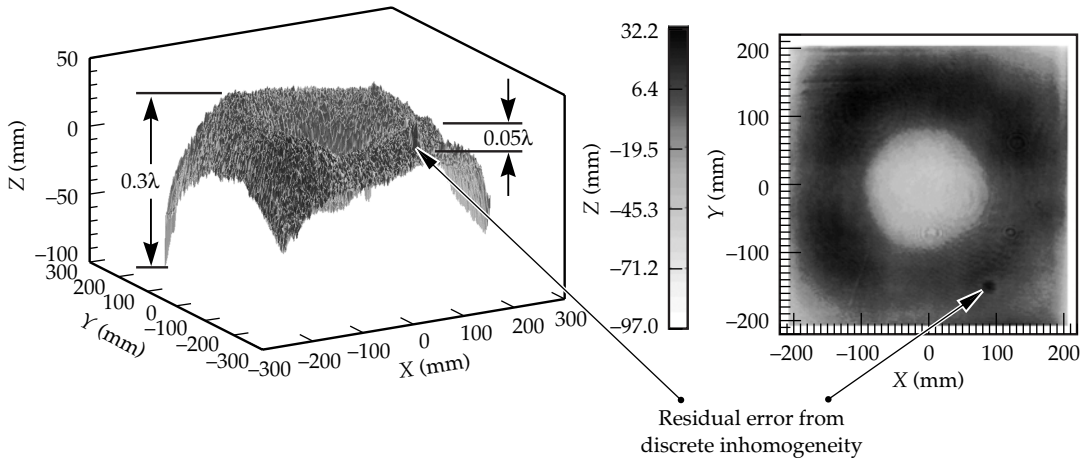

FIGURE 13. The transmitted wavefront from the finished NIF cavity spatial-filter lens made from the blank shown in Figure 11. The discrete inhomogeneity is still visible, but its amplitude has been reduced seven fold. (40-00-0499-0818pb01)

material inhomogeneities built into the specifications for the blanks. However, laser glass does have a specification allowing long-wavelength material inhomogeneities including power (0.425λ) and astigmatism (0.220λ), which are spherical and cylindrical terms, respectively. These simple long-wavelength features are correctable on plano optics with either a small tool or a pitch lap. With a pitch lap, the machine has to be operated in a condition that will yield intentionally nonflat optical surfaces, rather than the flat surfaces normally desired.

To cancel the material-induced wavefront distortion, a surface of the inverse sign and equal magnitude must be polished into the optic. This technique can also be used for fused-silica windows or BK7 polarizers, if required. In some cases, the spatial period of the material inhomogeneity might be too short to correct on a pitch lap, requiring the use of a small-tool figuring step in addition to the traditional flat-finishing manufacturing process.

Finishing for a High 3ω Laser-Damage Threshold

Finishing-development efforts, both at LLNL and at several vendors, have demonstrated that there are several paths toward obtaining fused-silica optics with finished surfaces meeting the NIF's 3ω fluence requirements: an average fluence of up to 8 J/cm^2 with peak fluences about 1.5 times higher.

For high-quality, fused-silica substrates, it is generally accepted that the damage performance of the polished surfaces is largely controlled by micron-scale subsurface damage, or by nanoscale absorbing particles. The subsurface damage results from flaws in the material generated by the various preliminary grinding and polishing steps.[8] The absorbing defects are due to contamination in the nominally 100-nm-thick polishing redeposition layer (Figure 14).

Several rules have been developed which, when followed, help to minimize subsurface damage and redeposition layer contamination. Following these rules has led to a general improvement of the laser-damage performance of the polished surfaces. They can be summarized as falling into two main groups:

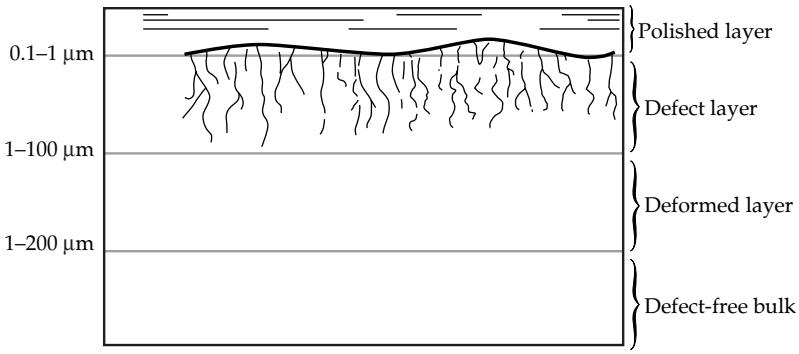

FIGURE 14. A conceptual illustration of subsurface damage. (40-00-0499-0819pb01)

1. Subsurface damage. High-performance parts are created through a series of finishing steps, each one of which uses successively smaller grinding particles. The depth of material removed in each step should be about three times the maximum size of the polishing particles used in the previous step. Knowing the size distribution of the particles used at each stage is necessary, as the maximum particle size is often two to three times larger in diameter than the average particle size.[9] Figure 15 shows the effect of subsurface damage on the laser-damage threshold for three parts with various degrees of residual subsurface damage.[10]
2. Polishing contamination. The chemo-mechanical nature of the final polishing operations on fused silica results in a smooth layer of silica being deposited, which is contaminated with the range of elements present in the polishing slurry. (These include cerium [Ce] from the ceria [CeO_2] polishing compound, plus iron, chromium, copper, sodium, potassium, and aluminum, which are present in the slurry either as anti-agglomerants or are incorporated into it as contaminants during the polishing operation.) The effects of polishing contamination can be minimized by selecting nonabsorbent polishing compounds, or by removing the contaminated re-deposition layer.

Depth profiling by secondary-ion mass spectroscopy (SIMS) shows that contaminants are present in the ~100-nm-thick redeposition layer, at levels from 1 to 1000 ppm. Figure 16 illustrates a concentration profile of Ce in the polish layer of a ceria-polished, fused-silica optic.[11] Ceria, a widely used polishing compound, is a strong absorber at 351 nm ($\alpha \approx 70{,}000\ cm^{-1}$). Simple thermo-mechanical models indicate that a 3-ns, 15-J/cm^2 laser pulse could heat a 10-nm-diameter ceria sphere to ~4000 K, therefore leading to a thermal explosion.[12] Fe, Cr, and Cu oxides would also be heated to similar levels.

The strongest indication of contaminant-related damage at high fluences is the "gray haze" morphology present on damaged ceria-polished surfaces. This haze consists of 1-μm-diameter damage pits, with concentrations of from 10^3 to

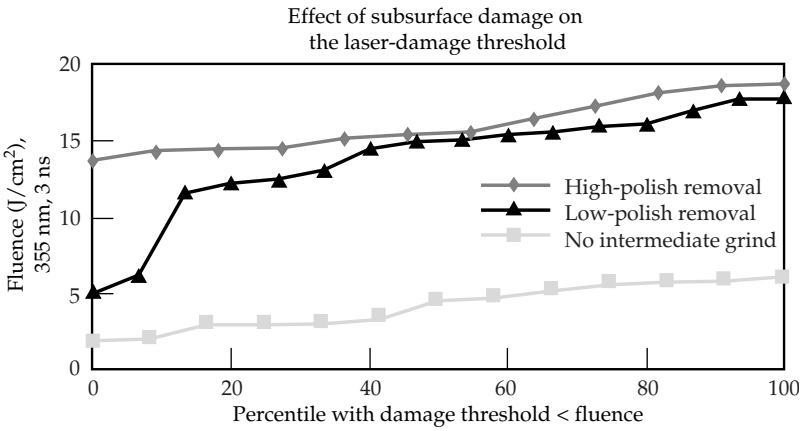

FIGURE 15. The level of grind and polish was varied on these three ceria-polished, unetched parts—to demonstrate that the first step toward increasing the damage threshold is subsurface damage control.[10] (40-00-0499-0820pb01)

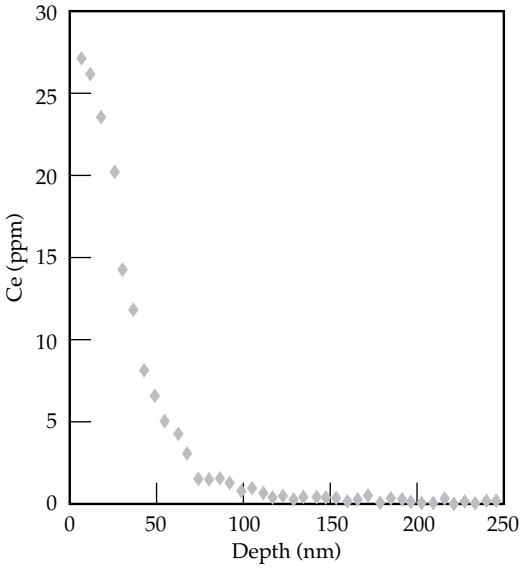

FIGURE 16. SIMS depth profile of Ce concentration inside the redeposition layer of a polished fused-silica surface.[11] (40-00-0499-0821pb01)

$10^5/cm^2$ (Figure 17).[13] The gray-haze damage can be reduced or eliminated by at least three different approaches:

1. Chemically etching the polished surface to remove contaminants. The gray-haze damage is attributed to ceria contamination in the 100-nm-thick redeposition layer. If this layer were to be removed with a hydrofluoric acid (HF) etch, it is expected that the damage morphology would also be removed. Studies of damage performance as a function of etch depth found that for 300 to 600-nm[17] deep etches, the gray haze was significantly reduced. Figure 18 compares the fluence vs damage threshold behavior of two parts similarly polished with ceria.[10] The HF-etched part exhibited no gray haze and performed significantly better in the high-fluence portion of the testing. Figure 19 shows a ceria-polished Beamlet debris shield, which was HF etched over one-third of its area to a depth of 600 nm.[17] For the as-received unetched part, high concentrations of gray-haze damage sites were observed for fluences above 12 J/cm^2. After the 600-nm-deep etch of an adjacent area of the part, the damage concentration was significantly reduced. Typically, etching the surface layer also exposes finishing flaws hidden by the redeposition layer; these are readily apparent in Figure 19.
2. Removing the contaminated surface layer with an ion etch. An alternative to a wet etch could be an ion etch of the surface layer. The Laboratory for Laser Energetics (LLE) has reported that the damage thresholds of phase-plate substrates are generally improved after an ion-beam etching.[14] Researchers at Osaka University have reported that after an argon-ion-beam etching of subsurface damage, the 355-nm damage threshold of fused-silica surfaces was doubled.[15] Ion-etch studies at LLNL show that there is a higher chance of avoiding gray-haze damage with an ion etch than without one. However, the laser-damage data obtained from these ion-etched surfaces did not conclusively show that ion etching improved the local damage performance for the parts studied.
3. Final polishing with zirconia instead of ceria. Zirconia has a negligible absorption at 351 nm and is therefore less likely than ceria to be a damage precursor. Surfaces polished with zirconia consistently do not show gray haze damage, while ceria-polished surfaces almost always show some level of gray haze at fluences near 10 J/cm^2, with 3-ns pulses. Figure 20 compares two fused-silica samples that were similarly polished using zirconia on one and ceria on the

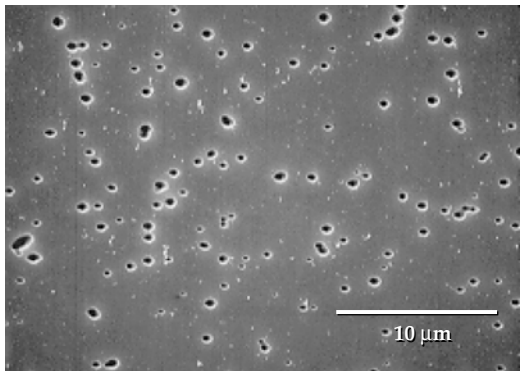

FIGURE 17. A SEM micrograph of gray-haze damage created by the 351-nm, 7-ns illumination of a polished fused-silica surface.[13]
(40-00-0499-0822pb01)

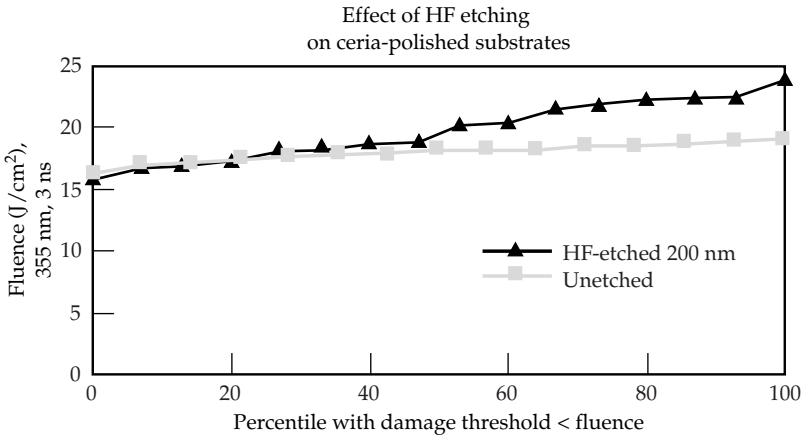

FIGURE 18. Etching with HF generally improves the high-fluence performance of ceria-polished optics by eliminating the gray-haze damage morphology.[10]
(40-00-0499-0823pb01)

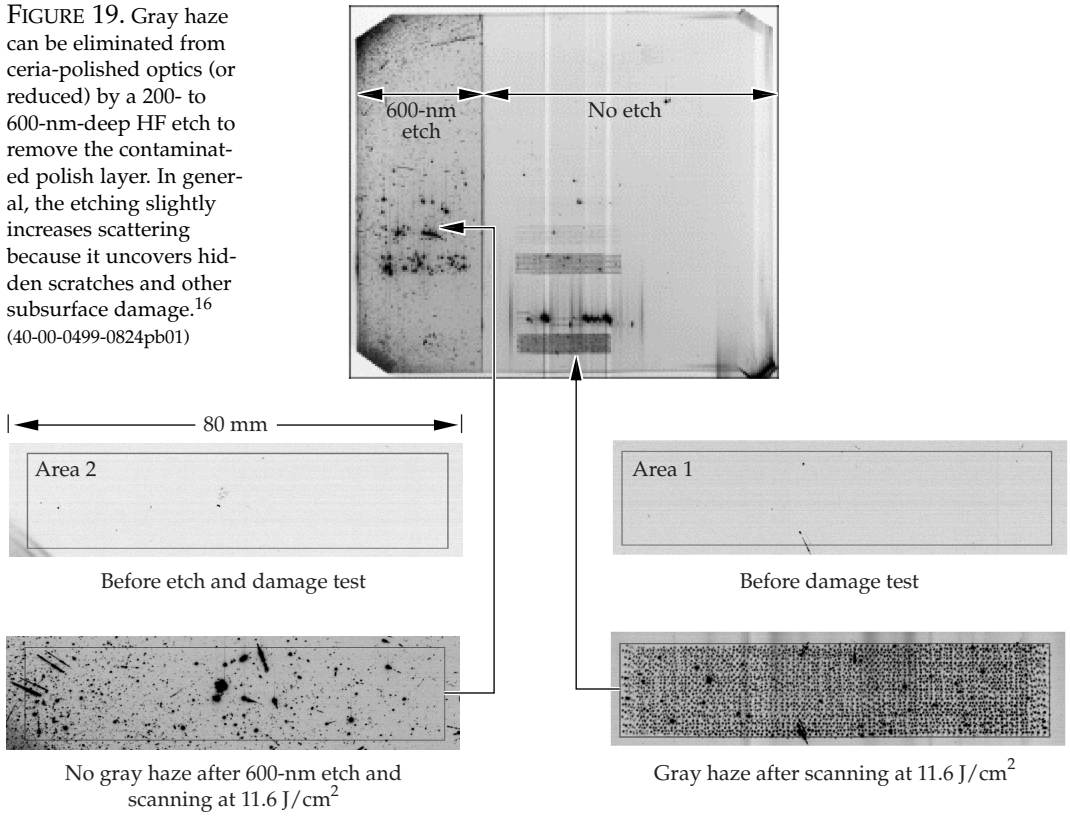

FIGURE 19. Gray haze can be eliminated from ceria-polished optics (or reduced) by a 200- to 600-nm-deep HF etch to remove the contaminated polish layer. In general, the etching slightly increases scattering because it uncovers hidden scratches and other subsurface damage.[16]
(40-00-0499-0824pb01)

other.[10] The zirconia polished surfaces show higher R:1 damage distributions than the ceria polished part. However, great care must be taken in choosing slurry parameters for zirconia polishing, as the material is easily agglomerated, resulting in surface scratches. The scratches show various degrees of propensity towards damage. Damage thresholds have been observed to decrease with zirconia polishing—if subsurface damage and scratch densities are not allowed to increase, due to poor slurry-parameter control.

Recent research at LLNL, at our finishing vendors, and elsewhere has led to new developments demonstrating that

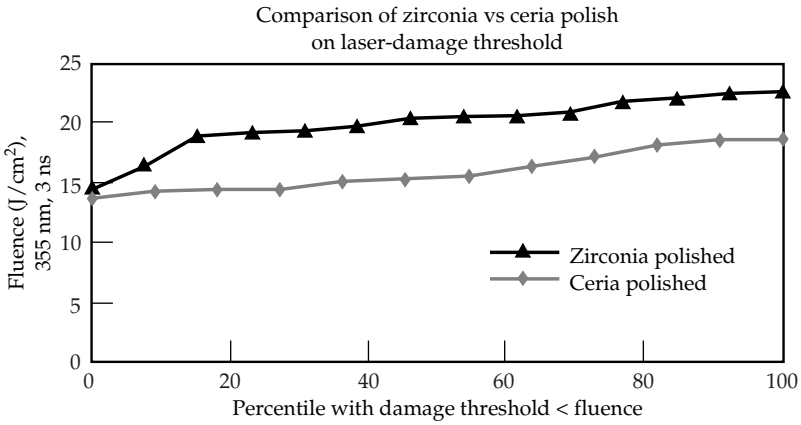

FIGURE 20. As long as subsurface damage is properly managed, the damage threshold can be improved by polishing with zirconia instead of ceria.
(40-00-0499-0825pb01)

fused-silica optics can be fabricated to meet the NIF's 3ω fluence requirements. Meeting these targets requires combining careful attention to the classic techniques of grinding and polishing (for controlling subsurface damage) with an understanding of the role played by contaminants in the polish redeposition layer.

Despite the excellent progress made in increasing damage thresholds and reducing damage density, it is clear that some damage will still occur at the NIF's operating fluences. Understanding how these more damage-resistant surfaces will behave in the NIF requires defining the statistical relations of damage density and damage growth with laser fluence and shot history.[17] This subject is explored in the article by Kozlowski on p. 193 of this issue.

Notes and References

1. L. J. Atherton, "Optics Manufacturing Readiness," *Manufacturing Readiness Plan for the National Ignition Facility,* Lawrence Livermore National Laboratory, Livermore, CA, NIF-LLNL-94-204, pp. 9–55, April 1994.
2. D. M. Aikens, L. Rich, D. Bajuk, and A. Slomba, "Developing Enabling Optics Finishing Technologies for the National Ignition Facility," Lawrence Livermore National Laboratory, Livermore, CA, UCRL-JC-129317, 1998 Summer Topical Meeting, Kailua-Kona, HI, June 8–12, 1998.
3. H. Ohmori, *Int. Jour. Japan Soc. Prec. Engr*. Vol. **26**, 273–278, (1992).
4. K. Grobsky and D. Johnson (private communication), 1995.
5. F. Tinker and J. Hopkins (private communication), 1997.
6. C. R. Wolfe, J. K. Lawson, M. C. Kellam, R. T. Maney, and A. Demiris, "Measurements of Wavefront Structure from Large-aperture Optical Components by Phase Shifting Interferometry," in *Optical Manufacturing and Testing*, Victor J. Doherty, H. Phillip Stahl, eds., in *Proc. SPIE* **2536**, 13–37 (1995).
7. J. K. Lawson, C. R. Wolfe, K. R. Manes, J. B. Trenholme, D. M. Aikens, and R. E. English, Jr., "Specification of Optical Components Using the Power Spectral Density Function," in *Optical Manufacturing and Testing*, Victor J. Doherty, H. Phillip Stahl, eds., in *Proc. SPIE* **2536**, 38–50 (1995).
8. P. P. Hed, D. F. Edwards, and J. B. Davis, *Subsurface Damage in Optical Materials: Origin, Measurement and Removal*, Lawrence Livermore National Laboratory, Livermore, CA, UCRL-99548 Rev 1 (1998). Submitted to *Appl. Opt.*
9. M. Nichols et al., LLNL Patent Docket No. IL-10215, (1998), *Fabrication of Optical Component*.
10. D. W. Camp et al., *Subsurface Damage and Polishing Compound Affect the 355-nm Laser Damage Threshold of Fused Silica Surfaces*, Lawrence Livermore National Laboratory, Livermore, CA, UCRL-JC-129301. Prepared for *Laser-Induced Damage in Optical Materials: 1997*, in *Proc. SPIE* **3244**, 356–364 (1998).
11. M. Kozlowski et al., "Depth profiling of Polishing-induced Contamination on Fused Silica Surfaces", *Laser-Induced Damage in Optical Materials: 1997*, in *Proc. SPIE* **3244**, 365–375 (1988).
12. M. D. Feit et al., "Modeling of Laser-Induced Surface Cracks in Silica at 355 nm," *Laser-Induced Damage in Optical Materials: 1997,* in *Proc. SPIE* **3244**, 350–355 (1998).
13. J. Yoshiyama et al., "A Study of the Effects of Polishing, Etching, Cleaving, and Water Leaching on the UV Laser Damage of Fused Silica," *Laser-Induced Damage in Optical Materials: 1997,* in *Proc. SPIE*, **3244**, 331–340 (1998).
14. D. J. Smith, J. A. Warner, N. LeBarron, and S. LaDelia, "Production of Distribution Phase Plates Using an Energetic Ion Process," *Annual Symposium on Optical Materials for High Power Lasers*, Sept. 28–Oct. 1, 1998.
15. T. Kamimura et al., "Improvement of Laser-Induced Surface Damage in UV Optics by Ion Beam Etching," *Annual Symposium on Optical Materials for High Power Lasers*, Sept. 28–Oct. 1, 1998.
16. L. Sheehan and R. Moaser, unpublished results, Lawrence Livermore National Laboratory, Livermore, CA (1998).
17. M. D. Feit et al., "Extrapolation of Damage Test Data to Predict Performance of Large-Area NIF Optics at 355 nm," *30th Annual Symposium on Optical Materials for High Power Lasers*, Boulder, CO, Sept. 28–Oct. 1, 1998.

Laser-Damage Testing and Modeling Methods for Predicting the Performance of Large-Area NIF Optics

M. R. Kozlowski *S. Schwartz*

M. D. Feit *L. M. Sheehan*

A. M. Rubenchik *Z. L. Wu*

The laser-damage performance of optics at Lawrence Livermore National Laboratory (LLNL) has historically been characterized using a discrete damage threshold. Such a threshold is defined as the lowest fluence at which damage is observed following illumination of roughly 20 sites with a nominally 1-mm-diam Gaussian beam. Use of a discrete damage threshold is appropriate when an optic damages at fluences significantly greater than that required in the laser system. The National Ignition Facility (NIF) laser, however, is designed to operate much closer to the damage limits of several optical components, particularly those in the final optics assembly that are exposed to ultraviolet (351-nm or 3ω) light. The damage propensity of most NIF optics is influenced by localized, defect-initiated laser damage. Because of the various material parameters and defect types influencing damage initiation, a distribution of damage thresholds can be expected. Our objective is to predict the extent of laser-induced damage that can be expected during standard operation of the NIF laser, particularly for final optical components.

New procedures and analysis techniques for damage testing have been developed to characterize damage performance. These test procedures provide statistical data needed to describe the extent of localized, defect-initiated damage on large (40- × 40-cm) optics. The testing is done with small Gaussian beams ($1/e^2$ diameter ≈ 1 mm) and subaperture test areas (a few cm^2). Statistical techniques were developed to scale the damage performance measured using small Gaussian beams to that expected from full-aperture NIF beams.

The laser-damage specifications of NIF optics are characterized by two parameters: total obscured area due to damage to an individual optic, and minimum damage size that can lead to damage to downstream optics by nonlinear imaging. The functional lifetime of an optic, as limited by either of the two specifications, is determined by the concentration of damage sites on the optic and the rate at which the sites grow. Evaluation of the risk of damage to downstream 1ω and 3ω optics by nonlinear imaging has been discussed elsewhere.[1,2] This report discusses the development of experimental techniques and data analysis methods to provide a statistical description of the concentration of damage sites on NIF-like optics. Efforts to measure damage growth rates are also introduced. Together, these two sets of data provide the basis for developing a model to predict the lifetime of NIF optics based on an obscuration limit. We provide an example that demonstrates the prediction of laser-damage density on a Beamlet-laser, 3ω, fused-silica focus lens based on off-line test data.

Damage Testing Methods

To address the statistical nature of damage, two damage testing techniques are now in use at LLNL. Both techniques, R:1 mapping and raster scanning, use commercially available lasers with nominally 1-mm-diameter laser beams to test multiple sites on an optic.

An individual R:1 threshold is determined by linearly ramping the fluence of a pulsed laser (3 to 10 ns, 10 Hz) until damage is detected at the illumination site. Damage is indicated by a change in scatter of a He–Ne laser beam from the surface being tested. The fluence at which a scatter threshold is exceeded is the damage threshold for that site. R:1 mapping consists of determining the R:1 damage threshold of multiple (typically about 100) sites using an Automated Damage Test (ADT) station.[3,4] The results of R:1 maps are plotted as cumulative damage-probability curves, as shown in Figure 1. The damage-probability curve, or S curve, is found from the ratio of the number of sites that damage below a fluence F to the total number of sites N. The 50% probability threshold is the fluence at which 50% of sites tested with the same laser parameters would show damage.

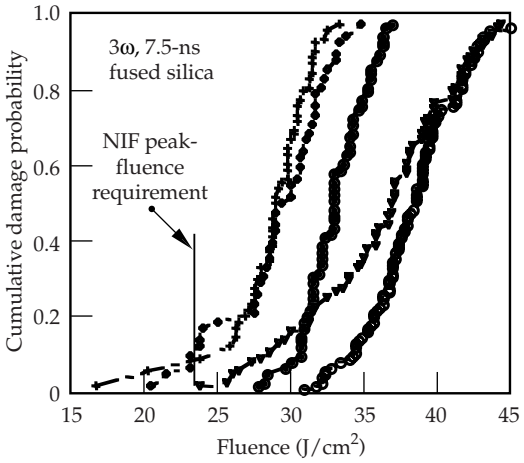

FIGURE 1. R:1 mapping S curves for silica surfaces finished with different polishing processes (τ = 7.5 ns). The 7.5-ns equivalent fluence requirement for 3ω optics is 23 J/cm^2, scaled from 3 ns using $\tau^{0.5}$ scaling. Thus, the low-fluence tail of the distribution is of greatest interest for NIF functional damage analysis. (40-00-0499-0797pb01)

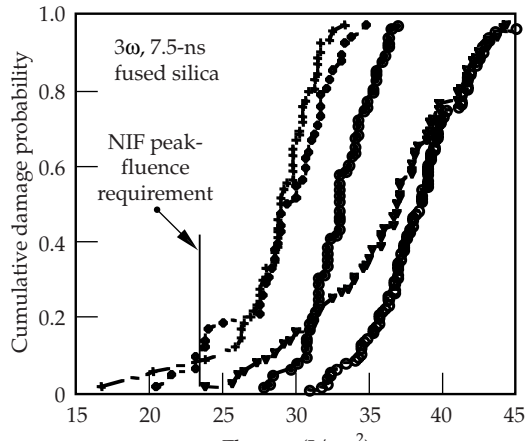

FIGURE 2. For raster-scan tests, the optic is translated in front of a pulsed, Gaussian laser beam with $1/e^2$ diameter of ~1 mm. A typical step size is the diameter of the beam at 90% of peak fluence. (40-00-0499-0798pb01)

The R:1 map is most commonly applied when comparisons of manufacturing processes and vendors are needed. The article, "Developing Optics Finishing Technologies for the National Ignition Facility," on p. 177 in this *Quarterly Report*, discusses the application of this test method to optical finishing.[5] As discussed below, the shape of the curve, particularly at the extremes, is influenced by beam parameters (fluence profile and beam diameter) and by the number of sites tested.

Although an R:1 map allows for rapid assessment of relative optical-component quality, it does not provide a quantitative measure of optic damage density at NIF-relevant fluences (i.e., at the low damage probability) because the sampled area is too small. Figure 1 shows that only the low-fluence tail of the S curve determines actual NIF performance for fused-silica optics. To obtain reliable low-fluence data, raster-scan techniques are used to test a larger number of sites (>10^3) at a single fluence. The raster-scan test allows large areas (several cm^2) to be sampled by translating the optic in front of a stationary, 1-mm-diameter test beam. The scan rate is chosen so that repetitive laser pulses overlap by a controlled amount, as shown in Figure 2. The illumination process is similar to that used for laser conditioning of optical coatings or inspecting laser glass for platinum inclusions.[4]

Our R:1 mapping station consists of a commercial Nd:YAG laser and beam-diagnostic system, a translation stage that allows rastering over the full aperture of meter-class optics, and a damage-diagnostic system. Figure 3 is a photo of the LLNL 3ω raster test system, also referred to as the large-aperture test (LAT) system. The test beam has a Gaussian profile, with a $1/e^2$ diameter at the sample plane of 1 to 1.6 mm. The repetition rate is 10 Hz, and the pulse length is 6 to 8 ns. The damage-diagnostic system, called the Defect Mapping System (DMS), uses fiber-optic light bars to internally illuminate an optic through the four edges.[6] A full-aperture scatter image of the optic is taken using the DMS, megapixel, charge-coupled device (CCD) camera both before and after

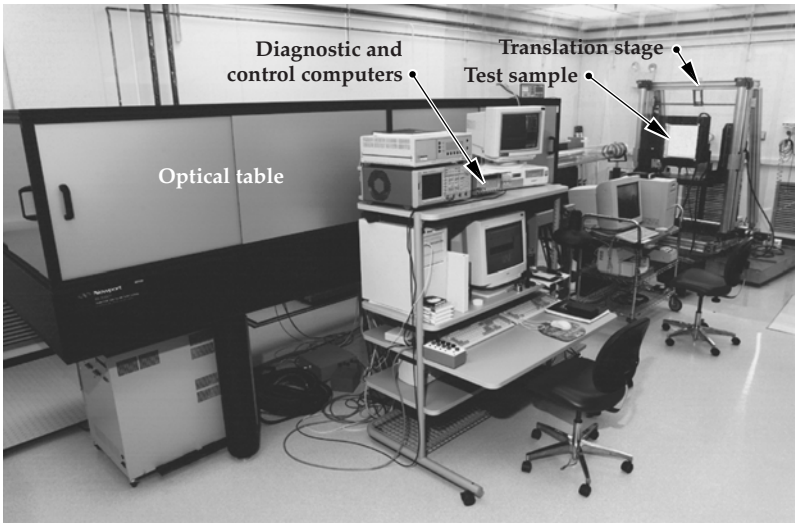

FIGURE 3. Photo of 3ω LAT system for laser-damage metrology. (40-00-0499-0799pb01)

raster-scan tests. The system detects defects as small as 10 μm over the full 40- × 40-cm optic. Because of blooming of defects in the image, it is not possible to resolve the size or features of individual defect or damage sites directly from the megapixel map. Instead, we use a long-focal-length microscope to photograph individual sites after they are located in the DMS image. The resolution of the micrographs is ~5 μm.

Damage tests are performed by raster scanning several regions of an optic at increasing fluences, and determining the fraction of sites damaged at each fluence. A typical test involves scanning seven areas of 20 cm^2 each at 3-ns-equivalent fluences of 2, 4, 6, 8, 10, 12, and 14 J/cm^2. Figure 4 shows the post-test DMS map and examples of damage-site microscopy for a test of a Beamlet, fused-silica, focus lens tested at five fluence levels. The step increment in the raster scan is specified as the beam width at a given fraction of the peak fluence. For example, a scan increment corresponding to the beam diameter at 90%

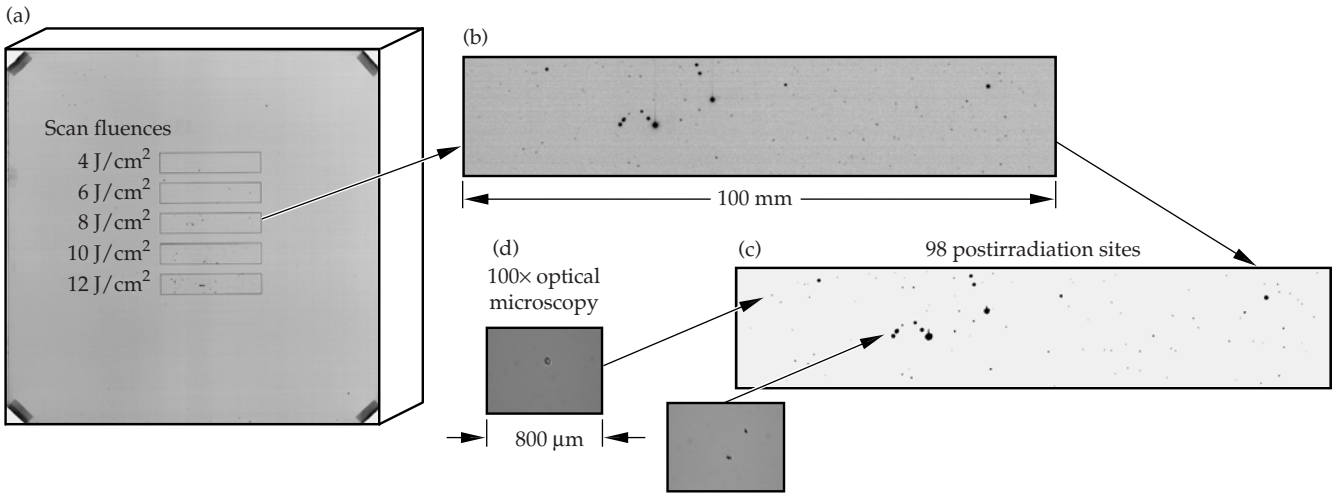

FIGURE 4. (a) DMS image of a fused-silica lens showing areas illuminated during a 3ω raster-scan test. Larger image of a single 2- × 10-cm scan area (b) before and (c) after thresholding to count defect sites. (d) A long-working-distance microscope is used to document the size and morphology of individual damage sites. (40-00-0499-0800pb01)

peak fluence would be ~0.2 mm. After scanning areas at the specified fluences, the DMS system is used to map and count the number of damage sites created during the test. Additional inspections with a microscope are used to determine the location of individual damage sites (front, rear, or bulk). Damage probabilities at a given fluence are determined by the number of damage sites detected divided by the number of pulses in the raster scan.

Figure 5 shows an example of damage-probability data obtained from scans of five, 20-cm^2 areas on a fused-silica lens. This plot of damage probability is influenced by the properties of the laser beam and the chosen scan increment. Damage-site concentrations, also shown in the plot, are independent of beam parameters and are calculated after determining the effective illumination area of the scan.

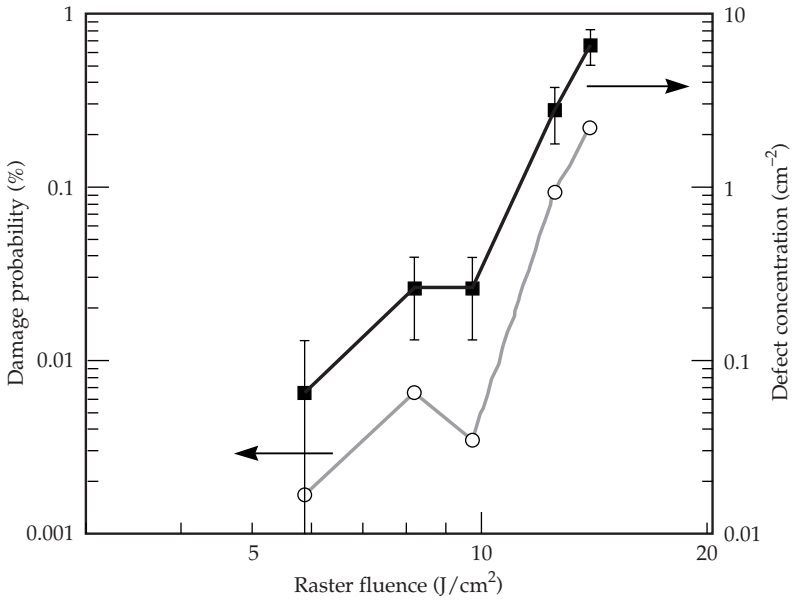

FIGURE 5. Results of a 3ω raster scan for a prototype, NIF, fused-silica focus lens. Data are from five scans at fluences of 6 to 14 J/cm^2, each measured over a different 20-cm^2 area of the optic. Damage probability (%) represents raw data for front-surface damage; defect concentration is after effective area correction. Error bars are calculated as $\pm c/\sqrt{N}$, where N is the number of damage sites detected in the scan. Effective area correction is not constant because the raster-step increment was increased for scans >8 J/cm^2 to minimize interaction between damage sites. (40-00-0499-0801pb01)

Analysis of Damage Data Using Extreme Statistics

Laser-induced surface damage initiates at extrinsic defects that strongly couple with the laser. Qualitatively, this statement is supported by the probabilistic nature of observed damage thresholds and the increased variance of observed thresholds with decrease of the illuminated area. The specific nature of responsible defects depends on the type of material (e.g., laser glass, fused silica, or KDP), polishing procedure, radiation wavelength, and other variables. To estimate operational damage probabilities for large optics from extrapolation of experimental results on smaller test areas, it is useful to apply a well-founded phenomenological approach involving a few empirical parameters. Predicting the density of damage sites on an optic is the first step in developing a general laser-damage reliability model for large optics.

Defect-initiated laser damage is a special case of the general need to predict the reliability of a system subject to failure at its weakest points, a problem that has been of great importance to industry.[7] Specific examples of the use of "extreme" statistics concern the mechanical strength of optical fibers[8] and the electrical breakdown of insulation on coaxial electrical cables.[9] In both cases, the need is to estimate the behavior of very long cables from tests conducted on much shorter lengths.

For NIF optics, our objective is to characterize the concentration of damage-inducing defects as a function of the fluence at which they cause damage. We define $P(S, F)$ as the probability that a surface area S exposed to radiation of increasing fluence will damage at fluence F. Following the methods of extreme statistics, the measured damage probability P (the S curve) is related to defect concentration c by

$$P(F) = 1 - \exp[-c(F)S] \,, \qquad (1)$$

where $c(F) = \int^F n(F')dF'$ is the cumulative areal density of defects that cause damage at a fluence less than F. In Eq. 1, the area being tested appears in the exponent. As the test area is increased, the probability of damage increases exponentially. The area scaling of damage probability given in Eq. 1 was demonstrated in a 1977 Arzamas study of laser-glass damage thresholds.[10] A similar demonstration for 3ω laser damage to fused-silica optics is described in Ref. 11.

Following the area dependence of Eq. 1, the issue for large-aperture NIF optics is not whether the optics will damage, but to what extent they will damage. The damage vulnerability of material is thus best described not by the damage probability derived from a particular test, but rather by the damage concentration $c(F)$ that is characteristic of the particular surface. To proceed further, we must specify the damage distribution function $c(F)$. In many practical applications, a power-law dependence of c on the "stress" factor (here, fluence F) has proven useful in analyzing experimental data. This so-called Weibull distribution function[7–9,11] is of widespread use. A variation of this model was used in Ref. 10 to analyze the area dependence of damage thresholds. We use this Weibull distribution in our analysis because it generally fits LLNL data. For example, Figure 6 shows a Weibull plot

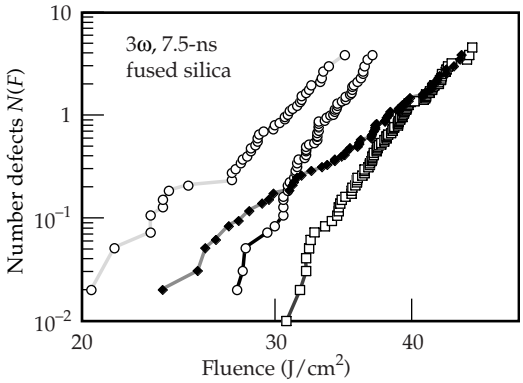

FIGURE 6. Weibull plot of cumulative damaging-defect distribution functions found from data in Figure 1. The Weibull exponent m ranges from 10 to 14 for these curves. (40-00-0499-0802pb01)

$\{N(F) = \ln[-\ln(1 - P)]$ versus $\ln F\}$ for the ADT damage test data in Figure 1. Overall, the data fit the Weibull form quite well, with a power (Weibull coefficient) m of 10 to 14. The fit to the Weibull distribution model provides confidence that the data can be extrapolated to lower fluences, therefore providing reliable estimates of damage statistics for large areas at lower, NIF-relevant fluences.

Influence of Damage-Test Beam Shape and Size

In the formulation just described, S is the illuminated area. To determine the concentration c, area S must be defined for nonuniform beam profiles. This is particularly important for the complicated irradiance patterns involved in raster scanning. Because damage incidence depends on the peak fluence seen at a point, we define S as the effective area of a flat beam with the same maximum fluence.

We have shown by use of the Weibull distribution that the damage probability for high-quality samples typically depends on a high power of the fluence, e.g., $m = 12$. If the illuminating beam is Gaussian in shape, for example, the effective source for initiating damage depends on the mth power of the Gaussian, which is much more strongly peaked than the Gaussian itself. Thus, an effectively smaller area is illuminated at the peak fluence. In general, we need to replace $S\,c(F)$ in Eq. 1 by the integral $\int c\,dxdy = c(F_0)S_{\text{eff}}$, where F_0 is the peak fluence, and S_{eff} is an effective illuminated area. For a Gaussian beam with $F = F_0 \exp[-(r/\sigma)^2]$, the appropriate area to use is $S_{\text{eff}} = \pi\sigma^2/m$. This effective area, determined jointly by the beam shape and the Weibull dependence of the data, must be used to calculate an "intrinsic" damaging defect density $c(F_0)$ characteristic of a flat-top beam of fluence F_0.

Once an intrinsic damage density is determined, the Weibull dependence allows extrapolation to other fluence levels. For example, consider our recent ADT tests (7.5-ns pulse) of fused-silica polished

surfaces. The beam $1/e^2$ radius was 1 mm, so the effective area is about 0.1 mm^2. The experimentally determined cumulative densities at 36 J/cm^2 were found to be:

- $c_1(36\ \text{J/cm}^2) = 411\ \text{cm}^{-2}$ with $m = 17$, and
- $c_2(36\ \text{J/cm}^2) = 376\ \text{cm}^{-2}$ with $m = 14$,

where the subscripts refer to side 1 and side 2. The NIF redline fluence for 7.5-ns pulses is 23 J/cm^2. At this fluence, the damaging-defect density is expected to be given by $c(36)\ (23/36)^m$, which gives $c_1 = 0.2\ \text{cm}^{-2}$ and $c_2 = 0.7\ \text{cm}^{-2}$. For a NIF-size optic of 1600-cm^2 area, we thus expect about 324 damage sites on side 1, and 1,120 sites on side 2 at the maximum fluence. The difference in damage-site densities at 23 J/cm^2 arises from the different values of m. The low defect densities reflect the high damage-resistance quality of the sample. The extrapolated differences for the large area emphasize the utility of using the exponent m as a figure of merit, all else being equal. In general, we can characterize the curve by its slope and value on a log–log plot. At lower operational fluences, very few damage sites would be expected on a large optic made using the same polishing process.

For the LAT raster scan using overlapping beams, a more rigorous approach to calculating S_{eff} is needed. We must evaluate $\int c\ dxdy = c(F_0)S_{\text{eff}}$ using $c(F) = c_0F^m(x,y)$, where $F(x,y)$ is the distribution of peak fluence over the scanned area. By evaluating this integral for a Gaussian scanning beam, and choosing the scan step so that the beams overlap at a fraction f of the peak intensity, we find that

$$S_{\text{eff}}/S_{\text{scan}} = (\pi/4)[\text{erf}(\text{arg})/\text{arg}]^2\ , \qquad (2)$$

where $\text{arg} = \sqrt{[m\ \ln(1/f)]}$. For example, by using Eq. 2, the effective area of a 20-cm^2 scan (where $f = 0.5$ and $m = 7.7$) is only 3 cm^2. We used this correction for effective area to convert the original damage probabilities in Figure 5 to the corresponding damage densities.

Such an analysis allows us to compare different types of damage tests, including the R:1 maps and LAT raster-scan tests used to evaluate NIF optics. Figure 7 compares the derived damage density for ADT and LAT tests on several silica optics produced using various polishing processes. Whereas the damaging-defect densities found using the two test methods cover a range spanning 6 orders of magnitude, the results of the two types of tests are consistent.

Extrapolation to Large-Area Optics

Using the procedure just described, we can calculate the concentration of damage sites within an area S of a flat-top beam of fluence F. For the NIF laser, the practical goal is to predict the damage concentration on full-aperture optics resulting from illumination with the actual NIF beam. As with the small-beam tests, we must account for the fluence distribution. For a beam with normal (i.e., Gaussian) beam statistics, as observed for the Beamlet laser and shown in Figure 8, we can make an analytic estimate of the effect of the fluence distribution on damage density. If the average fluence is F_0, and the $1/e$ width of the fluence distribution is σ, then

$$P(F_0) = 1 - \exp[-S\ \langle c(F_0)\rangle]\ , \qquad (3)$$

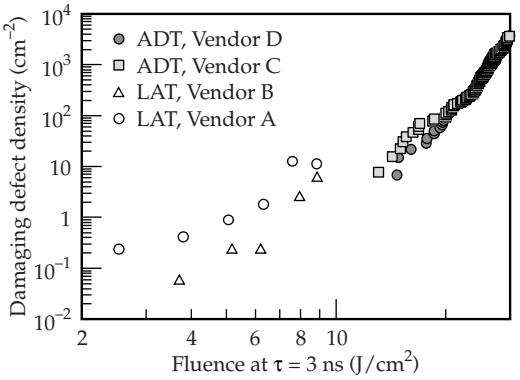

FIGURE 7. Damage densities derived for fused silica from small-area (ADT) and large-area (LAT) tests are consistent. (40-00-0499-0803pb01)

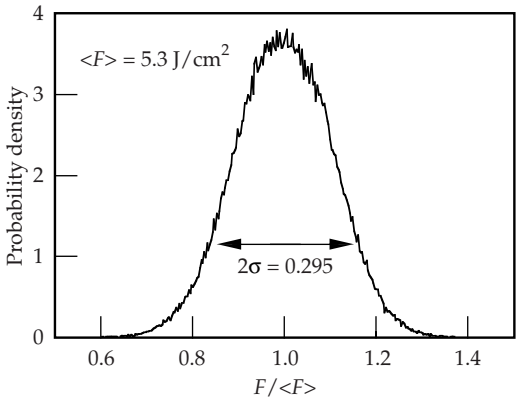

FIGURE 8. Typical Beamlet intensity distribution for medium-damage-threshold campaign with an average fluence of 5.3 J/cm^2. (40-00-0499-0804pb01)

where

$$\left\langle c\left(F_0\right)\right\rangle \approx c\left(F_0\right)\sqrt{\frac{4b^2}{4b^2+2m}}\,\mathrm{Exp}\left[\frac{m^2}{4b^2+2m}\right]. \quad (4)$$

Here, $P(F_0)$ is the expected damage probability as a function of the mean fluence, $P_0 = 1 - \exp[-S\,c(F_0)]$ is the damage probability obtained for a perfect flat-top beam at fluence F_0, $b = F_0/\sigma$, and m is the slope of the Weibull curve.

This is a good approximation provided that

$$b = F_0/\sigma >> m^{1/3}, \quad (5)$$

that is, for a sufficiently small variance (e.g., for $m = 12$, b should be greater than 2.5). Here, $c(F)$ is the cumulative damage density for the flat beam, and $\langle c\rangle$ refers to the expectation value for the NIF beam. This condition is satisfied for the distribution given in Figure 8. Equation 4 is approximate. In the case where m does not satisfy Eq. 5, $P(F_0)$ can be found by numerical integration using the exact expression

$$\left\langle c\left(F_0\right)\right\rangle = \int_0^\infty c(F)f(F)dF, \quad (6)$$

where $f(F)$ is the fluence distribution of the large beam, and the cumulative defect density $c(F)$ is obtained from the Weibull fit of the small-beam test data.

Note that the factor multiplying $c(F_0)$ in Eq. 4 gives the increase in expected damage density due to the fact that the illuminating fluence is not fixed, but has a distribution. This damage enhancement factor (DEF) can be used as a figure of merit in comparing the damage effects of beams with structure or random fluctuations. In the example case calculated below, DEF = 1.30, i.e., the damage density is expected to be 30% greater than that for a flat beam at the same average fluence.

We tested the predictive capabilities of the above model for the case of a fused-silica lens damaged on the Beamlet laser during a 1.5-ns, frequency-tripling campaign. LAT test results on the lens (at 7.5 ns) led to the front-surface data shown in Figure 5, as well as corresponding rear-surface data. Figure 9 shows the result of extrapolating the LAT results to Beamlet conditions. To predict the performance of the lens during the

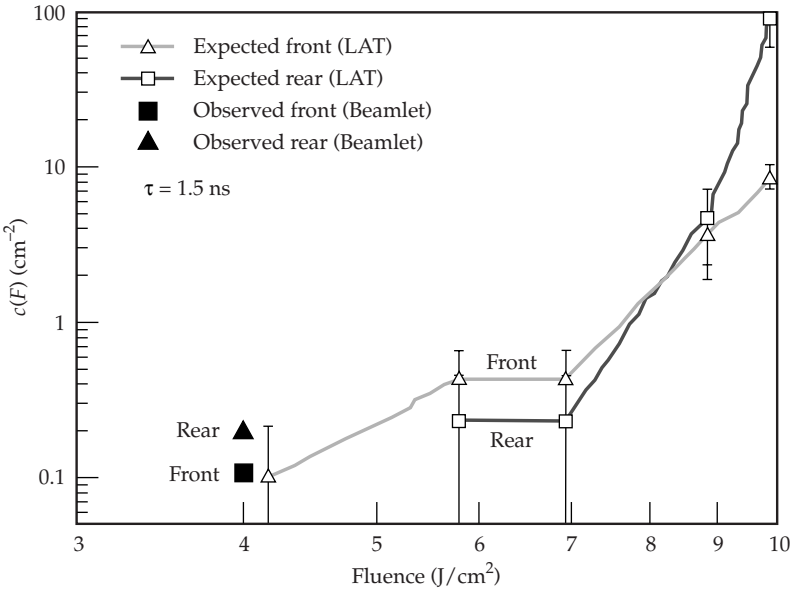

FIGURE 9. Expected damage concentration derived from LAT off-line test results for fused-silica lens, compared with observations on the Beamlet frequency-tripling campaign. Damage concentrations are specified for the peak fluence in the campaign. Detailed accounting for shot-to-shot beam structure could increase the calculated values by up to a factor of 2. (40-00-0499-0805pb01)

frequency-tripling campaign, the LAT data needed to be scaled for pulse length differences and to account for the Beamlet beam profile. Fluence levels were corrected for pulse length using standard $\sqrt{\tau}$ scaling. The fluence distribution correction to the effective defect concentrations was calculated using Eq. 4 with $F_0/\sigma = 6.7$ (from the Beamlet distribution shown in Figure 8) and $m = 7.7$ obtained from the Weibull analysis leading to Figure 5. On the same plot, we show the observed damage density on the lens following a 38-shot, frequency-tripling campaign on Beamlet. The expected and observed densities agree quite well. The expected damage curve assumes that the beam profile is the same from shot to shot. However, we know that this is not true. If intensity fluctuations (hot spots) move around completely randomly from shot to shot, the expected damage density would increase by another factor of about 2, still in good agreement with the Beamlet data.

Once damage is initiated, the growth of damage sites with subsequent pulses ultimately determines the functional lifetime of the optic. Our understanding of damage-growth-rate issues is not developed to the same level as that for damage density. We have, however, shown that the growth rates of laser damage depend on the optical material, illumination fluence, and location of the damage. For example, the growth rate of laser damage in fused-silica optics increases nearly linearly with fluence.[12] The growth rate is approximately 10 times higher for rear-surface damage than for damage initiated either in the bulk or at the front surface.[12,13] For KDP, however, damage in the bulk does not grow, whereas rear-surface damage can grow at rates faster than that for fused-silica rear surfaces.[14] We are developing an experimental plan to study the growth of damage sites on fused-silica and KDP surfaces using a 1-cm-square, 3ω beam.

Conclusions

Some laser-induced damage of optical components can be expected on the NIF. To quantify the extent of damage, we have developed testing procedures and data analysis methods that can determine a fluence-dependent damage concentration for a given optical surface. The damage concentration dependency can be convolved with the beam profile to predict the damage performance of optics on the NIF. We present an example showing that our approach is successful in predicting the damage density on a fused-silica focus lens used in a full-aperture, Beamlet, frequency-tripling campaign. Our methods provide the basis for the qualification of NIF optics vendors, and they will be used as metrology tools during the production of NIF optics.

To calculate the damage-limited functional lifetime of a NIF optic, additional information is needed. Laser-damage growth rates must be determined experimentally as a function of laser pulse and environmental parameters. Knowledge of the expected shot program for the NIF laser is also required. During the next year, this additional information will be combined with the damage concentration analysis presented here to produce a practical tool for estimating intrinsic damage lifetimes of NIF optics. Additional studies will identify modifications that are needed to the model to account for system-related effects not characterized in the off-line tests presented in this report.

Acknowledgments

We gratefully acknowledge the contribution of S. Maricle, R. Mouser, and C. Battersby in laser-damage measurements, F. Y. Génin in growth-rate studies, and P. Wegner in conducting the Beamlet tests.

Notes and References

1. M. D. Feit et al., "NIF Laser System Performance Ratings," *Supplement to SPIE* **3492**, 39–48 (1998).
2. M. D. Feit et al., "NIF Laser System Performance Ratings," *Supplement to SPIE* **3492**, 61–64 (1998).
3. J. Hue, P. Garrec, J. Dijon, and P. Lyan, "Laser–Induced Damage in Optical Materials: 1995," *SPIE* **2714**, 90–101 (1996).
4. L. Sheehan et al., "Laser-Induced Damage in Optical Materials: 1998," *SPIE* **3578**, 302–313 (1999).
5. T. G. Parham et al., *ICF Quarterly Report* **99**(2), 177, Lawrence Livermore National Laboratory, Livermore, CA, UCRL-LR-105821-99-2 (1999).
6. F. Rainer, "Laser-Induced Damage in Optical Materials: 1997," *SPIE* **3244**, 272–281 (1998).
7. S. Zacks, *Introduction to Reliability Analysis. Probability Models and Statistical Methods* (Springer-Verlag, New York, 1992).
8. R. Olshansky and R. D. Maurer, *J. Appl. Phys*. **47**, 4497 (1976).
9. I. Simoni, G. Mazzanti, and G. Montano, "Electrical Breakdown of Insulating Materials and Structures," *Size-Scale Effects in the Failure Mechanisms of Materials and Structures*, A. Carpinteri, Ed. (E&FN Spon., Chapman and Hall, London, 1996).
10. A. V. Bessarab et al., *Sov. J. Quantum Electron*. **7**, 181 (1977).
11. M. D. Feit et al., "1998 SSLA-ICF Third Annual Conference, Monterey, CA," *SPIE* **3492**, 226–234 (1998).
12. F. Salleo, R. Chinsio, and F. Y. Genin, "Laser-Induced Damage in Optical Materials: 1998," *SPIE* **3578**, 456–471 (1999).
13. M. R. Kozlowski, R. Mouser, S. Maricle, P. Wegner, and T. Weiland, "Laser-Induced Damage in Optical Materials: 1998," *SPIE* **3578**, 436–445 (1999).
14. L. Hackel et al., *Ultraviolet Light Generation and Transport in the Final Optics Assembly of the National Ignition Facility*, Lawrence Livermore National Laboratory, Livermore, CA, NIF-0017657 (January 8, 1999).

Development of the NIF Target Chamber First Wall and Beam Dumps

A. K. Burnham *J. F. Latkowski* *P. F. Peterson**
*J. M. Scott** *W. Hibbard* *R. E. Tokheim*†
P. K. Whitman *M. Gerassimenko* *D. R. Curran*†
F. Y. Genin *M. A. Norton*

The NIF target chamber beam dumps must survive significant x-ray, laser, ion, and shrapnel exposures without generating excessive vapors or particulate; such contamination of the final optics debris shields would make them susceptible to subsequent laser damage. The most important criterion for demonstrating the acceptability of NIF first-wall materials is the contamination rate of the final optics by target and ablation debris. The rate of debris-shield contamination must be consistent with the refurbishment resources of the NIF. Specifically, current plans are to retrieve, clean, and recoat the debris shields weekly, but refinish them only after six months. Sparse data suggest a limit for repetitive, dispersed metallic and refractory contamination—i.e., thin films and particles less than 1 μm (dust and microsplats)—of about 1 μg/cm^2 to allow a debris shield to last one week at NIF fluences without excessive damage growth. For an average density of 10 g/cm^3, this corresponds to only 1 nm of contamination. Because the debris shields sit ~7 m from the target chamber center, the maximum amount of mobile contamination per laser shot is about 6 g. (Mobile contamination is direct and remobilized target debris plus material ablated from the chamber wall and its various protrusions, as shown in Figure 1.) This is equivalent to a 1-nm thickness over a 7-m sphere, even though the target chamber itself has a radius of only 5 m. Due to concerns about whether a 1-μg/cm^2 contamination limit is truly acceptable, a 3-g mobile contamination/shot budget has been adopted (as described in the section Establishing a Contamination Budget).

This limit is challenging indeed. The x-ray fluences in the target chamber will routinely be in the vicinity of 1 J/cm^2 on the chamber wall, with eventual exposures up to ~2 J/cm^2 once ignition shots with yields of 10 to 20 MJ are attained.[1] Those fluences ablate 0.1 to 1.0 μm of Al each shot, which is enough to turn the debris shields into mirrors after a single shot. We earlier described x-ray experiments leading to the conclusion that B_4C was the best material for limiting ablation of the first

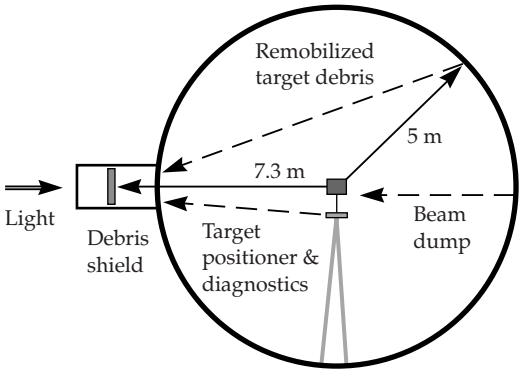

FIGURE 1. Schematic diagram of the target chamber showing the potential exposure of debris shields to contamination from the hohlraum, the target positioner and diagnostics, the beam dumps, and remobilized debris from the first wall. (40-00-0199-0182pb01)

*University of California, Berkeley, CA
†SRI International, Menlo Park, CA

wall, as it provided the lowest ablation for a readily available commercial material.[2] Even so, about 1 to 5 nm of material would be ablated over this fluence range. Laser damage experiments suggested that the final optics could tolerate 5 to 10 high-fluence shots at the resulting B_4C contamination level before substantial surface damage occurred. However, x-ray ablation of the first-wall material is only one source of optics contamination. In addition, there are ablation of beam dump material by x rays and unconverted light, ablation of material from the target positioner and diagnostics, and reablation of target material deposited on the first wall.

It was recognized early that buildup and reablation of target debris would eventually defeat even the best first-wall material.[3] Evaluation of periodic robotic CO_2 pellet cleaning concluded that it was neither practical nor effective. Instead, the relative simplicity, cheapness, and effectiveness of exochamber bead blasting made it an attractive alternative. However, the panels would have to be removed from the chamber for this cleaning, and time limitations implied a cleaning frequency of no more than once every two months. Consequently, we explored whether passive cleaning of target contamination by capture on the rear of a louvered first wall could reduce or eliminate the need for active cleaning. Reevaluation of the neutron activation issues surrounding the use of steel in the target chamber concluded that a Ni-free stainless steel would not be significantly worse in terms of occupational radiation exposure, so the ablation characteristics of stainless steel (SS) alloy 409 were evaluated, as well. The combined result of these various efforts was that reablation of target debris from the first wall, not the first wall itself, was the limiting factor of optics contamination, and that an inexpensive SS louvered first wall would be acceptable, at least for the initial years of NIF operation.

Concurrent evaluation of beam-dump materials and geometries concluded that no absorbing glass design, the method currently used on Nova, could satisfy both x-ray and unconverted-light ablation criteria. Alternative designs were considered, including louvers of B_4C and stainless steel, with and without a thin cover of transparent fluorinated ethylene propylene (FEP) Teflon. While the FEP proved to have a high enough laser damage threshold and was an effective capture agent for dust generated within the beam dump, it had the disadvantage of substantial x-ray ablation at NIF fluences. Fortunately, the amount of laser ablation of stainless steel was low enough that the escaping contamination could be reduced to acceptable levels by the same louver design used for the remainder of the first wall. This commonality of design also had the advantage of removing any beam-steering limitations, except those related to sending light into the opposing beamline.

In this article, we discuss acceptable optics contamination rates, feasibility of a SS louver first wall, demonstration of a viable beam dump, establishing a contamination budget, and reducing the shrapnel threat. We finish with a summary of our conclusions. Both the amount of transmittance loss and the reduction of the damage threshold suggest a limit of 1-nm equivalent thickness of metal film and fine dust from targets and ablated target chamber components. It is impractical to clean the interior of the target chamber often enough to prevent reablated target debris from the chamber wall from exceeding this limit, so we have adopted a self-cleaning louver design for both the first wall and beam dumps. A "dogleg" louver configuration captures about 90% of the ablated material, leading to an asymptotic limit of reablation that is consistent with the 1-nm limit.

Acceptable Optics Contamination Rates

The target chamber material and geometric design depend critically on the maximum acceptable rate of contamination of the debris shields. The NIF conceptual design set the maximum acceptable contamination rate of the debris shields at 1 nm or less average per shot based on 1% absorption for metal thicknesses of 0.2 to 0.5 nm. A simple absorption–thermal-diffusion calculation indicates that the surface of the silica is heated to ~2600°C for

1% absorption at 5 J/cm^2. However, the amount of absorption depends on the form of the deposits, i.e., whether they are truly thin films or fine particulate. Previous papers[3,4] reported that thin films of B_4C were more efficient at reducing the damage threshold of bare silica optics than equivalent masses of 1-μm-diam dust, presumably because of the more effective energy absorption. In addition, laser pulses seemed effective at partially removing the dust particles prior to the onset of substantial damage.

More recently, we found that contamination levels greater than 1-nm equivalent thickness of metal film and fine metal target debris are unacceptable with respect to both optical transmittance and laser-damage threshold criteria. The optical transmittance of several thin films made by sputtering are shown in Figure 2. Thicknesses for Cu and Au were confirmed by x-ray fluorescence. Immediately obvious is that 1 nm of B_4C and Al absorb little 3ω light, but corresponding thicknesses of Cu and Au are quite absorbing. Unfortunately, the exact relationship between absorbance and thickness is not straightforward, in part because of film oxidation. For example, the native oxide layer of Al is ~3 nm at atmospheric pressure, but it is not known whether the film will oxidize significantly at target chamber vacuum conditions between shots. Similarly, there is little difference between absorbance for the two Cu thicknesses, possibly because of oxidation. As a result, there is only a limited correspondence between the measured and calculated transmittance assuming the standard Fresnel equations.

The relationship between functional damage and metal thickness is also complicated and poorly understood. The apparent damage threshold of the silica becomes more constant, albeit lower, over the part as the effect of the uniform contamination replaces the statistical variation in damage resistance typical of polished silica. For example, when 5 nm of Cu is deposited on the surface of two types of silica polished with different processes and having average 3-ns 3ω ramped (R/1) damage thresholds of 12 and 16 J/cm^2, respectively, both damage thresholds are reduced to about 6 J/cm^2. The nature of the damage also changes, with the silica becoming less prone to brittle-crack propagation, more prone to surface waviness, and either more or less prone to submicron pitting, depending on the contaminant.

Some samples were contaminated in the Nova target chamber as a part of the effort to determine the effect of SS beam dumps on debris-shield lifetime. The resulting contamination was a combination of thin film and particulates of Al, Fe, Cu, and Au, the latter from targets, depending on the

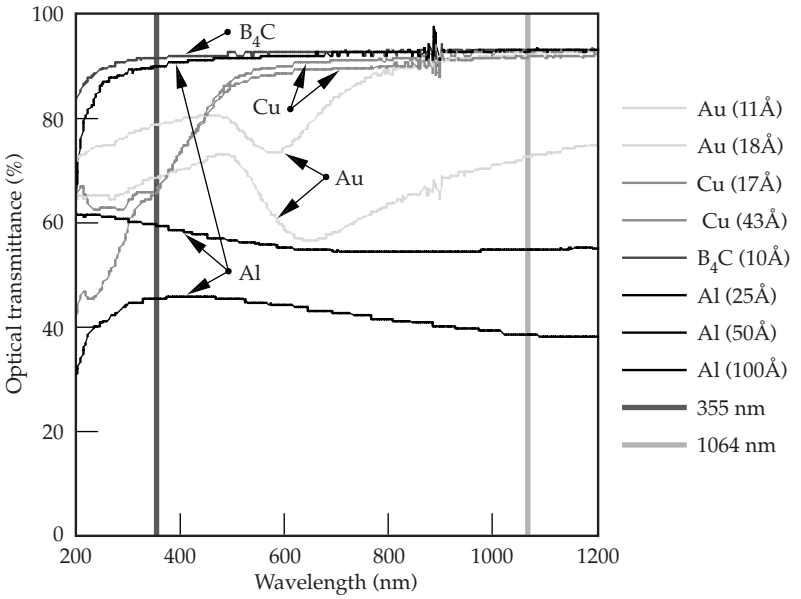

FIGURE 2. Optical transmittance of fused silica coated with thin films of potential contaminants in the NIF target chamber. (40-00-0199-0183pb01)

location in the chamber. The latter three were quantified by x-ray fluorescence. For the lowest contamination level, about 0.08 μg/cm^2 (or 0.8 nm) of Fe, Cu, and Au and 0.7% transmittance loss, the average 3-ns 3ω ramped (R/1) damage threshold was reduced from 15 to 11 J/cm^2. No work has yet been done on repetitive contamination for repeated high-fluence exposure, which is the real situation for the NIF, in order to establish a good estimate of the lifetime of debris shields. Even so, results to date indicate that the provisional 1 nm is likely an upper limit for NIF-like conditions.

Feasibility of a SS Louver First Wall

The required cleaning frequency of a flat first wall depends critically on the rate of remobilization of target debris from the wall by x rays of subsequent shots. As a part of evaluating this issue for a flat first wall of B_4C, an experiment was performed in which the ablated material from a slanted piece of B_4C was collected on a facing box with a thin slit. Analysis of the amounts and distribution of target debris in terms of a simple reablation model concluded that cleaning at least once per month would be required to prevent the remobilized target debris from contaminating the optics at an unacceptable rate. As a result, we started active consideration of a louvered first wall. The basic concept is that most of the reablated target material is captured on the back of the louver and is shielded from subsequent reablation. Consequently, the chamber becomes self-cleaning, at least with respect to metal films.

While it is conceivable, albeit expensive, to fabricate a louvered B_4C first wall, a combination of three factors—the projected difficulty and expense, the durability of SS fixtures in the Nova chamber, and the possibility that target debris would quickly make the underlying first-wall substrate material irrelevant—prompted us to reexamine the feasibility of using SS as the first wall. This option had been rejected a few years earlier because of perceived problems with neutron activation.

A reconsideration of neutron activation and disposal issues concluded that neither was a significant problem for the SS mass required to fabricate thin louvers. A plot of in-chamber dose rates as a function of cooldown time from various sources after 10 y of 1200-MJ/y operation is given in Figure 3. The dominant contribution for the first five days is the Al vacuum chamber itself. No personnel access would be allowed during this time regardless of the composition of the first wall. After that time, a 316 SS first wall would become the

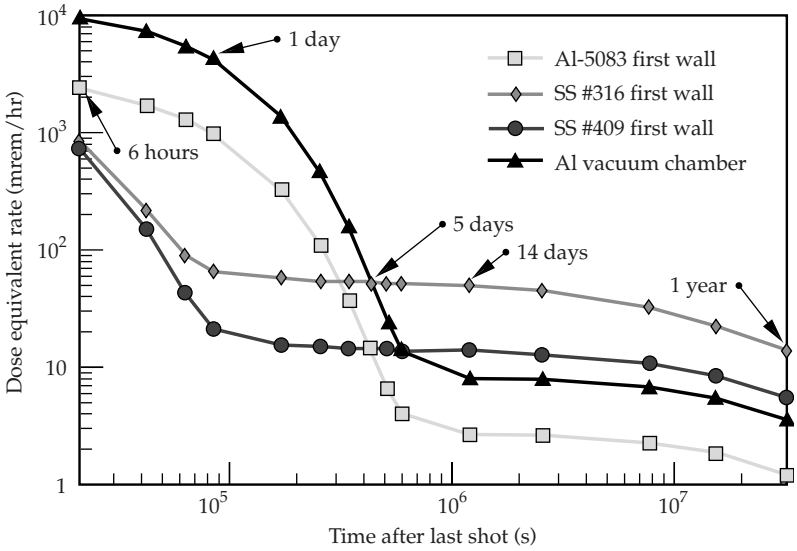

FIGURE 3. Personnel dose rate inside the target chamber after a 20-MJ ignition shot following 10 y of 1200-MJ/y yields. (40-00-0199-0184pb01)

major exposure source, but further analysis found that 90% of the problem is due to activation of Ni. Nominally Ni-free alloys are available, with Ni levels less than 0.5 wt%.[5] A similar analysis with 409 SS, including the 0.75 wt% of Ti required for welding compatibility, reveals that the long-term radiation dose is only twice that from the Al chamber itself. However, this potential increased exposure would be largely eliminated by the reduced need for cleaning activated first-wall louvers compared to a flat B_4C/Al first wall. Also, the 409 SS first wall contributes negligibly for external doses during final optics maintenance. Finally, the decommissioning dose rate for SS first-wall panels is negligibly higher than for B_4C/Al panels, and waste disposal ratings ($>10^{-8}$) are small enough to qualify as low-level radioactive waste.

Given that neutron activation is not a significant problem, two experiments were conducted to assess the ablation of 409 SS and overlying contaminants. The first experiment exposed polished coupons to 1 to 4 shots of varying fluence at normal incidence using the same technique as Anderson et al.,[2] and a second experiment compared the ablated material collected on Ti witness foils parallel to adjacent 409 SS and B_4C louvers.

The ablation per shot vs fluence is shown in Figure 4 for 409 SS, B_4C, Al, and SiO_2. As for other metals, the induced roughness due to surface melting of the SS was far greater than the removal thickness, but a 2D scan of the surface by a Wyko white-light interferometer gave a removal depth with an estimated error of less than a factor of two. The ablated thickness of SS is far less than for Al, comparable to that of SiO_2, and approximately 10 times greater than that of B_4C. Given the possibility of a 90% capture efficiency for SS louvers,[6] the amount of SS potentially escaping into the target chamber and potentially contaminating optics is not much worse than for flat B_4C panels.

The relative advantage of B_4C decreased even more based on the results of the adjacent louver experiment (see Figure 5).[7] The ablation rates of Fe, Cu, and Au calculated from the amounts collected on the Ti foils are given in Table 1. The amount of Fe collected during the first week is consistent with that expected from the data in Figure 4. In subsequent weeks, the Fe ablation drops substantially. By the third week, there is little difference between the amount of Fe from the B_4C or SS. A more detailed analysis indicates that the fraction of target debris remobilized per shot increases from 0.03 for B_4C to 0.06 for SS. Initially, therefore, B_4C does have an advantage. However, further analysis shows that the advantage diminishes with

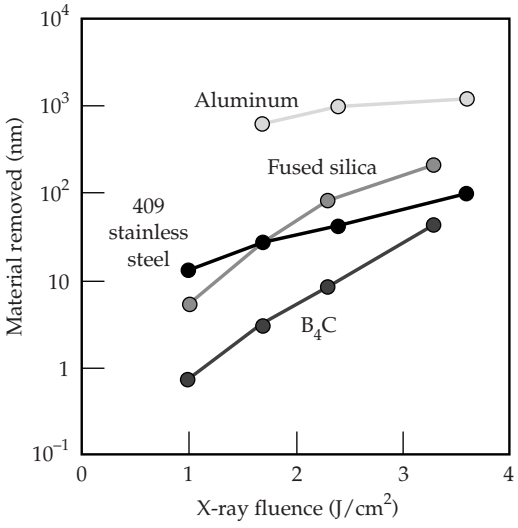

FIGURE 4. Thicknesses of 409 SS ablated as a function of x-ray fluence from a hohlraum emitting an ~200-eV blackbody spectrum. (40-00-0199-0185pb01)

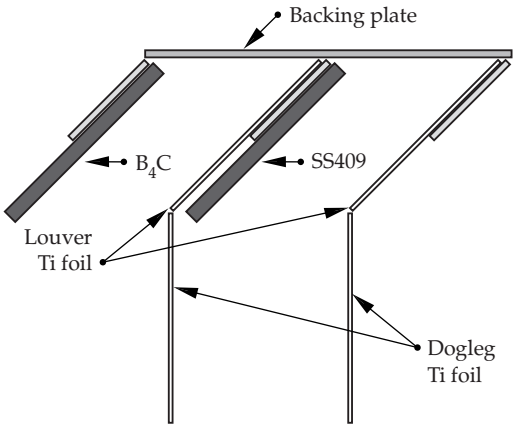

FIGURE 5. Schematic diagram of the comparative louver reablation-capture experiment. The center of the B_4C and SS louvers was approximately 40 cm from target chamber center. (40-00-0199-0186pb01)

TABLE 1. Deposition rates of target materials on witness foils used in the comparative louver reablation-capture experiment.

		Deposition rates on Ti foil opposite B_4C (μg/cm^2/shot)			Deposition rates on Ti foil opposite SS409 (μg/cm^2/shot)		
	Shots	*Cu*	*Au*	*Fe*	*Cu*	*Au*	*Fe*
Week 1	12	0.037	0.023	0.022	0.046	0.029	0.769
Week 2	3	0.084	0.027	0.034	0.134	0.052	0.087
Week 3	14	0.095	0.029	0.047	0.089	0.030	0.045
Week 4	11	0.054	0.029	0.009	0.080	0.043	0.015

time as the target debris builds up on B_4C, and the ratio of total contamination rates for B_4C and SS first wall increases to 0.9 after 90 shots, or 5 weeks on the NIF, for equivalent louver geometries.

Demonstration of a Viable Beam Dump

Finding a viable concept for absorbing unconverted light in the NIF target chamber is complicated by concurrent exposure to x rays and target shrapnel. Concepts investigated included absorbing glass, absorbing glass covered by silica or borosilicate glass, B_4C or SS covered with FEP film, and louvers of various materials with and without covers. Absorbing glasses were chosen from inexpensive commercial products to have a 1-μm optical absorbance between 1.5 and 4 cm^{-1} in order to limit the surface temperature rise to less than 100°C at 60 J/cm^2 and thereby limit thermal stress cracking. In the end, no concept could compete with the cost, contamination rate, and durability of efficient SS louvers essentially identical to those used for the remainder of the chamber first wall.

X-ray exposure tests in the Nova target chamber found that all absorbing glasses underwent severe thermal surface crazing for exposures of about 1 J/cm^2 due to a combination of the high surface temperatures and high thermal-expansion coefficients. This resulted at best in slightly more mass ablation than SS, as shown in Figure 4. This means that any absorbing glass concept would need to either shield the absorbing glass from the x rays or capture most of the ablatant. While fused silica and borosilicate glasses had acceptable x-ray ablation rates, they were prone to potentially catastrophic damage from target shrapnel. A polymeric candidate, FEP, would be immune to catastrophic shrapnel damage, but it ablated approximately 1 μm of material at these fluences. Most of the FEP ablatant would be pumped out of the chamber as a gas, but the effects of small amounts of HF and condensable products raise concerns. Exposure of candidate materials to 100 to 500 shots of 1-μm light at various fluences found that sandblasted absorbing glasses performed well for 14-ns fluences below 15 J/cm^2, but a significant fraction of the NIF beam dump will receive fluences greater than 20 J/cm^2 due to overlapping diffraction orders and beam modulation. In this higher fluence range, all glasses, including sandblasted fused silica, became prone to significant ablation and potentially catastrophic cracking. Although both B_4C and SS ablate more material at low fluences, they perform significantly better than the other materials at higher fluences, as shown in Figure 6.

A summary of the contamination masses generated from the various materials is given in Table 2 for 1.8 MJ of blue light on target producing 1 J/cm^2 of x rays. The amount of material produced from laser ablation was calculated by multiplying the relationship of ablation to fluence by the

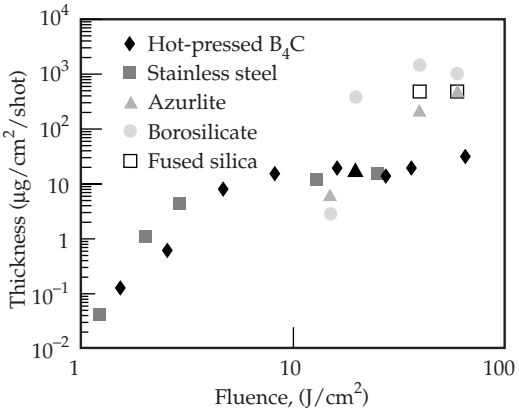

FIGURE 6. Ablation of candidate beam dump materials as a function of applied 1-μm laser fluence. (40-00-0199-0187pb01)

calculated areal fluence distribution in a NIF beam dump. All materials produce about the same amount of material before capture considerations. SS produces the most ablatant from x rays, but its ability to be formed into complex louvers makes nearby capture much easier. Considering a capture efficiency of 90% for SS and 50% for the other materials, one finds that B_4C and SS produce the least amount of contamination in the target chamber. Given that SS would be far cheaper to install and last longer, it is clearly the best option.

The SS louver concept was tested at half-NIF scale in both the two-beam and ten-beam Nova chambers. The two-beam chamber tests used 8- to 10-ns Gaussian pulses of infrared light with an average fluence up to 15 J/cm^2 and modulated fluences over small areas of 45–60 J/cm^2. The SS louvers were at 45° and were covered with a fresh film of FEP before each shot. The amount of SS captured on the FEP was consistent with that calculated from the laser ablation experiments and a 60% geometric louver capture efficiency. The second test of the prototype NIF beam dump was performed on Nova, receiving about 200 NIF-equivalent fluence shots over a period of three months. It showed only the normal expected wear. Witness coupons were analyzed to determine performance. Coupons in six-inch-manipulator tubes before and during the beam dump test showed no increase in Fe relative to that from targets and diagnostics. Fe collected just outside the beam footprint on the sides of the louvers was about 100 times less than would be ablated from a flat piece of SS due to a combination of louver efficiency and being outside the area of normal ablation. Witness coupons on the collecting side of the louver collected Fe in amounts expected.

TABLE 2. Mass-generation terms predicted for NIF beam dumps using the test materials and no louvers for 1.8-MJ blue light focused on target and 0.1-J/cm^2 x-ray fluence. (KPP and CPP refer to kinoform and continuous phase plates, respectively.)

	Mass generation terms				Target chamber
	Laser ablation		*X-ray*	*Shrapnel*	contamination rate
Material	with KPP g/shot	with CPP g/shot	g/shot	g/shot	g/shot
B_4C	1.4	1.4	0.2	~0	0.8
SS[a]	1.0	1.0	10.0	~0	1.1
Azurlite™	0.6	0.5	~11	1	6.8
Borosilicate	0.8[c]	0.6[c]	2.2	1	2.5
Fused silica[b]	2.2[c]	1.6[c]	1.1	1	2.7

[a] Louvers can capture ~90% of the SS, ~50% of the B_4C and glass ablation.
[b] Fused silica is limited to a few hundred shots.
[c] Glass numbers are highly variable.

Establishing a Budget for Contamination

Using the provisional 1-nm-per-shot limit for debris-shield contamination, a budget for contamination sources has been established. The source estimations can only be qualitative, as details of the targets are still unknown. At the chamber wall, 3 g of metal with an average density of 10 g/cm^2, if evenly dispersed, would form an average deposition thickness of 1 nm. However, the debris shields are recessed from the first wall in the final optics assembly (FOA) to a distance of 7.3 m. If the material entering the FOA were deposited according to a $1/r^2$ law, as much as 6 g could be tolerated. However, given the concerns about whether the 1-nm limit is truly acceptable, a 3-g/shot mobile contamination budget has been adopted.

Additional sources of contamination exist besides the direct and remobilized target debris. These sources include unconverted-light beam dumps and ablation from the target positioner and diagnostic snouts. The laser targets themselves will be irradiated with frequency-tripled light, and the 40% of the total energy remaining as unconverted light must be absorbed either on target shields or on the far wall of the chamber. The former contamination source is considered part of the target, but the contribution from the wall is calculated assuming no credit for the shields.

One of the advantages of a louvered SS first wall is that it also serves as an excellent beam dump. Experimental analysis of absorbing glass and B_4C beam dumps showed that SS generated the least amount of contamination of any option considered, as well as being the least expensive.[8] Convolving the expected fluence distribution with the ablation vs fluence function gave a total ablation of 1 g of SS. Because the planned louvers are calculated to have a 90% capture efficiency,[7] only 0.1 g of this contribution need be considered.

The current design for the target positioner shield uses a disk of B_4C covering a crushable Al foam. Because of the relatively small area of this shield, only 0.1 to 0.2 g of ablation is expected. Comparable amounts of ablation are expected from protruding diagnostics. Consequently, these sources' portion of the budget has been established at 0.3 g.

Because the material ablated from the first wall by 200-eV x rays is almost completely remobilized target debris rather than substrate material for fluences of ~1 J/cm^2, and because the asymptotic limit of the direct-plus-remobilized target debris is 2.1 times the direct contribution for louvers with 90% capture efficiency, a target mass of 1 g would imply a total contamination source of 2.1 g/shot. Adding this to the other sources gives a total mobile contamination of 2.5 g, less than the 3-g total budget.

There are two cautions concerning this analysis. First, it would imply that the mobile contamination would approach 0.4 g for infinitesimal targets. In fact, the ablation of the SS itself provides a lower limit of 0.5 nm for a Lambertian distribution of x rays having a maximum of 1 J/cm^2 at the target chamber poles, taking credit for a 90% louver capture efficiency. This corresponds to 1.1 g of ablatant from the chamber wall (give or take a factor of 1.5 depending on the assumed form for the ablation below 1 J/cm^2). Second, as the fluence increases, the x-ray ablation increases as well, producing a higher contamination rate. The true contamination rate is complicated by the fact that these higher fluences caused by ignition will also include higher-temperature x rays, primarily in the 350-eV range.[1] A full discussion of this issue is beyond this article, but as x-ray energy increases, the relative advantage of B_4C increases. Consequently, retrofit to B_4C louvers may be required when ignition is attained. Monitoring using Ti sample coupons on the backs of selected louvers will provide historical data on debris and substrate mobilization rates and collection efficiency, which will allow early detection of contamination trends that would warrant a first-wall retrofit.

Finally, the acceptability of a 1-nm-per-shot contamination rate has yet to be demonstrated. Unfortunately, it is extremely difficult to select materials and cleaning procedures that can achieve lower contamination rates with an unprotected debris shield. Several ideas are being considered to reduce the contamination rate. First, a beam tube

UCRL-LR-105821-99-2

extending partially into the target chamber would reduce the viewfactor of the debris shield to contamination coming from the target chamber wall. This option will likely be installed on at least some beam ports during the early stages of the NIF to determine its effectiveness. A supplemental pulsed-gas purge though this tube may also be helpful at preventing slow-moving debris from reaching the debris shield. Alternatively, a thin, disposable debris shield of either glass or polymer could prevent all but the larger shrapnel from reaching the debris shield,[9] but no material yet exists with adequate optical uniformity and x-ray ablation characteristics. Finally, some type of electrical or magnetic capture device may reduce the particulates reaching the debris shield.

Reducing the Shrapnel Threat

An earlier paper[10] presented the possibility that major damage to the first wall and final optics could come from shrapnel generated from unconverted-light shine shields and from SS tubes transporting liquid He for cooling cryogenic targets. In fact, there is very little that can be done to protect final optics from shrapnel greater than 30 μm or so. Such particles will easily penetrate a thin polymeric film and reach the debris shield. Instead, target designers must adopt a strategy of minimizing the amount of shrapnel generated and directing what is formed to the waist of the target chamber.

Figure 7 shows a cryogenic hohlraum design that substitutes conductive sapphire for He-filled SS for cooling.[11] The distribution of damage on the target chamber interior is shown in Figure 8. Most of the shrapnel damage occurs near the target chamber waist, indicating that this particular design is much more compatible with the NIF facility limitations. While this is not a final target design, it demonstrates what can be accomplished with an eye towards minimizing facility damage.

NIF will likely field a limited number of experiments that have large near-target surface areas with the potential to generate unacceptable debris ablation and shrapnel generation. Cryogenic frost and other materials have been explored to protect such large near-target surfaces, using geometries similar to a minichamber to surround the target.[12]

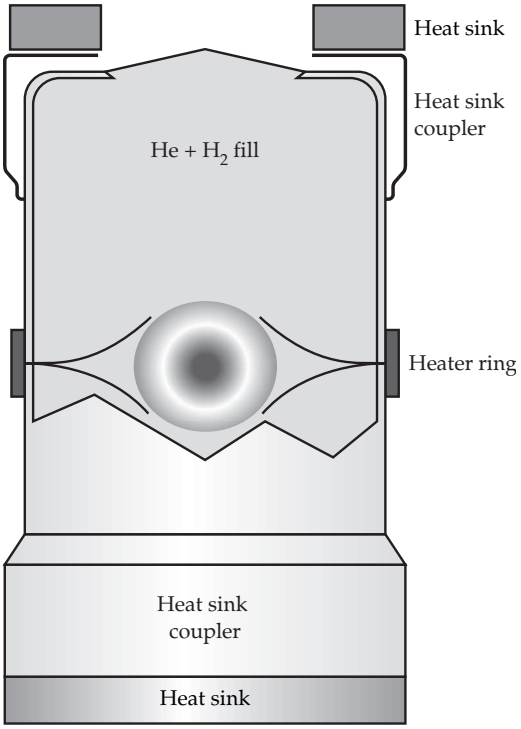

FIGURE 7. Schematic of a prototype cryogenic hohlraum design for the NIF used in shrapnel-generation experiments. (40-00-0199-0188pb01)

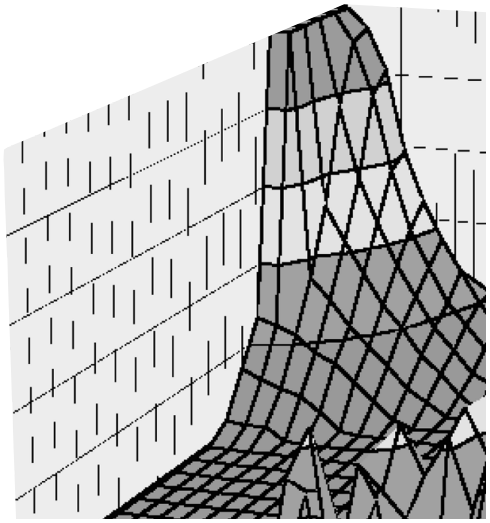

FIGURE 8. Areal distribution of the relative shrapnel damage on the first wall calculated from a 20-MJ hohlraum ignition shot. (40-00-0199-0189pb01)

Conclusions

Realistic projections of the amount of remobilized target debris for NIF conditions suggest that active target-debris cleaning cannot be conducted often enough to prevent an unacceptably large contamination rate of the final optics debris shields. As a result, a louvered first wall with passive cleaning capability is necessary. The louvered design chosen for the NIF is a "dogleg" configuration with an estimated capture efficiency of 90% for ablated material.

A secondary benefit of the passive cleaning approach is that the ablation resistance of the first wall material is less critical. Although SS ablates about 10 times as much as B_4C under NIF conditions, the ease of manufacturing highly efficient louvers largely eliminates the advantage of the B_4C. Furthermore, after a few tens of shots, the first-wall ablation is dominated by remobilization of target debris from earlier shots rather than mobilization of the substrate, making the underlying material less important.

Even with the NIF louver design, the contamination rate of the debris shield may exceed the acceptable limit, which is tentatively set at 1 nm/shot of absorbing film. As a result, supplemental methods may be required to reduce or eliminate the transport of remobilized target debris to the debris shield. None of these methods, however, can stop high-velocity shrapnel from the target, so targets must be designed to vaporize nearly completely and so that any nonvaporized material turned into shrapnel is directed towards the target chamber waist.

Acknowledgments

We thank Leonard Summers for alloy selection and supplying the 409 SS, Jim Hughes for x-ray fluorescence measurements, and the Nova technician staff for experimental support.

Notes and References

1. A. T. Anderson, R. A. Managan, M. T. Tobin, and P. F. Peterson, *Fusion Technology* **30**, 425–430 (1996).
2. A. T. Anderson, A. K. Burnham, M. T. Tobin, and P. F. Peterson, *Fusion Technology* **30**, 757–763 (1996).
3. A. K. Burnham et al., *Fusion Technology* **30**, 730–735 (1996).
4. R. Rainer et al., *Laser-Induced Damage in Optical Materials: 1996*, in *Proc. SPIE* **2966**, 463–473 (1997).
5. L. T. Summers, "Selection of Steel Alloy for the First Wall of the NIF Target Chamber," Lawrence Livermore National Laboratory Technical Memorandum, October 16, 1997.
6. A. K. Burnham et al., "Constraints on Target Chamber First Wall and Target Designs That Will Enable NIF Debris Shields to Survive," Lawrence Livermore National Laboratory, Livermore, CA, UCRL-JC-129707 (July 1997).
7. J. M. Scott, P. F. Peterson, and A. K. Burnham, *Fusion Technology* **34**, 459–463 (1998).
8. P. K. Whitman et al., "Management of unconverted light for the National Ignition Facility target chamber," 3rd Annual International Conference on Solid State Lasers for Applications to Inertial Confinement Fusion, in *Proc. SPIE* **3492**, 718–729 (1998).
9. P. Whitman, D. Milam, M. Norton, and W. Sell, *Laser-Induced Damage in Optical Materials: 1997*, in *Proc. SPIE* **3244**, 528–534 (1998).
10. R. E. Tokheim et al., *Fusion Technology* **20**, 745–751 (1996).
11. J. J. Sanchez and W. H. Giedt, "Thermal control of cryogenic cylindrical hohlraums for indirect-drive inertial confinement fusion," to be published in *Fusion Technology*.
12. P. F. Peterson and J. M. Scott, *Fusion Technology* **34**, 772–776 (1998).

NOVA UPDATE
JANUARY–MARCH 1999

Nova Operations performed 288 experiments, which exceeded our goal for the quarter. These experiments supported efforts in ICF, Defense Sciences, university collaborations, Laser Science, and Nova facility maintenance.

The two largest experiments involved the Petawatt and the cryogenic target (equation-of-state) projects. Both made significant progress, benefiting from the efficiency gained by performing the two experiments at the same time. With the exception of cryogenic gasbag experiments, the cryogenic target experiments did not use the beamline, which is required for Petawatt experiments. This allowed each experiment to be prepared virtually independent of the other.

The process of planning the decommissioning of the Nova facility continued. Next quarter will be the last quarter in which Nova will operate. The disposition of most of the major Nova components was determined in February by a committee organized by the Department of Energy. Requesters will receive responses during the next quarter. Although the initial deadline for submitting requests for Nova components has passed, some Nova components remain available. Details for requesting components are available in an ad dated December 22, 1998, in the on-line archives of the *Commerce Business Daily*.

National Ignition Facility Update January–March 1999

The second quarter 1999 was another productive quarter on the NIF site as the total Conventional Facilities work completed approached 56%. With the completion of Phase I work by Nielsen Dillingham Builders, CSP-4, in December, the coordination between prime subcontractors on site has been reduced significantly. Overhead and underground work in Laser Bay 1 continued to make good progress throughout the quarter. The lag between Laser Bay 2 and Laser Bay 1 remains approximately six weeks. Overhead drywall work in Laser Bay 2 is nearly complete, and ceiling finish installation has begun. Removal of the overhead work platform in Laser Bay 2 started in March, and approximately 25% of it was removed by the end of the month.

The current schedule date for installation of the Laser Bay 2 mat slab is mid-May which will facilitate the commencement of concrete pedestal construction in June 1999. Concrete placement in the Target Bay (Figure 1) stayed on schedule, because embed and rebar conflicts were resolved. Preparation for installation of the Target Chamber sphere is on schedule, and it is to be placed in the Target Bay in early June. Switchyard 2 concrete has been accelerated and will be completed in early April. The Optics Assembly Building is on schedule. Installation of air handlers and recirculating fans was completed, and hook-up is nearly finished. The installation of the clean room wall system is currently under way.

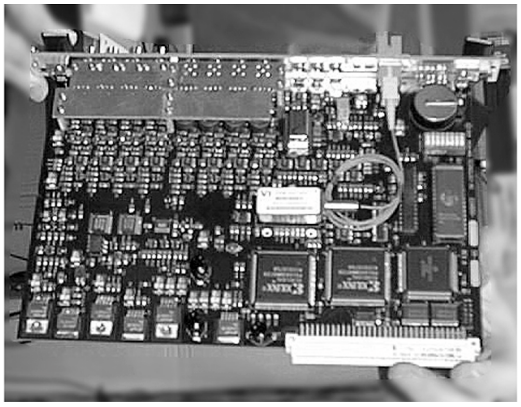

FIGURE 1. Target bay cylinder wall lift 3. (40-60-0199-0013#12A)

Title III engineering is proceeding for laser systems. Several key procurements were placed during the past quarter, including the amplifier frame assembly units and capacitor charging power supplies. Requests for Proposals were issued for several others, including the amplifier flashlamps and blast shield glass. The optical pulse generation integrated test planning is well under way, and occupancy of the Laser Building is expected next month. Planning for an integrated amplifier, power conditioning, and transport and handling test began in the second quarter 1999 with the goal of resolving interface, reliability, and contamination issues prior to entering the Laser and Target Area Building.

During this quarter, the strategy for installing the Laser Bay and switchyard structures (see Figure 2), utilities, and beam enclosures, with the exception of the main vessels, has been developed. The strategy is to package the work into two construction packages and have contractors do the work. The utilities will be in CSP-14, and the beam enclosures and support structures in CSP-16.

The computer control system continues to make good progress with front-end processors scheduled for the "Penlight" release, due in April 1999. An unanticipated problem in the framework that implements graphical user interfaces was fixed by a tiger team effort. However, the design change will delay three supervisor portions of Penlight until June 1999, which also corresponds to the earliest that hardware will become available in the preamplifier integration lab. The final design review for the facility timing system was satisfactorily held at the vendor, Timing Solutions Corporation, in February 1999. The first prototype of the companion delay generator was delivered for initial testing from a second vendor, Highland Technology.

During this quarter, the strategy for installing the Target Area structures, utilities, and beam enclosures, with the exception of the Target Chamber, has been developed. The strategy is to package the work into one construction package, CSP-15, and have a fixed-price contractor do the work. The design efforts have been stepped up to be able to finish the construction bid package in time to have the contract in place when needed.

Pitt Des Moine's subcontractor ATTM Corp. completed the layout of the target chamber ports and first wall mounting brackets (see Figure 3). Some slight interferences between the first wall mounts and the holes were noted, and some slight corrections to the mount locations were made. ATTM also set a target ball at the best-fit center of the chamber to be used for locating the pilot holes and the bored holes. The NIF survey group verified the location of some of the initial setups for boring pilot holes as well as the location on the outside of the chamber of some of the holes. Excellent agreement (less than 0.1 mm) was achieved. Boring of the holes in the target

FIGURE 2. Target bay and switchyard. (40-60-0399-0633#18)

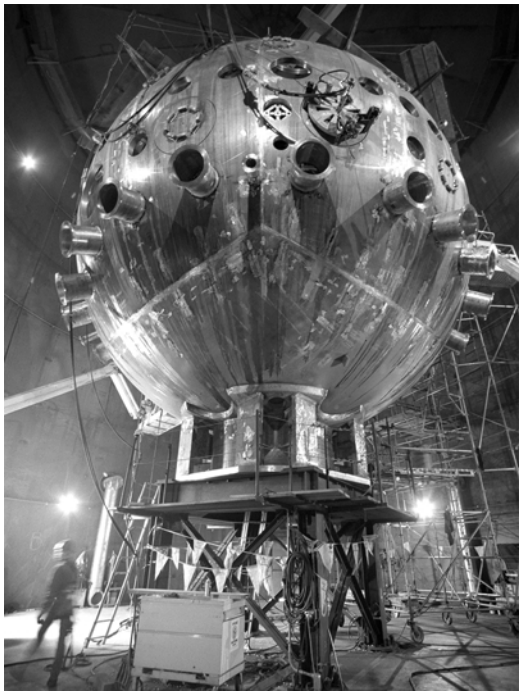

FIGURE 3. Target chamber. (40-60-0399-0669#13pb01)

chamber started in February 1999. By the end of March, In Place Machining completed 149 of the 189 holes.

In Optics, facilitization is complete at Hoya, Schott, Cleveland Crystals, Inc. (CCI), Corning, and Zygo, with only a few remaining items to be completed at Spectra-Physics and the University of Rochester/ Laboratory for Laser Energetics. Production of NIF optics is under way with the award of the contract for NIF fused silica blanks and contracts for BK7 mirror and polarizer blanks. Optics production is well under way for the optical material vendors. Initial contracts are in place for laser glass production to buy long lead items and batch materials. Contracts for amplifier cladding glass are ready to award for the first Schott campaign in April. The Lens/Windows blank pilot is nearly complete at Corning, and the first production blanks have shipped. CCI has been awarded a production contract for the DKDP triplers. The mirror and polarizer blank pilots are complete, and initial production quantities have started to ship.

Key Assurance activities to support the Project are all on schedule, including construction safety support, litigation support to the DOE for the settlement of 60(b) (e.g., quarterly reports), and the *Final Safety Analysis Report*.

The Congressional mandated Independent Project Assessment (IPA) was completed by Lockwood-Greene with a final report issued in March 1999.

At the end of FY98 there were 10 of 95 DOE/OAK Performance Measurement Milestones remaining to be completed, and by the end of the first quarter 1999, nine were completed. The only remaining FY98 milestone is the "Cooling Towers Operational," which will be accomplished in April 1999.

The FY99 DOE/OAK Performance Measurement Milestone plan includes 124 milestones. Through March 1999, 43 milestones were due, with 32 due in the second quarter 1999. A total of 36 have been completed, 29 during the second quarter 1999, including 7 early completions.

PUBLICATIONS AND PRESENTATIONS JANUARY–MARCH 1999

A

Amendt, P. A., Turner, R. E., Landen, O. L., Bradley, D. K., Suter, L. J., McEachern, R., Wallace, R. J., and Hammel, B. A., *High Growth Factor, High Convergence Implosions in Cylindrical Hohlraums*, Lawrence Livermore National Laboratory, Livermore, CA, UCRL-JC-133631-ABS. Prepared for *1st Intl Conf on Inertial Fusion Sciences and Applications*, Bordeaux, France, Sept 12, 1999.

B

Banks, P. S., Feit, M. D., and Perry, M. D., "High-Intensity Third-Harmonic Generation in Beta Barium Borate through Second-Order and Third-Order Susceptibilities," *Opt. Lett.* **24**(1), 4–6 (1999).

Battersby, C. L., Sheehan, L. M., and Kozlowski, M. R., *Effects of Wet Etch Processing on Laser-Induced Damage of Fused Silica Surfaces*, Lawrence Livermore National Laboratory, Livermore, CA, UCRL-JC-131224. Prepared for *30th Boulder Damage Symp: Annual Symp on Optical Materials for High Power Lasers*, Boulder, CO, Sept 28, 1998.

Bittner, D. N., Collins, G. W., Monsler, E., and Letts, S., *Forming Uniform HD Layers in Shells Using Infrared Radiation*, Lawrence Livermore National Laboratory, Livermore, CA, UCRL-JC-131371; *Fusion Tech.* **35**(2), 244–249 (1999).

Britten, J. A., Herman, S. M., Summers, L. J., Rushford, M. C., Auyang, L., Barton, L. M., Shore, B. W., Dixit, S. N., Parham, T. G., and Hoaglan, C. R., *Manufacture, Optical Performance and Laser Damage Characteristics of Diffractive Optics for the National Ignition Facility*, Lawrence Livermore National Laboratory, Livermore, CA, UCRL-JC-131517. Prepared for *30th Boulder Damage Symp: Annual Symp on Optical Materials for High Power Lasers*, Boulder, CO, Sept 28, 1998.

Budil, K. S., Gold, D. M., Estabrook, K. G., Remington, B. A., Kane, J., Bell, P. M., Pennington, D., Brown, C., Hatchett, S., Koch, J. A., Key, M. H., and Perry, M. D., *Blast Wave Diagnostic for the Petawatt Laser System*, Lawrence Livermore National Laboratory, Livermore, CA, UCRL-JC-130955; *Rev. Sci. Inst.* **70**(1) Pt. 2, 806–809 (1999).

C

Callahan-Miller, D. A., and Tabak, M., *Distributed Radiator, Heavy-Ion Target Driven by Gaussian Beams in a Multibeam Illumination Geometry*, Lawrence Livermore National Laboratory, Livermore, CA, UCRL-JC-131543 Rev 1. Submitted to *Nuclear Fusion*.

Collins, G. W., Celliers, P. M., Gold, D. M., Da Silva, L. B., and Cauble, R., *Shock-Compression Experiments and Reflectivity Measurements in Deuterium up to 3.5 Mbar Using the Nova Laser,* Lawrence Livermore National Laboratory, Livermore, CA, UCRL-JC-132119; *Cont. to Plasma Physics* **39**(1-2), 13–16 (1999).

Cook, B., Takagi, M., Buckley, S., Fearon, E., and Hassel, A., *Mandrel Development Update—1/98 to 12/98*, Lawrence Livermore National Laboratory, Livermore, CA, UCRL-ID-133144 (1999).

Cook, R. C., McEachern, R. L., and Stephens, R. B., *Representative Surface Profile Power Spectra from Capsules Used in Nova and Omega Implosion Experiments*, Lawrence Livermore National Laboratory, Livermore, CA, UCRL-JC-129961; *Fusion Tech.* **35**(2), 224–228 (1999).

Cook, R., Buckley, S. R., Fearon, E., and Letts, S. A., *New Approaches to the Preparation of PαMS Beads as Mandrels for NIF-Scale Target Capsules,* Lawrence Livermore National Laboratory, Livermore, CA, UCRL-JC-129955; *Fusion Tech.* **35**(2), 206–211 (1999).

Cooke, D. W., Muenchausen, R. E., and Bennett, B. L., *Measurement of Point Defect Energetics in Potassium Dihydrogen Phosphate (KDP)*, Lawrence Livermore National Laboratory, Livermore, CA, UCRL-CR-133032.

D

De Yoreo, J., Land, T. A., Orm, C., Teng, H. H., McBride, M. T., Martin, T., Dove, P. M., Tayhas, G., and Palmore, T. P., *Force Microscopy Investigation of Trends in Surface Dynamics during Crystal Growth from Solutions*, Lawrence Livermore National Laboratory, Livermore, CA, UCRL-JC-133041-ABS. Prepared for *Union of Crystallographers General Assembly and Intl Congress of Crystallography*, Glasgow, Scotland, Aug 4, 1999.

Dubois, P. F., "Scientific Components Are Coming," *IEEE Computer* **32**(3), 115–117 (1999).

E

Eder, D. C., Pretzler, G., Fill, E., Eidmann, K., and Saemann, A., *Spatial Characteristics of Kα Radiation from Weakly Relativistic Laser Plasmas*, Lawrence Livermore National Laboratory, Livermore, CA, UCRL-JC-133236. Submitted to *Applied Phys. B*.

F

Farley, D. R., Estabrook, K. G., Glendinning, S. G., Glenzer, S. H., Remington, B. A., and Stone, J. M., *Radiative Jet of Astrophysical Interest Produced at the Nova Laser Facility*, Lawrence Livermore National Laboratory, Livermore, CA, UCRL-JC-133046-DR. Submitted to *Phys. Rev. Lett*.

Farley, D., Remington, B., Estabrook, K., Glendinning, G., Back, C., Zimmerman, G., Harte, J., Turner, B., Glenzer, S., and Wallace, R., *Nova Simulations of Astrophysical Jets*, Lawrence Livermore National Laboratory, Livermore, CA, UCRL-JC-132904-COM. Submitted to *New Scientist*.

Feit, M. D., Rubenchik, A. M., Kozlowski, M. R., Genin, F. Y., Schwartz, S., and Sheehan, L. M., *Extrapolation of Damage Test Data to Predict Performance of Large-Area NIF Optics at 355 nm*, Lawrence Livermore National Laboratory, Livermore, CA, UCRL-JC-131222. Prepared for *30th Boulder Damage Symp: Annual Symp on Optical Materials for High Power Lasers*, Boulder, CO, Sept 28, 1998.

G

Glendinning, S. G., Amendt, P., Cline, B. D., Ehrlich, R. B., Hammel, B. A., Kalantar, D. H., Landen, O. L., Turner, R. E., Wallace, R. J., Weiland, T. J., Dague, N., Jadaud, J.-P., Bradley, D. K., Pien, G., and Morse, S., *Hohlraum Symmetry Measurements with Surrogate Solid Targets*, Lawrence Livermore National Laboratory, Livermore, CA, UCRL-JC-129773; *Rev. Sci. Inst.* **70**(1), 536–542 (1999).

Glenzer, S. H., Alley, W. E., Estabrook, K. G., De Groot, J. S., Haines, M., Hammer, J. H., Jadaud, J.-P., MacGowan, B. J., Moody, J. D., and Rozmus, W., *Thomson Scattering from Laser Plasmas*, Lawrence Livermore National Laboratory, Livermore, CA, UCRL-JC-131357. Prepared for *40th Annual Mtg of the Div of Plasma Physics*, New Orleans, LA, Nov 16, 1998.

Glenzer, S. H., Rozmus, W., MacGowan, B. J., Estabrook, K. G., De Groot, J. D., Zimmerman, G. B., Baldis, H. A., Hammel, B. A., Harte, J. A., Lee, R. W., Williams, E. A., and Wilson, B. G., *Thomson Scattering from High-Z Laser-Produced Plasmas*, Lawrence Livermore National Laboratory, Livermore, CA, UCRL-JC-131980; *Phys. Rev. Lett*. **82**(1), 97–100 (1999).

Gresho, P. M., *Some Aspects of the Hydrodynamics of the Microencapsulation Route to NIF Mandrels*, Lawrence Livermore National Laboratory, Livermore, CA, UCRL-JC-129963; *Fusion Tech.* **35**(2), 157–188 (1999).

H

Hammer, J. H., Tabak, M., Wilks, S. C., Bailey, D. S., Koch, J., Landen, O., Lindl, J., Rambo, P. W., Toor, A., and Zimmerman, G. B., *High Yield ICF with a Z-Pinch Driven Hohlraum*, Lawrence Livermore National Laboratory, Livermore, CA, UCRL-JC-133657-ABS. Prepared for *1st Intl Conf on Inertial Fusion Sciences and Applications (IFSA)*, Bordeaux, France, Sept 12, 1999.

Hinkel, D. E., and Haan, S. W., *Laser-Plasma Interactions in the 350 eV National Ignition Facility Target*, Lawrence Livermore National Laboratory, Livermore, CA, UCRL-JC-133083-ABS. Prepared for *3rd Intl Workshop on Laser Plasma Interaction Physics*, Banff, Canada, Feb 17, 1999.

Hinkel, D. E., Berger, R. L., Williams, E. A., Langdon, A. B., Still, C. H., and Lasinski, B. F., *Stimulated Brillouin Backscatter in the Presence of Transverse Plasma Flow*, Lawrence Livermore National Laboratory, Livermore, CA, UCRL-JC-130345; *Phys. Plasmas* **6**(2), 571–581 (1999).

Hinkel, D. E., Haan, S. W., Dittrich, T. R., and Marinak, M. M., *Design of Ignition Targets for the National Ignition Facility*, Lawrence Livermore National Laboratory, Livermore, CA, UCRL-JC-133510-ABS. Prepared for *1st Intl Conf on Inertial Fusion Sciences and Applications*, Bordeaux, France, Sept 12, 1999.

Ho, D. D. M., Grabowski, J. J., Brandon, S. T., Tsang, K. T., and Wong, A. Y., "Transfer of Free Electrons to Chlorine and Its Consequences for Mitigating Ozone Depletion in a Computational Model of the Antarctic Stratosphere," *Phys. Essays* **11**(4), 569–575 (1998).

I

Isakov, A. I., *Annual Report 1998*, Lawrence Livermore National Laboratory, Livermore, CA, UCRL-CR-133636.

Johnson, R. R., *Emergence of the National Ignition Facility*, Lawrence Livermore National Laboratory, Livermore, CA, UCRL-JC-133034-ABS. Prepared for *Optical Society of America Mtg Section Mtg*, Ann Arbor, MI, Feb 23, 1999.

K

Kalantar, D. H., Chandler, E. A., Colvin, J. D., Lee, R., Remington, B. A., Weber, S. V., Wiley, L. G., Hauer, A., Wark, J. S., Loveridge, A., Failor, B. H., Meyers, M. A., and Ravichandran, G., *Transient X-Ray Diffraction Used to Diagnose Shock Compressed Si Crystals on the Nova Laser*, Lawrence Livermore National Laboratory, Livermore, CA, UCRL-JC-129861; *Rev. Sci. Inst*. **70**(1), 629–632 (1999).

Kalantar, D. H., *Impact of Unconverted Light on Diagnostics for NIF Experiments*, Lawrence Livermore National Laboratory, Livermore, CA, UCRL-JC-133225-ABS. *Workshop on Target Diagnostics for Large Laser Fusion Facilities*, Monterey, CA, Mar 1, 1999.

Kalantar, D. H., *Shock Compressed Solids on the Nova Laser*, Lawrence Livermore National Laboratory, Livermore, CA, UCRL-JC-132687-ABS Rev. Prepared for *11th Biennial Intl Conf of the Topical Group on Shock Compression of Condensed Matter*, Snowbird, Utah, June 27, 1999.

Kane, J., Arnett, D., Remington, B. A., Glendinning, S. G., Bazan, G., Muller, E., Fryxell, B. A., and Teyssier, R., *2d vs. 3d Supernova Hydrodynamic Instability Growth*, Lawrence Livermore National Laboratory, Livermore, CA, UCRL-JC-133050. Submitted to *Astrophys. J.*

Kane, J., Drake, R. P., and Remington, B. A., *An Evaluation of the Richtmyer-Meshkov Instability in Supernova Remnant Formation*, Lawrence Livermore National Laboratory, Livermore, CA, UCRL-JC-130957; *Astrophys. J.* **511**(1,PT1), 335–340 (1999).

Kauffman, R., *ICF Quarterly Report*, **8**(4), Lawrence Livermore National Laboratory, Livermore, CA, UCRL-LR-105821-98-4 (1998).

Kauffman, R., *Inertial Confinement Fusion Monthly Highlights*, December 1998, Lawrence Livermore National Laboratory, Livermore, CA, UCRL-TB-128550-99-3.

Kauffman, R., *Inertial Confinement Fusion Monthly Highlights*, February 1999, Lawrence Livermore National Laboratory, Livermore, CA, UCRL-TB-128550-99-5.

Kauffman, R., *Inertial Confinement Fusion Monthly Highlights*, January 1999, Lawrence Livermore National Laboratory, Livermore, CA, UCRL-TB-128550-99-4.

Key, M. H., *Laser Interactions with Matter at Extremely High Intensities*, Lawrence Livermore National Laboratory, Livermore, CA, UCRL-JC-133049 ABS. Prepared for *Italian National Institute of Matter Physics*, Sicily, Italy, Jun 14, 1999.

Key, M., *ICF Quarterly Report*, **8**(3), Lawrence Livermore National Laboratory, Livermore, CA, UCRL-LR-105821-98-3 (1998).

Koch, J. A., Cui, S., and McNeill, M., *Effective Focal Length Calculations and Measurements for a Radial Diffraction Grating*, Lawrence Livermore National Laboratory, Livermore, CA, UCRL-JC-133594. Submitted to *J. Opt.Society of America A*.

Koch, J. A., Landen, O. L., Hammel, B. A., Brown, C., Seely, J., and Aglitskiy, Y., *Recent Progress in High-Energy, High-Resolution X-Ray Imaging Techniques for Application to the National Ignition Facility*, Lawrence Livermore National Laboratory, Livermore, CA, UCRL-JC-129869; *Rev. Sci. Inst.* **70**(1), 525–5629 (1999).

Kodama, R., Takahashi, K., Tanaka, K. A., Kato, Y., Murai, K., Weber, F., Barbee, T. W., and Da Silva, L. B., "Measurements of Laser-Hole Boring into Overdense Plasmas Using X-Ray Laser Refractometry," *Rev. Sci. Inst.* **70**(1), 543–548 (1999).

L

Landen, O. L., Amendt, P. A., Suter, L. J., Turner, R. E., Glendinning, S. G., Haan, S. W., Pollaine, S. M., Hammel, B. A., Tabak, M., and Rosen, M. D., *Simple Time-Dependent Analytic Model of the P2 Asymmetry in Cylindrical Hohlraums*, Lawrence Livermore National Laboratory, Livermore, CA, UCRL-JC-132445.

Landen, O. L., Bradley, D. K., Pollaine, S. M., Amendt, P. A., Glendinning, S. G., Suter, L. J., Turner, R. E., Wallace, R. J., Hammel, B. A., and Delamater, N., *Indirect-Drive Symmetry Diagnosis at NIF-Scale Using the OMEGA Laser Facility*, Lawrence Livermore National Laboratory, Livermore, CA, UCRL-JC-133632-ABS. Prepared for *1st Intl Conf on Inertial Fusion Sciences and Applications*, Bordeaux, France, Sept 12, 1999.

Langer, S. H., Scott, H. A., Marinak, M. M., and Landen, O. L., *Modeling Line Emission from ICF Capsules in 3 Dimensions*, Lawrence Livermore National Laboratory, Livermore, CA, UCRL-JC-131240. Submitted to *J. Quant. Spectros. Radiat. Transfer*.

Latkowski, J. F., Sanchez, J. J., and Pittenger, L. C., *Neutronics and Activation Analysis for the National Ignition Facility Cryogenic Target Positioner*, Lawrence Livermore National Laboratory, Livermore, CA, UCRL-JC-129954; *Fusion Tech.* **35**(2), 255–259 (1999).

Lerche, R. A., and Ognibene, T. J., *Error Analysis for Fast Scintillator-Based Inertial Confinement Fusion Burn History Measurements*, Lawrence Livermore National Laboratory, Livermore, CA, UCRL-JC-129701; *Rev. Sci. Inst*. **70**(1), 1217–1219 (1999).

Lindl, J., Herrmann, M., and Tabak, M., *Generalized Scaling of the Energy Threshold for Ignition and Efficient Burn of ICF Targets*, Lawrence Livermore National Laboratory, Livermore, CA, UCRL-JC-133642-ABS. Prepared for *1st Intl Conf on Inertial Fusion Sciences and Applications*, Bordeaux, France, Sept 12, 1999.

M

Maricle, S., Mouser, R., Schwartz, S., Parham, T., Wegner, P., and Weiland, T., *Laser Damage Performance of Fused Silica Optical Components Measured on the Beamlet Laser at 351 nm*, Lawrence Livermore National Laboratory, Livermore, CA, UCRL-JC-131221. Prepared for *30th Boulder Damage Symp: Annual Symp on Optical Materials for High Power Lasers*, Boulder, CO, Sept 28, 1998.

McEachern, R., and Alford, C., *Evaluation of Boron-Doped Beryllium as an Ablator for NIF Target Capsules*, Lawrence Livermore National Laboratory, Livermore, CA, UCRL-JC-130530; *Fusion Tech*. **35**(2), 115–118 (1999).

McEachern, R., *Tailoring Material Properties of Sputtered Beryllium*, Lawrence Livermore National Laboratory, Livermore, CA, UCRL-ID-133589.

Moody, J. D., MacGowan, B. J., Glenzer, S. H., Kirkwood, R. K., Kruer, W. L., Schmitt, A. J., Williams, E. A., and Stone, G. F., *First Measurement of Short Scalelength Density Fluctuations in a Large Laser-Plasma*, Lawrence Livermore National Laboratory, Livermore, CA, UCRL-JC-133035. Submitted to *Phys. Rev. Lett*.

Moody, J. D., MacGowan, B. J., Glenzer, S. H., Kirkwood, R. K., Kruer, W. L., Pollaine, S. M., Williams, E. A., Stone, G. F., Afeyan, B. B., and Schmitt, A. J., *Measurements of Near Forward Scattered Laser Light in a Large Inertial Confinement Fusion Plasma*, Lawrence Livermore National Laboratory, Livermore, CA, UCRL-JC-129774; *Rev. Sci. Inst*. **70**(1), 677–681 (1999).

Moran, M. J., "The Fusion Diagnostic Gamma Experiment: A High-Bandwidth Fusion Diagnostic of the National Ignition Facility," *Rev. Sci. Inst*. **70**(1) 1226–1228 (1999).

N

Norimatsu, T., Izawa, Y., Mima, K., and Gresho, P. M., "Modeling of the Centering Force in a Compound Emulsion to Make Uniform Plastic Shells for Laser Fusion Targets," *Fusion Tech*. **35**(2), 147–156 (1999).

P

Pennington, D. M., Brown, C. G., Cowan, T. E., Fountain, W., Hatchett, S. P., Henry, E., Hunt, A. W., Johnson, J., Kartz, M., and Key, M., *Petawatt Experiments at LLNL*, Lawrence Livermore National Laboratory, Livermore, CA, UCRL-JC-133590-ABS-S. Prepared for *Applications of High Field and Short Wavelength Sources VIII*, Postdam, Germany, Mar 27, 1999.

Pennington, D. M., Brown, C. G., Kartz, M., Landon, M., Perry, M. D., and Tietbohl, G., *Production of High Intensity Laser Pulses with Adaptive Optics Wavefront Correction*, Lawrence Livermore National Laboratory, Livermore, CA, UCRL-JC-132977-ABS-S. Prepared for *Intl Conf for Optics XVIII*, San Francisco, CA, Aug 2, 1999.

Pennington, D. M., Brown, C. G., Kartz, M., Landon, M., Perry, M. D., and Tietbohl, G., *Production of High Intensity Laser Pulses with Adaptive Optics*, Lawrence Livermore National Laboratory, Livermore, CA, UCRL-JC-133182-ABS. Prepared for *Intl Workshop on Adaptive Optics for Industry and Medicine*, Durham, England, Jul 12, 1999.

Perry, M. D., Feit, M. D., Barton, I., Dixit, S., Hyde, R., Early, J., and Powell, H. T., *Advanced Concepts for the Space Based Laser*, Lawrence Livermore National Laboratory, Livermore, CA, UCRL-ID-133277.

Perry, M. D., Sefcik, J. A., Cowan, T., Hatchett, S., Hunt, A., Moran, M., Pennington, D., Snavely, R., and Wilks, S. C., *Hard X-Ray Production from High Intensity Laser Solid Interactions*, Lawrence Livermore National Laboratory, Livermore, CA, UCRL-JC-130942; *Rev. Sci. Inst*. **70**(1), 265–279 (1998).

Perry, T. S., Klein, R. I., Budil, K. S., and Bach, D. R., *Interaction of Laser Driven Shock Waves with a Spherical Density Perturbation*, Lawrence Livermore National Laboratory, Livermore, CA, UCRL-JC-132867. Prepared for *Joint Working Group (JOWOG-37)*, Los Alamos, NM, Feb 2, 1998.

Phillips, T. W., Cauble, M. D., Cowan, T. E., Hatchett, S. P., Henry, E. A., Key, M. H., Perry, M. D., Sangster, T. C., and Stoyer, M. A., *Diagnosing Hot Electron Production by Short Pulse, High Intensity Lasers Using Photonuclear Reactions*, Lawrence Livermore National Laboratory, Livermore, CA, UCRL-JC-129813; *Rev. Sci. Inst*. **70**(1), 1213–1216 (1999).

R

Remington, B. A., *Extreme States of Matter on Nova*, Lawrence Livermore National Laboratory, Livermore, CA, UCRL-ID-133627.

Remington, B. A., *Studying the Stars on Earth: Astrophysics on Intense Lasers*, Lawrence Livermore National Laboratory, Livermore, CA, UCRL-JC-133464. Prepared for *American Physical Society 1999 Centennial Mtg*, Atlanta, GA, Mar 20, 1999.

Roberts, C. C., Letts, S. A., Saculla, M., Hsieh, E. J., and Cook, R. C., *Polyimide Films from Vapor Deposition: Toward High Strength, NIF Capsules*, Lawrence Livermore National Laboratory, Livermore, CA, UCRL-JC-132194; *Fusion Tech*. **35**(2), 138–146 (1999).

Robey, H. F., and Potapenko, S., *Ex-Situ Microscopic Observation of the Lateral Instability of Macrosteps on the Surfaces of Rapidly Grown KH_2PO_4 Crystals*, Lawrence Livermore National Laboratory, Livermore, CA, UCRL-JC-133360. Submitted to *J. Cryst. Growth*.

Robey, H. F., Floyd, R., Torres, R., and Burnham, A., *Impurity Leaching Rates of 1000 Liter Growth Tanks*, Lawrence Livermore National Laboratory, Livermore, CA, UCRL-ID-133365.

Robey, H. F., Hawley-Fedder, R., Floyd, R., DeHaven, M., and Rozsa, R., *LLNL KDP Crystal Growth Electronic Log Book*, Lawrence Livermore National Laboratory, Livermore, CA, UCRL-MA-133359.

Robey, H. F., Potapenko, S. U., and Summerhays, K. D., *"Bending" of Steps on Rapidly Grown KH_2PO_4 Crystals due to an Inhomogeneous Surface Supersaturation Field*, Lawrence Livermore National Laboratory, Livermore, CA, UCRL-JC-133206. Submitted to *J. Cryst. Growth*.

Ryutov, D. D., Drake, R. P., and Remington, B. A., *Criteria for Scaled Laboratory Simulations of Astrophysical MHD Phenomena*, Lawrence Livermore National Laboratory, Livermore, CA, UCRL-JC-133092. Submitted to *Astrophys. J. Supplements*.

S

Schwartz, S., Feit, M. D., Kozlowski, M. R., and Mouser, R. P., *Current 3ω Large Optic Test Procedures and Data Analysis for the Quality Assurance of National Ignition Facility*, Lawrence Livermore National Laboratory, Livermore, CA, UCRL-JC-131217. Prepared for *30th Boulder Damage Symp: Annual Symp on Optical Materials for High Power Lasers*, Boulder, CO, Sept 28, 1998.

Sheehan, L., Schwartz, S., Battersby, C., Dickson, R., Jennings, R., Kimmons, J., Kozlowski, M., Maricle, S., Mouser, R., Runkel, M., *Automated Damage Test Facilities for Materials Development and Production Optic Quality Assurance at Lawrence Livermore National Laboratory*, Lawrence Livermore National Laboratory, Livermore, CA, UCRL-JC-131230. Prepared for *30th Boulder Damage Symp: Annual Symp on Optical Materials for High Power Lasers*, Boulder, CO, Sept 28, 1998.

Smolsky, I. L., Zaitseva, N. P., Carman, L., Ryon, R. W., and Voloshin, A. E., *Mechanisms of Vicinal Sectorality Formation on Dipyramid Faces in the KDP Group Crystals*, Lawrence Livermore National Laboratory, Livermore, CA, UCRL-JC-133460. Submitted to *J. Cryst. Growth*.

Stolz, C. J., Sheehan, L. M., Maricle, S. M., Schwartz, S., and Hue, J., *Study of Laser Conditioning Methods of Hafnia Silica Multilayer Mirrors*, Lawrence Livermore National Laboratory, Livermore, CA, UCRL-JC-131215. Prepared for *30th Boulder Damage Symp: Annual Symp on Optical Materials for High Power Lasers*, Boulder, CO, Sept 28, 1998.

Suter, L. J., Landen, O. L., and Koch, J. I., *Prospects for Fluorescence Based Imaging/Visualization of Hydrodynamic Systems on the National Ignition Facility*, Lawrence Livermore National Laboratory, Livermore, CA, UCRL-JC-130980; *Rev. Sci. Inst*. **70**(1) 663–666 (1999).

Suter, L., Glenzer, S., Turner, R., Decker, C., Landen, O., Lasinski, B., MacGowan, B., Dattolo, E., Dague, N., and Juraszek, D., *Status of Our Understanding and Modeling of NIF X-Ray Coupling Efficiency*, Lawrence Livermore National Laboratory, Livermore, CA, UCRL-ID-132922.

T

Tobin, M. T., and Eder, D. C., *Modeling Debris Shield Replacement for ICF Facilities*, Lawrence Livermore National Laboratory, Livermore, CA, UCRL-JC-133646-ABS. Prepared for *1st Intl Conf on Inertial Fusion Sciences and Applications*, Bordeaux, France, Sept 12, 1999.

Turner, R. E., Landen, O. L., Bell, P., Costa, R., and Hargrove, D., *Achromatically Filtered Diamond Photoconductive Detectors for High Power Soft X-Ray Flux Measurements*, Lawrence Livermore National Laboratory, Livermore, CA, UCRL-JC-129713; *Rev. Sci. Inst*. **70**(1), 656–658 (1999).

W

Weakley, S. C., Stolz, C. J., Wu, Z. L., Bevis, R. P., and von Gunten, M. K., *Role of Starting Material Composition in Interfacial Damage Morphology of Hafnia Silica Multilayer Coatings*, Lawrence Livermore National Laboratory, Livermore, CA, UCRL-JC-131214. Prepared for *30th Boulder Damage Symp: Annual Symp on Optical Materials for High Power Lasers*, Boulder, CO, Sept 28, 1998.

Wharton, K. B., Kirkwood, R. K., Glenzer, S. H., Estabrook, K. G., Afeyan, B. B., Cohen, B. I., Moody, J. D., MacGowan, B. J., and Joshi, C., *Observation of Resonant Energy Transfer between Identical-Frequency Laser Beams*, Lawrence Livermore National Laboratory, Livermore, CA, UCRL-JC-130320. Prepared for *American Physical Society Div of Plasma Physics Mtg*, New Orleans, LA, Nov 20, 1998.

Whitman, P. K., Bletzer, K., Hendrix, J. L., Genin, F. Y., Hester, M., and Yashiyama, J., *Laser-Induced Damage of Absorbing and Diffusing Glass Surfaces under IR and UV Irradiation*, Lawrence Livermore National Laboratory, Livermore, CA, UCRL-JC-131213. Prepared for *30th Boulder Damage Symp: Annual Symp on Optical Materials for High Power Lasers*, Boulder, CO, Sept 28, 1998.

Williams, E. A., *Bending and Spreading of RPP/SSD Laser Beams*, Lawrence Livermore National Laboratory, Livermore, CA, UCRL-JC-132989-ABS. Prepared for *3rd Intl Workshop on Laser Plasma Interaction Physics*, Banff, Canada, Feb 17, 1999.

Wu, Z. L., Feit, M. D., Kozlowski, M. R., Rubenchik, A. M., and Sheehan, L., *Laser Modulated Scattering as a Nondestructive Evaluation Tool for Optical Surfaces and Thin Film Coatings*, Lawrence Livermore National Laboratory, Livermore, CA, UCRL-JC-131211. Prepared for *30th Boulder Damage Symp: Annual Symp on Optical Materials for High Power Lasers*, Boulder, CO, Sept 28, 1998.

Wu, Z. L., Feit, M. D., Kozlowski, M., Natoli, J. Y., Rubenchik, A. M., Sheehan, L., and Yan, M., *Single-Beam Photothermal Microscopy—a New Diagnostic Tool for Optical Materials*, Lawrence Livermore National Laboratory, Livermore, CA, UCRL-JC-131212. Prepared for *30th Boulder Damage Symp: Annual Symp on Optical Materials for High Power Lasers*, Boulder, CO, Sept 28, 1998.

Y

Young, P. E., Berger, R. L., Decker, C., Divol, L., Hinkel, D. E., Kirkwood, R. K., Geddes, C., Glenzer, S. H., Langdon, A. B., and MacGowan, B. J., *Recent Laser-Plasma Interaction Studies at LLNL*, Lawrence Livermore National Laboratory, Livermore, CA, UCRL-JC-133633-ABS. Prepared for *1st Intl Conf on Inertial Fusion Sciences and Application*, Bordeaux, France, Sept 12, 1999.

Young, P. E., Moody, J. D., Rozmus, W., Russell, D. A., and DuBois, D. F., *Angular Dependence of 3ω 0/2 Spectra near the Two-Plasmon Decay Threshold*, Lawrence Livermore National Laboratory, Livermore, CA, UCRL-JC-133630-ABS. Prepared for *1st Intl Conf on Inertial Fusion Sciences and Application*, Bordeaux, France, Sept 12, 1999.

Z

Zaitseva, N., Atherton, J., Rozsa, R., Carman, L., Smolsky, I., Runkel, M., Ryon, R., and James, L., "Design and Benefits of Continuous Filtration in Rapid Growth of Large KDP and DKDP Crystals," *J. Crystal Growth* **197**(4), 911–920 (1999).

Zaitseva, N., Smolsky, I., Carman, L., and Ryon, R., *Rapid Crystal Growth from Solutions: Mechanisms of Growth and Defect Formation*, Lawrence Livermore National Laboratory, Livermore, CA, UCRL-JC-133048-ABS. Prepared for *18th Intl Congress of Crystallography*, Glasgow, Scotland, Aug 4, 1999.

Ze, F., Landen, O. L., Bell, P. M., Turner, R. E., Tutt, T., Alvarez, S. S., and Costa, R. L., *Investigation of Quantum Efficiencies in Multilayered Photocathodes for Microchannel Plate Applications*, Lawrence Livermore National Laboratory, Livermore, CA, UCRL-JC-129620; *Rev. Sci. Inst*. **70**(1), 659–662 (1999).

ICF/NIF and HEDES Program
Lawrence Livermore National Laboratory
P.O. Box 808, L-475
Livermore, California 94551

Address Correction Requested